



**HAL**  
open science

## **Initial results from the Oman Drilling Project Multi-Borehole Observatory: Petrogenesis and ongoing alteration of mantle peridotite in the weathering horizon**

Peter B Kelemen, James A Leong, Juan Carlos de Obeso, Jürg M Matter,  
Eric T Ellison, Alexis Templeton, Daniel B Nothaft, Alireza Eslami, Katy  
Evans, Marguerite Godard, et al.

### ► To cite this version:

Peter B Kelemen, James A Leong, Juan Carlos de Obeso, Jürg M Matter, Eric T Ellison, et al..  
Initial results from the Oman Drilling Project Multi-Borehole Observatory: Petrogenesis and ongoing  
alteration of mantle peridotite in the weathering horizon. *Journal of Geophysical Research: Solid  
Earth*, 2021, 126 (12), pp.e2021JB022729. 10.1029/2021JB022729 . hal-03513332

**HAL Id: hal-03513332**

**<https://hal.science/hal-03513332>**

Submitted on 5 Jan 2022

**HAL** is a multi-disciplinary open access archive for the deposit and dissemination of scientific research documents, whether they are published or not. The documents may come from teaching and research institutions in France or abroad, or from public or private research centers.

L'archive ouverte pluridisciplinaire **HAL**, est destinée au dépôt et à la diffusion de documents scientifiques de niveau recherche, publiés ou non, émanant des établissements d'enseignement et de recherche français ou étrangers, des laboratoires publics ou privés.

## Initial results from the Oman Drilling Project Multi-Borehole Observatory: Petrogenesis and ongoing alteration of mantle peridotite in the weathering horizon

Peter B. Kelemen<sup>1</sup>, James A. Leong<sup>1</sup>, Juan Carlos de Obeso<sup>2</sup>, Jürg M. Matter<sup>3</sup>, Eric T. Ellison<sup>4</sup>, Alexis Templeton<sup>4</sup>, Daniel B. Nothhaft<sup>5</sup>, Alireza Eslami<sup>6</sup>, Katy Evans<sup>7</sup>, Marguerite Godard<sup>8</sup>, Benjamin Malvoisin<sup>6</sup>, Jude A. Coggon<sup>3</sup>, Nehal H. Warsi<sup>9</sup>, Philippe Pézard<sup>8</sup>, Saebyul Choe<sup>10</sup>, Damon A.H. Teagle<sup>3</sup>, Katsuyoshi Michibayashi<sup>11</sup>, Eiichi Takazawa<sup>12</sup>, Zaher Al Sulaimani<sup>13</sup> and the Oman Drilling Project Science Team

1: Lamont Doherty Earth Observatory, Columbia University, Palisades NY 10964, [peterk@LDEO.columbia.edu](mailto:peterk@LDEO.columbia.edu) ... 2. Dept. of Geosciences, University of Calgary 3. School of Ocean & Earth Science, University of Southampton 4. Dept. of Geological Sciences, University of Colorado, Boulder 5. School of Engineering and Applied Sciences, University of Pennsylvania 6: ISTerre, Université de Grenoble-Alpes 7: School of Earth & Planetary Sci., Curtin University 8: CNRS Géosciences, Université de Montpellier 9. Alara Resources Ltd., Oman 10. Dept. of Earth & Planetary Sci., American Museum of Natural History ... 11. Dept. of Earth & Planetary Sciences, Nagoya University 12. Dept. of Geology, Niigata University & VERC IMG JAMSTEC 13. Oman Water Society & Middle East Desalination Research Center

### Abstract

The Oman Drilling Project “Multi-Borehole Observatory” (MBO) samples an area of active weathering of tectonically exposed peridotite. This paper reviews the geology of the MBO region, summarizes recent research, and provides new data constraining ongoing alteration. Host rocks are partially to completely serpentinized, residual mantle harzburgites and replacive. Dunites show evidence for “reactive fractionation”, in which cooling, crystallizing magmas reacted with older residues of melting. Harzburgites and dunites are 65-100% hydrated. Ferric to total iron ratios vary from 50 to 90%. In Hole BA1B, alteration extent decreases with depth. Gradients in water and core composition are correlated. Serpentine veins are intergrown with, and cut, carbonate veins with measurable <sup>14</sup>C. Ongoing hydration is accompanied by SiO<sub>2</sub> addition. Sulfur enrichment in Hole BA1B may result from oxidative leaching of sulfur from the upper 30 m, coupled with sulfate reduction and sulfide precipitation at 30-150 m. Oxygen fugacity deep in Holes BA3A, NSHQ14 and BA2A is fixed by the reaction 2H<sub>2</sub>O = 2H<sub>2</sub> + O<sub>2</sub> combined with oxidation of ferrous iron in serpentine, brucite and olivine. fO<sub>2</sub> deep in Holes BA1A, BA1D and BA4A is 3-4 log units above the H<sub>2</sub>O-H<sub>2</sub> limit, controlled by equilibria involving serpentine and brucite. Variations in alteration are correlated with texture, with reduced, low SiO<sub>2</sub> assemblages in mesh cores recording very low water/rock ratios, juxtaposed with adjacent veins recording much higher ratios. The proportion of reduced mesh cores vs oxidized veins increases with depth, and the difference in fO<sub>2</sub> recorded in cores and veins decreases with depth.

### Plain Language Summary

The Oman Drilling Project developed a “Multi-Borehole Observatory” (MBO) in an area of active weathering of tectonically exposed peridotite, to study the geochemistry, mechanics and hydrology of peridotite alteration, which modifies the mineralogy, composition, density and rheology of mantle lithologies, creates and sustains plate boundaries, and forms dramatic redox gradients. In turn, these redox conditions support a unique subsurface microbial ecosystem, form free H<sub>2</sub> gas, facilitate methane generation, and potentially play a role in the origin of life on this and other planets. This paper provides an overview of the geology of the area within and surrounding the MBO, a summary of recent research on core and fluids from three new cored boreholes and four new rotary boreholes in the MBO, together with older Omani water monitoring well NSHQ14, and new data and calculations constraining ongoing peridotite alteration in this area. We constrain the igneous history of the mantle rocks, the extent to which they have been hydrated, carbonated and oxidized. Highlights include new hypotheses on mechanisms of shallow sulfur depletion and deeper enrichment, and new insights into the interaction of water and minerals that controls the partial pressures of oxygen and hydrogen in this important geochemical environment.

## 1. Introduction

The Oman Drilling Project (OmanDP) Multi-Borehole Observatory (MBO) lies in the area bounded by latitudes 22.84 to 22.98°N, and 58.58° to 58.76°E (Figures 1, 2 and 3), northeast of the city of Ibra in the Sultanate of Oman, and close to the town of Batin. This area was chosen for drilling to investigate ongoing hydration, carbonation and oxidation of exposed mantle peridotite during near-surface weathering, the associated hydrological system, and the subsurface, chemosynthetic biosphere fostered by weathering of mantle peridotite. Cores collected in the MBO will also be relevant for understanding mantle melt transport, and quantifying the cooling history of the shallow mantle near a spreading ridge. Conversely, cores from the crust-mantle transition zone (MTZ) drill sites CM1A and CM2B in the Wadi Tayin massif, obtained mainly to study near-spreading-ridge igneous, alteration and cooling processes, will shed further light on weathering and the subsurface biosphere in tectonically exposed peridotite.

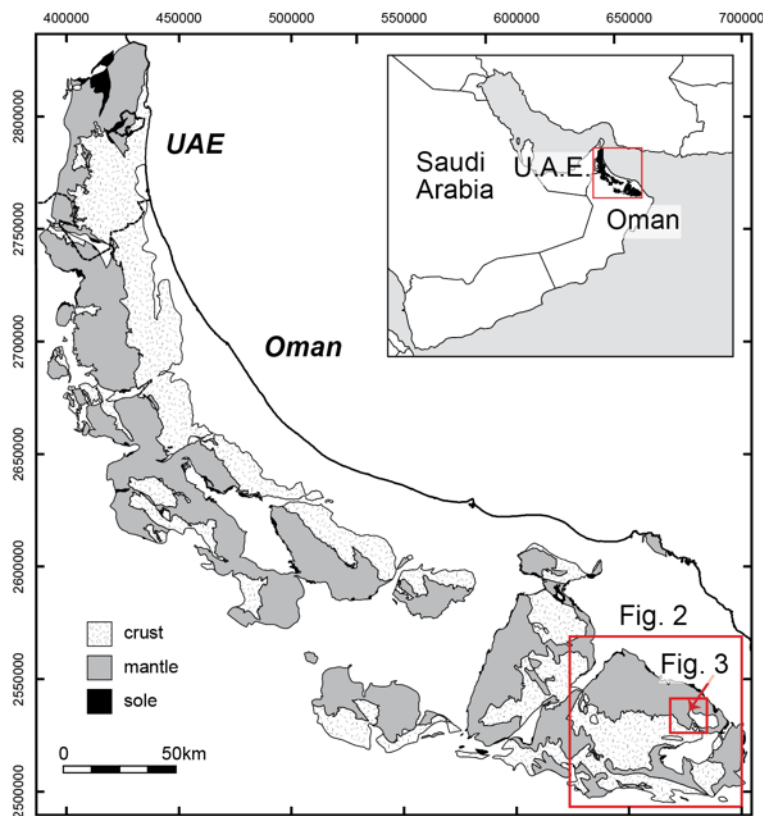


Figure 1: Outcrop area of the Samail ophiolite in Oman and the United Arab Emirates, based on Nicolas *et al.* [2000a]. Red rectangles indicate the approximate location of Figure 2, providing place names used in this paper, and Figure 3, a geologic map of the area that is the focus of this paper. Map coordinates are meters in UTM (Universal Transverse Mercator) Zone 40Q.

Initially, we hoped to conduct drilling of actively altering peridotite in Wadi Dima, west of the present sites, in an area without large faults. However, we were not able to find drill sites more than 3.5 km from the nearest registered “falaj” (irrigation system), as required for permitting. Alternatives were (a) Wadi Laywani, a broad, south-facing drainage about 20 km northeast Batin, and 4 km east of the road from Batin to the village of Dima, and (b) the headwaters of Wadi Mehlah, along the Batin-Dima road. Wadi Mehlah is a long, straight NNW trending valley NNW of Wadi Laywani, parallel to the Batin-Dima road, draining into Wadi Tayin east of Wadi Dima, near its intersection with Wadi Tayin.

Both of these alternative areas lie along a major NW-SE trending fault system that cuts the Samail ophiolite (Figure 4). An advantage of Wadi Laywani is that there had been prior sampling and analysis of water and rock chips from water monitoring wells NSHQ14, NSHQ04, WAB71 and WAB188 in and near that catchment [Miller *et al.*, 2016; Paukert *et al.*, 2012; Paukert Vankeuren *et al.*, 2019; Rempfert *et al.*, 2017]. (The water monitoring wells have been established and maintained by the Oman Ministry of Regional Municipalities and Water Resources, and its precursor and successor organizations).

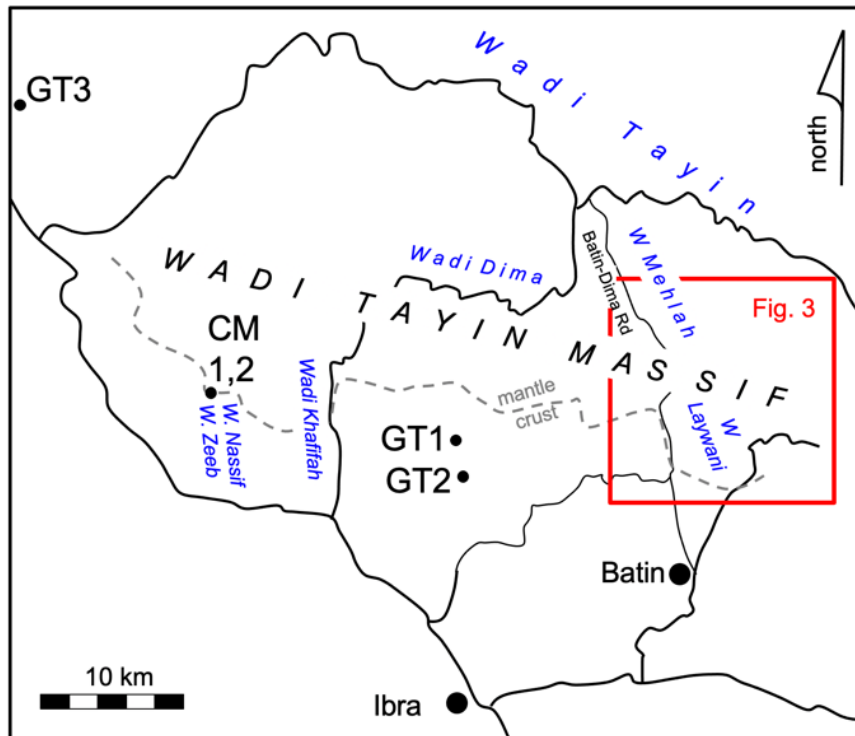
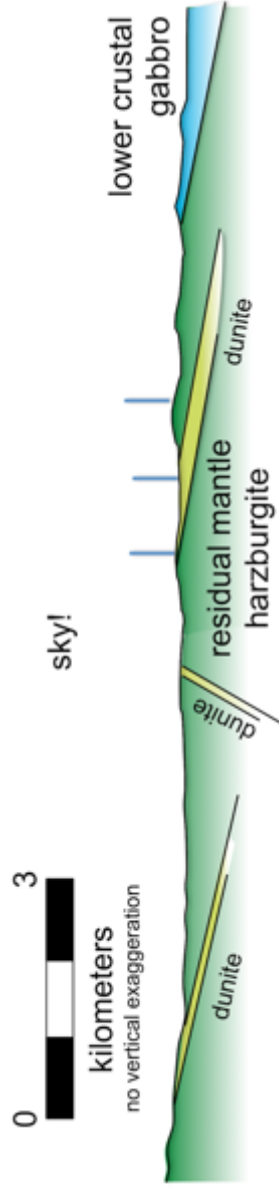
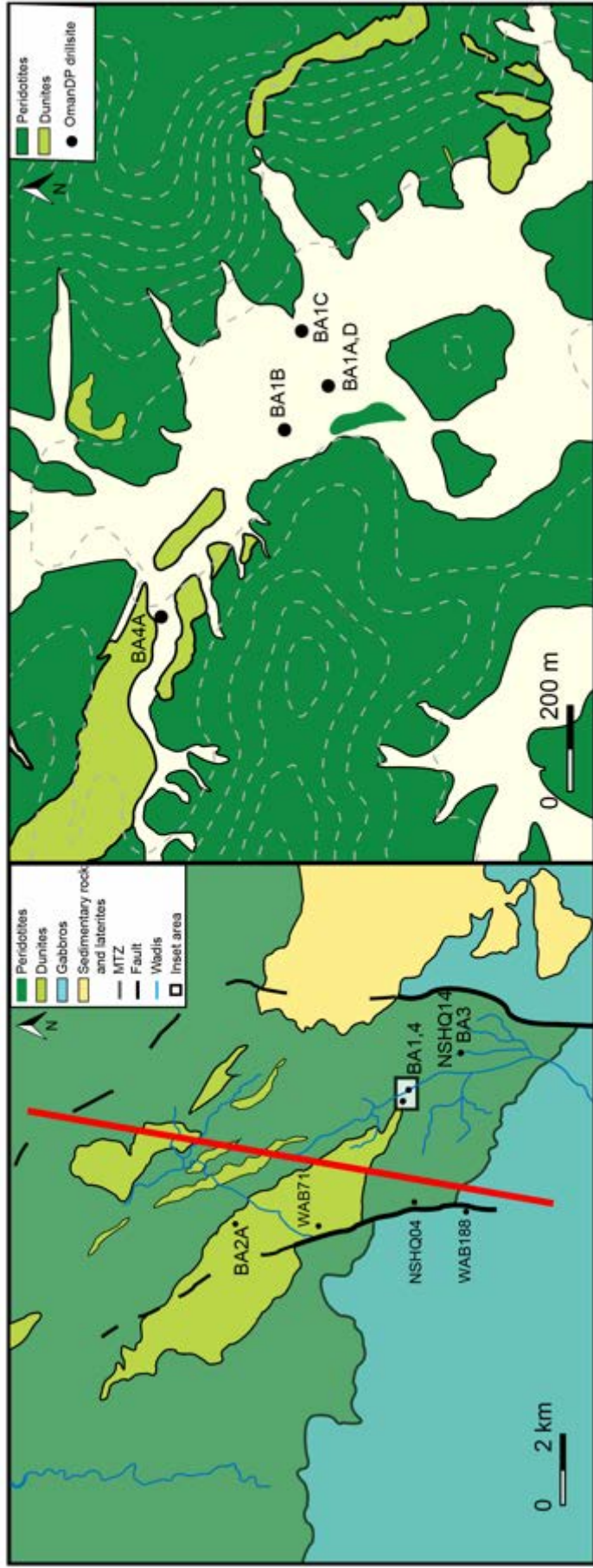


Figure 2: Map showing location of places named in this paper, and the locations of OmanDP Holes GT1 and GT2 (crustal gabbros), GT3 (gabbro-sheeted dike transition), and CM1 and CM2 (crust-mantle transition). Solid lines are roads; thick: paved, thin: gravel. Grey dashed line illustrates the approximate trace of the crust-mantle transition zone in the Wadi Tayin massif of the Samail ophiolite. Red rectangle indicates approximate location of Figure 3.

OmanDP drilling in the MBO area began with reconnaissance, rotary boreholes in each of the two alternative areas in winter 2017. Hole BA1A is in Wadi Laywani. The water table was encountered at a depth of ~ 16 meters. Drill chips indicated that the bedrock was a mix of serpentinized dunite and harzburgite. Hole BA2A is in the headwaters of Wadi Mehlah. Surrounding outcrops and drill chips indicated that the Hole is almost entirely in dunite. Other than the drilling fluid, there was essentially no water in Hole BA2A within its full depth of 400 meters. As a result, in order to ensure the presence of water for lubrication during coring, we decided to drill all subsequent MBO holes in Wadi Laywani.

The MBO includes OmanDP Holes BA1A, BA1B, BA1C, BA1D, BA2A, BA3A and BA4A. (The two letter BA designation in the OmanDP Hole names referred to the location, near Batin, and the focus on Alteration). In addition, we have benefited from access to pre-existing Oman Water Ministry monitoring holes NSHQ04, NSHQ14, WAB71 and WAB188. Among these Holes, BA1B, BA3A and BA4A recovered core via wireline diamond drilling (~ 100% recovery), while cuttings from rotary boreholes BA1A and BA2A were examined by the OmanDP Science Team, and two groups have also studied cuttings and drilling logs from NSHQ14 [Miller *et al.*, 2016; Paukert *et al.*, 2012]. Core was shipped to Japan and loaded onto Drilling Vessel Chikyu, where the OmanDP Science Team performed analyses closely following protocols established by the various incarnations of the Ocean Drilling Program (formerly the Ocean Drilling Program, ODP, and the International Ocean Drilling Program, IODP; currently, the International Ocean Discovery Program, IODP). Detailed core descriptions, together with drilling history and some background information [Kelemen *et al.*, 2021b; c; d; e; f; g; Kelemen *et al.*, 2020g] are available online at [http://publications.iodp.org/other/Oman/VOLUME/CHAPTERS/113\\_BT1.PDF](http://publications.iodp.org/other/Oman/VOLUME/CHAPTERS/113_BT1.PDF)







 peridotite approx 3 km thick  
 overlying allocthanous Hawasina nappes  
 overlying autocthanous Mesozoic to Proterozoic Arabian continental margin

Figure 3: Geologic maps and cross section of the MBO area, based on USGS mapping [Bailey, 1981] and our unpublished observations. Dashed grey lines in righthand map, elevation contours, interval 5 m, from 550 to 590 m asl.

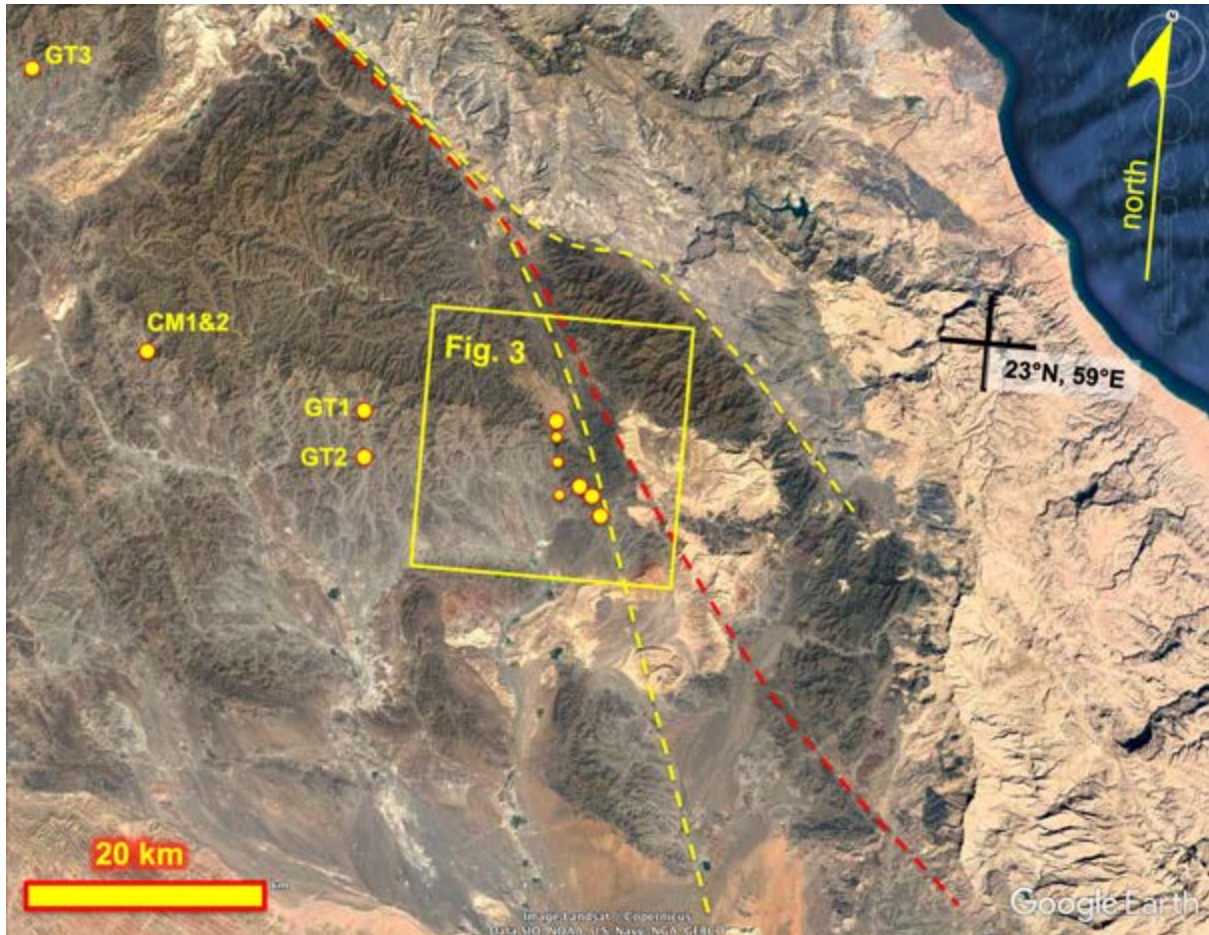


Figure 4: Regional scale fault traces transecting the MBO. Wadi Tayin massif mantle peridotites are dark olive green to brown. Gabbros south of the peridotite are greenish grey. The Saih Hatat dome, exposing Proterozoic to Paleozoic shelf sediments, is the grey area northeast of the Wadi Tayin peridotites. Late Cretaceous to Eocene, shallow marine limestones unconformably overlying all of these units on the east, plus smaller erosional remnants near the center of the image, are tan. Approximate locations of OmanDP Holes GT3A, CM1&2, GT1, GT2, BA2A, BA4A, BA1A-D, and BA3A (plus pre-existing water monitoring well NSHQ14 adjacent to BA3A), listed in order from W to E, are shown as large yellow circles. Approximate locations of other, pre-existing water monitoring wells within the MBO are shown as smaller yellow circles. Yellow versus red colors for inferred fault traces were used simply for visibility.

### 1.1 Regional geology and structure of the MBO and vicinity

The MBO Holes are entirely within partially to completely serpentized peridotite comprising the mantle section of Wadi Tayin massif of the Samail ophiolite. Peridotites in the Wadi Tayin and nearby Samail massif mantle sections record at least one phase of extensive melting and melt-extraction, producing residual harzburgites. The harzburgites record ~ 15 to 20% melt extraction, assuming the protolith had a fertile lherzolite composition and have major and trace element contents very similar to residual mantle peridotites dredged from mid-ocean ridges [M Godard *et al.*, 2000; Hanghøj *et al.*, 2010; Kelemen *et al.*, 1997a; Kelemen *et al.*, 1995a; Monnier *et al.*, 2006].

In the northern massifs of the ophiolite, there are clear indications that two important stages of partial melting and melt transport affected the mantle section, one during upwelling and corner flow in the shallow mantle beneath an oceanic spreading ridge, and a later one producing cross-cutting features. Products of the second stage are relatively rare in the southern massifs of the ophiolite, including Wadi Tayin and the neighboring Samail massif. For example, one characteristic of peridotites strongly affected by the second stage is high Cr# (molar Cr/(Cr+Al)) in spinels, ranging from 0.7 to 0.9 [e.g., Arai *et al.*, 2006; Tamura and Arai, 2006, and references therein]. Such high Cr# is generally taken to indicate the effects of arc magmatism. In contrast, spinels in the southern massifs of the Samail ophiolite show a broad range of more aluminous compositions, with Cr# from ~ 0.2 to 0.73 [e.g., M Godard *et al.*, 2000; Hanghøj *et al.*, 2010; Kelemen *et al.*, 1997a; Kelemen *et al.*, 1995a; Monnier *et al.*

al., 2006], similar to the range in peridotites dredged from the mid-ocean ridges [~ 0.1 to 0.69, *H Dick and Bullen*, 1984; *El Dien et al.*, 2019; *Urann et al.*, 2020]. We don't want to be misunderstood here; the Samail ophiolite lavas, from southern as well as northern massifs, contain a distinct geochemical subduction signature [e.g., *Alabaster et al.*, 1982; *MacLeod et al.*, 2013; *Pearce et al.*, 1981; *Pearce and Peate*, 1995]. Conversely, the samples with highest Cr# spinels dredged from the Mid-Atlantic Ridge have been attributed to the presence of a fragment of depleted arc lithosphere beneath the ridge [*Urann et al.*, 2020]. However, there is little evidence for a profound difference in melt generation and extraction processes, when comparing mid-ocean ridge peridotites with Samail ophiolite peridotites from the southern, Wadi Tayin and Samail massifs in Oman.

The Wadi Tayin massif is one of the largest and most intact massifs in the ophiolite. A well-exposed crustal section in the "Ibra syncline", about 7 km thick from seafloor pillow lavas to the mantle-crust transition zone (MTZ), has been the subject of many detailed studies [e.g., papers in *Bieseler et al.*, 2018; *Bosch et al.*, 2004; *Boudier et al.*, 1996; *Coleman and Hopson*, 1981; *Coogan et al.*, 2006; *Currin et al.*, 2018; *France et al.*, 2009; *Garrido et al.*, 2001; *Kelemen and Aharonov*, 1998; *Kelemen et al.*, 1997b; *Koga et al.*, 2001; *Korenaga and Kelemen*, 1997; *Mock et al.*, 2021; *Müller et al.*, 2017; *Nicolas et al.*, 2003; *Oeser et al.*, 2012; *Peucker-Ehrenbrink et al.*, 2012; *Rajendran and Nasir*, 2019; *Rioux et al.*, 2012; *VanTongeren et al.*, 2015; *VanTongeren et al.*, 2008; *Zihlmann et al.*, 2018]. OmanDP Holes GT1A and GT2A, drilled in winter 2017, sampled lower crustal gabbros in this section, while Hole GT3A sampled the sheeted-dike to upper gabbro transition in a nearby part of the Samail massif [*Kelemen et al.*, 2020b; d; e; f]. The MTZ of the Wadi Tayin massif is exposed in outcrop in several places, including Wadi Nassif and the smaller, adjacent Wadi Zeeb. The latter was the site of Holes CM1A,B, and CM2A,B in late fall 2017, which provided a complete core sample through the transition zone [*Kelemen et al.*, 2021a; h; i]. The MTZ dips 20 to 30° SSW along the strike length of the Wadi Tayin massif [*Bailey*, 1981; *Nicolas et al.*, 2000a].

If there has been no tectonic thinning or thickening, then the thickness of the mantle section – perpendicular to the MTZ and the paleo-seafloor – ranges from 10 to 20 km below the base of the crust [*Boudier and Coleman*, 1981], yielding a maximum thickness for the entire Wadi Tayin massif of ~ 25 km. At the base of the mantle section throughout the ophiolite is the trace-element-enriched "Banded Unit", composed of 1 to 10 m scale bands of harzburgite, dunite and rare lherzolite, overlying a metamorphic sole composed mainly of amphibolites [*M Godard et al.*, 2000; *Khedr et al.*, 2013; *Khedr et al.*, 2014; *Takazawa et al.*, 2003; *Yoshikawa et al.*, 2015]. Locally, the Wadi Tayin Banded Unit includes mylonitic shear zones, which formed at an inferred temperature of 700-1000°C [*Boudier et al.*, 1988; *Boudier and Coleman*, 1981]. This sequence is characteristic of the base of the most complete, best-exposed sections throughout the Samail ophiolite, where the underlying metamorphic sole is preserved. The metamorphic sole in Wadi Tayin records peak metamorphism at ~ 700-900°C and ~ 1.2 GPa [e.g., *Cowan et al.*, 2014; *Hacker and Mosenfelder*, 1996; *M Searle and Cox*, 2002; *M P Searle and Malpas*, 1980; *Soret et al.*, 2017], roughly consistent with the thickness estimate and deformation temperature inferred for the base of the Wadi Tayin peridotite section.

The MTZ and surrounding crust and mantle are cut and displaced by several kilometers along a set of NNW trending, strike-slip faults [*Bailey*, 1981; *Nicolas et al.*, 2000a]. In the MBO area, these have a right lateral sense of displacement. Perhaps related to these smaller features, a 10- to 50-km-scale NNW trending fault system evident in satellite imagery cuts all the way across the Wadi Tayin massif in Wadi Laywani (draining south) and Wadi Mehlah (draining north) (Figure 4). The sense of displacement along this larger fault system has not been determined, but it is possible that it too is a right-lateral, strike-slip fault.

Near the western end of the Wadi Tayin massif, a large strike-slip fault shows left lateral displacement of the MTZ along Wadi Khafifah. This continues as a ductile shear zone extending several kilometers into the mantle section [*Nicolas and Boudier*, 2008]. Along this shear zone, deformation was localized in gabbroic dikes within the mantle [*Homburg et al.*, 2010]. Strongly deformed gabbroic dikes are also observed in outcrop in the MBO region. Ductile deformation of the dikes may be related movement along the large fault system; if so, the faults became active while the mantle section of the Wadi Tayin massif was still at high temperature, though deformation has apparently continued into the low-temperature, brittle regime.

Normally, Samail ophiolite peridotites have a foliation that is approximately parallel to the MTZ and the paleo-seafloor [e.g., synoptic cross-sections in *Lippard et al.*, 1986; *Nicolas et al.*, 1988]. A



peculiar structural relationship has been observed – but rarely documented in publications – across central parts of the Wadi Tayin mantle section, in which peridotite foliation – marked by faint, pyroxene-rich banding – dips steeply with respect to the shallow dip of the MTZ [e.g., *Boudier and Coleman*, 1981, their Figure 2]. Despite this steep foliation, dunite-harzburgite contacts have a low dip, approximately parallel to that of the MTZ, and spinel lineation within the steeply dipping peridotite foliation has a low inclination.

Perhaps fortunately, indications from surface mapping and drill site observation of core are that peridotite foliation at the MBO sites has a shallow dip, approximately parallel to the MTZ exposed in east facing outcrops on ridges forming the west side of Wadi Laywani, SW of Site BA3, as illustrated in the widely used, synoptic cross-sections of the Samail ophiolite. Here, we simply mention the odd geometry of foliation and lineation further west in the Wadi Tayin massif, because it may be important in future syntheses of drilling results and surface observations.

### *1.2 Mantle dunites in the MBO and vicinity*

Geological mapping in the late 1970's identified two particularly large dunite bodies in the Wadi Tayin mantle section, within depleted, residual mantle harzburgite [*Bailey*, 1981]. The dunites dip 20 to 30° SSW, approximately parallel to the overlying MTZ. Kelemen et al. [2000, their Table 1] measured the thickness of the northeastern dunite body, perpendicular to top and bottom contacts with harzburgite, to be ~ 70 meters, in the range of other large mantle dunites in the Samail ophiolite. More extensive size-frequency data on mantle dunites are reported by Braun & Kelemen [2002].

Unpublished observations by Peter Kelemen, and later by Bob Miller (California State University, San Jose) confirmed the SSW dip of the southwestern dunite body at its thin, northwestern tip, where it is about 2 km below the MTZ. However, there have been no estimates of its thickness in its central region, at Site BA2 for example, due to faulting and irregular contacts.

Between the two large, SSW dipping dunites is a zone containing of thinner dunites, up to 20 m wide, with steep NNE dips (Figure 3). This NW striking zone is approximately coincident with the Batin – Dima road, and not more than 3 km wide. This zone may be the locus of steeply inclined spinel lineations reported by Nicolas et al. [*Nicolas et al.*, 2000b], who interpreted such steep lineations as indicative of the presence of “mantle diapirs”.

One potential explanation for these relationships – with shallow dunites to the SW and NE, flanking a central zone of steeply dipping dunites, is that the central dunites represent a frozen zone of mantle upwelling beneath a spreading center, whereas the MTZ parallel dunites to the NE and SW have been transposed by corner flow on either side of the ridge. However, given that the Wadi Tayin massif, and overlying Late Cretaceous to Eocene limestones, are clearly faulted and tilted within the area of the left panel in Figure 3, it is not clear whether features within the mantle section retain their structural orientation, with respect to each other and to the crust-mantle transition zone (MTZ). Thus, the narrow zone of steep dunites could be a preserved relict of the upwelling zone in the mantle beneath a spreading center, or the result of post-emplacement, tectonic rotations within the Wadi Tayin massif.

As is evident from geologic mapping, Sites BA2 and BA4 lie within the outcrop of the southeastern tip of the large, shallowly SSW dipping dunite body, and most Holes in Site BA1 – in gravels within Wadi Laywani – also intersect that large dunite (Figure 5). On site observations of drill cuttings [*Kelemen et al.*, 2021e] indicate that the entire 400 meter Hole BA2A is within massive dunite. Assuming a SW dip of 25 to 30 degrees parallel to the MTZ, this indicates that the dunite at Site BA2A is more than 350 meters thick, perpendicular to the MTZ. As such, it is more than three times thicker than the next thickest dunite in the mantle section of the Samail ophiolite, as measured by Kelemen et al. [2000, their Table 1].

Core from Hole BA4A, and surrounding outcrops, are composed of alternating bands of dunite and harzburgite [*Kelemen et al.*, 2021g], rather than the more massive dunites in outcrop further to the NW. However, to the SE, Holes BA1A, B, C and D again intersected the large dunite body, where it is massive, containing only a few thin harzburgite lenses, ~ 100-200 m thick, and about 2 km structurally beneath the MTZ [*Kelemen et al.*, 2021d]. The upper 150 meters of core from Hole BA1B was largely composed of dunite, with relatively few harzburgite bands. The large dunite may or may not extend



across Wadi Laywani. Approximate logs based on drill cuttings suggest that the top of Hole BA1C intersected ~ 100 m of dunite near the east side of the Wadi, and a few relatively thin, SSW dipping dunite lenses can be seen on WSW facing-outcrops flanking the Wadi to the east (Figure 3). If the overall, thick dunite unit does cross the Wadi, this places an upper bound of a few hundred meters on displacement along the fault zone(s) within Wadi Laywani.

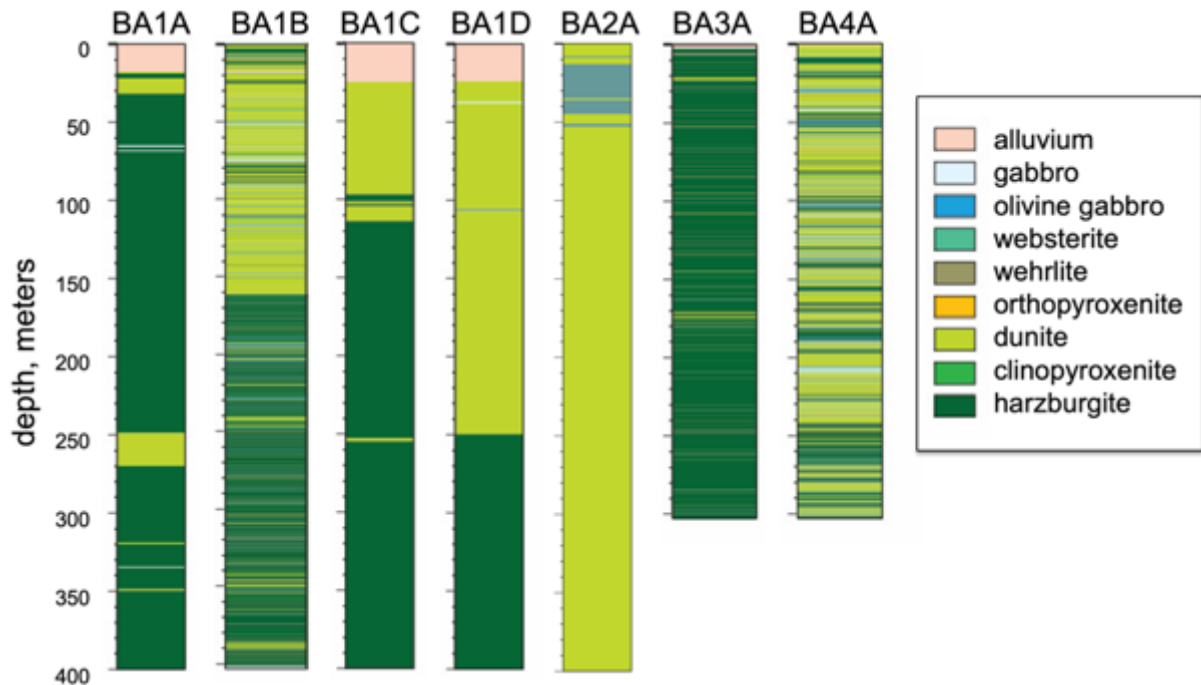


Figure 5: Lithologic columns based on analysis of drill core from Holes BA1B, BA3A and BA4A, and drill cuttings from Holes BA1A, BA1C, BA1D and BA2A, from Kelemen *et al.* [2021d; e; f; g].

Dunites in the mantle section of ophiolites – and by inference in the mantle beneath oceanic spreading ridges – are generally understood to be the products of reaction between olivine-saturated melt – ascending by porous flow along crystal grain boundaries – and shallow mantle harzburgites. Orthopyroxene from the harzburgite dissolves in the ascending, decompressing melt, producing olivine + melt, and this leads to formation of dunites in channels of focused porous flow [e.g., Aharonov *et al.*, 1995; J L Bodinier, 1988; Kelemen, 1990; Kelemen *et al.*, 1995a; Kelemen *et al.*, 1995b; Quick, 1982]. Typically, unless modified by subsolidus, low temperature Fe/Mg exchange with spinel, olivine in mantle dunites has about the same composition (Mg#, molar Mg/(Mg+Fe), ~ 0.91) as in the surrounding harzburgites [Kelemen, 1990], consistent with formation of dunite by reaction, rather than as the residue of extensive partial melting and melt extraction [e.g., as advocated by Benoit *et al.*, 1999; Rospabé *et al.*, 2017], or as newly crystallized magmatic rocks [“cumulate dunites”, e.g., Rollinson, 2019].

As melt approaches the surface and begins to cool, it will begin to undergo crystallization and accompanying chemical fractionation, potentially producing olivine with a lower Mg#. If it continues to react with mantle peridotite, open system processes will buffer the composition of cooling melt to various degrees, in a process termed “reactive fractionation” [Abily and Ceuleneer, 2013; Collier and Kelemen, 2010]. This process can produce trends typical of reaction between fractionating melt and mantle peridotite with increasing incompatible element concentrations at nearly constant compatible element concentrations [e.g., Kelemen, 1986; 1990]. Using major elements alone, diagnostic characteristics of dunites and “troctolites” (plagioclase bearing dunites and impregnated peridotites) produced by reactive fractionation are nearly constant Ni content over a range of Mg#, together with a wide range of Ca# (molar Ca/(Ca+Na), also known as normative anorthite content), as emphasized in several studies of “impregnated dunites” and “troctolites” recovered via dredging and drilling along the mid-ocean ridges, and outcrop sampling in ophiolites [Arai and Matsukage, 1996; Basch *et al.*, 2018; 2019; Brunelli *et al.*, 2006; Collier and Kelemen, 2010; H J Dick and Natland, 1996; Drouin *et al.*, 2009; Drouin *et al.*, 2010; Ferrando *et al.*, 2018; Gillis *et al.*, 2014; M. Godard *et al.*, 2009; Kelemen *et*

*al.*, 2004; Kelemen *et al.*, 2007; Seyler and Bonatti, 1997; Seyler *et al.*, 2007; Suhr *et al.*, 2008; Takazawa *et al.*, 2007; Tartarotti *et al.*, 2002].

### 1.3 Mantle dikes in the MBO and vicinity

Cutting the dunite around the MBO sites are numerous, tabular gabbroic and pyroxenite dikes. It is qualitatively evident that the dikes are more numerous than is typical in the mantle section of the Samail ophiolite, though this has not yet been quantified. The dikes range from fine-grained to pegmatoidal, and may be an important source of calcium and, locally, aluminum during alteration and weathering of the peridotite. It is not clear why there is an unusual number of dikes in the vicinity of the MBO. However, the presence of dikes in the mantle section of the Samail ophiolite is common. A late set of gabbronorite and websterite dikes cutting mantle peridotite foliation and dunite contacts occurs throughout the ophiolite [Benoit *et al.*, 1999; Benoit *et al.*, 1996; Ceuleneer *et al.*, 1996; Kelemen *et al.*, 1997a; Python and Ceuleneer, 2003]. Geochemical characteristics of these dikes indicate that they are not related to the magmas that formed the overlying crust, and could be formed from small amounts of late, shallow melts of residual mantle harzburgite [Kelemen *et al.*, 1997a]. They could be related to large websterite and gabbronorite intrusions into the mantle and crust in the northern massifs of the ophiolite [summary in Python and Ceuleneer, 2003; Smewing, 1981]. Less commonly (but not far away, in the Samail massif of the ophiolite), there are also olivine gabbro and troctolite dikes in the mantle, which could have crystallized from the same kind of magmas that formed most of the crust [Ceuleneer *et al.*, 1996; Python and Ceuleneer, 2003]. Because almost all of the dikes in the MBO area have been substantially altered to calc-silicate, “rodingite” assemblages during serpentinization, it is not yet clear which kinds of lithologies predominate in the dike swarm around the BA sites.

### 1.4 Post-emplacement alteration of the MBO and vicinity

Emplacement of the ophiolite, and the underlying, allochthonous Hawasina Formation, onto the Arabian continental margin, followed by subaerial weathering of the ophiolite, was complete by about 74 Ma, based on the age of the oldest sediments overlying an erosional unconformity at the top of the ophiolite section [S Al Khirbash, 2015; Alsharan and Nasir, 1996; Bailey, 1981; Hansman *et al.*, 2017; Nolan *et al.*, 1990; Schlüter *et al.*, 2008; Wyns *et al.*, 1992]. Extensive erosion of the eastern part of the Wadi Tayin massif exposed mantle peridotite at the surface, locally forming laterites in a discontinuous band that extends to ~ 3 km E of Sites BA1, 3 and 4 [S Al Khirbash, 2015; S A Al Khirbash, 2016; 2020], and well exposed erosional surfaces overlain by peridotite conglomerates in erosional windows near the coast east and northeast of Wadi Tayin [de Obeso and Kelemen, 2018; 2020]. After marine transgression, Late Cretaceous and Tertiary shallow water sediments were deposited unconformably on the peridotites in this area [Alsharan and Nasir, 1996; Hansman *et al.*, 2017; Nolan *et al.*, 1990]. As a result of this history, without careful study, it is not immediately clear how much of the low temperature alteration of the peridotite in the MBO, and in the Wadi Tayin massif more generally, may have occurred in the Late Cretaceous, and how much is related to more recent, ongoing weathering. Noël *et al.* [Noël *et al.*, 2018] propose that the stable isotope characteristics of some serpentinites record “high” alteration temperatures consistent with early alteration near the axis of the spreading ridge that formed the ophiolite crust, and/or during early stages of ophiolite emplacement. However, we regard this result as uncertain, because their inferred alteration temperatures (~ 115-10°C) are lower than the temperature in the shallow mantle beneath oceanic crust (~100°C at the Moho in ocean crust > 60 million years old, hotter in younger crust) and temperatures at the base of the crust during metamorphism of the metamorphic sole (800-900°C at ~ 40 km, so more than 140°C at 7 km).

Turning attention from the MBO region to the Samail ophiolite in general, studies of low temperature peridotite alteration in the mantle section of the Samail ophiolite have been more limited than studies of mantle melting and melt transport, and studies of oceanic crustal formation and alteration. Early work by Barnes *et al.* [1978] and Neal, Stanger and their colleagues [Neal and Stanger, 1983; 1984; 1985; Stanger and Neal, 1994] focused on the production of hyperalkaline spring water and H<sub>2</sub>-rich gas during peridotite weathering, further refining the insights of Barnes and O’Neil [1969] that were based on observations of similar systems in California. Stanger and colleagues also wrote papers about unusual minerals formed in low temperature weathering of peridotite in Oman [Stanger *et al.*, 1988; Stanger and Neal, 1994; Taylor *et al.*, 1991]. Boudier and colleagues investigated seismic anisotropy in partially serpentinized peridotites from Oman and other regions [Boudier *et al.*, 2010;

Dewandel *et al.*, 2003]. Clark and Fontes and co-workers investigated travertine deposits forming at peridotite-hosted, alkaline springs [1990].

Three relatively recent developments led to increased interest in specific aspects low temperature alteration of peridotite, in the Samail ophiolite and worldwide. First, there has been widespread recognition that highly reducing environments and large redox gradients produced during serpentinization [e.g., Frost, 1985] can stabilize hydrocarbons and provide energy for microbial chemosynthesis, leading to an explosion of hypotheses concerning the subsurface biosphere, abiotic hydrocarbon genesis, and the origin of life on this and other planets [e.g., Berndt *et al.*, 1996; Ehlmann *et al.*, 2010; Ehlmann *et al.*, 2009; Etiope *et al.*, 2013; Fisk and Giovannoni, 1999; Foustoukos and Seyfried, 2004; Frost and Beard, 2007; Horita and Berndt, 1999; Martin *et al.*, 2008; Martin and Russell, 2007; McCollom, 1999; 2007; Russell *et al.*, 2010; Schulte *et al.*, 2006; Shock, 1997; Shock *et al.*, 1995; Sleep *et al.*, 2011; Sleep *et al.*, 2004; Varnes *et al.*, 2003]. There has been a substantial amount of work on the Samail ophiolite related to this topic [Boulart *et al.*, 2013; Boyd *et al.*, 2020; Canovas *et al.*, 2017; de Obeso and Kelemen, 2018; 2020; Ellison *et al.*, 2021; Fones *et al.*, 2019; Fones *et al.*, 2021; Glombitza *et al.*, 2021; Kraus *et al.*, 2021; J A Leong *et al.*, 2021a; J A M Leong *et al.*, 2021b; J A M Leong and Shock, 2020; L.E. Mayhew *et al.*, 2018; Miller *et al.*, 2016; Newman *et al.*, 2020; Nothaft *et al.*, 2021a; Nothaft *et al.*, 2021b; Rempfert *et al.*, 2017; Sano *et al.*, 1993; A Templeton *et al.*, 2021; Vacquand *et al.*, 2018].

Second, it has been proposed that formation of carbonate minerals via reaction of surface waters with peridotite can produce a significant carbon reservoir on this and other planets, and could potentially be emulated in accelerated systems for engineered carbon capture and storage [e.g., Kelemen and Matter, 2008]. There have been numerous, related studies of carbon mineralization during natural weathering of peridotite in the Samail ophiolite [Chavagnac *et al.*, 2013a; Chavagnac *et al.*, 2013b; Falk *et al.*, 2016; Giampouras *et al.*, 2020; Kelemen *et al.*, 2011; Lacinska and Styles, 2013; Lacinska *et al.*, 2014; Leleu *et al.*, 2016; Mervine *et al.*, 2014; Mervine *et al.*, 2015; Noël *et al.*, 2018; Paukert *et al.*, 2012; Paukert Vankeuren *et al.*, 2019; Rajendran and Nasir, 2019; Rajendran *et al.*, 2014; Streit *et al.*, 2012], elsewhere on Earth [e.g., Alt *et al.*, 2013; Alt *et al.*, 2012; Andrews *et al.*, 2018; Arcilla *et al.*, 2011; Beinlich *et al.*, 2010; del Real *et al.*, 2016; Gahlan *et al.*, 2020; Manuella *et al.*, 2019; Morrissey and Morrill, 2017; Oskierski *et al.*, 2013a; Oskierski *et al.*, 2013b; c; Picazo *et al.*, 2020; Benoît Quesnel *et al.*, 2016; Benoît Quesnel *et al.*, 2013; Sánchez-Murillo *et al.*, 2014; Schwarzenbach *et al.*, 2016; Schwarzenbach *et al.*, 2013; Ulrich *et al.*, 2014], and on Mars [e.g., Edwards and Ehlmann, 2015; Ehlmann and Edwards, 2014; Ehlmann *et al.*, 2008; Kelemen *et al.*, 2020a; Salvatore *et al.*, 2018; Tarnas *et al.*, 2021; Tomkinson *et al.*, 2013]. References listed here are in addition to studies of carbon mineralization - forming completely carbonated "listvenites" - at the base of the Samail ophiolite mantle section and elsewhere on Earth, summarized in a companion paper to this one [Kelemen *et al.*, 2021] on OmanDP Hole BT1B, which sampled Cretaceous listvenites at the "leading edge of the mantle wedge", which formed just above the basal thrust of the ophiolite during subduction and obduction of carbon-bearing sediments

Third, there has been renewed focus on the volume changes associated with hydration, carbonation and oxidation of peridotite during weathering, as originally addressed by MacDonald and Fyfe [1985], O'Hanley [1992] and Evans [2004], and on the ways in which these volume changes may be accommodated [O Evans *et al.*, 2018; 2020; Iyer *et al.*, 2008; Jamtveit *et al.*, 2009; Kelemen and Hirth, 2012; Klein and Le Roux, 2020; H Lisabeth *et al.*, 2017a; H P Lisabeth *et al.*, 2017b; Malvoisin *et al.*, 2017; Røyne and Jamtveit, 2015; Rudge *et al.*, 2010; Ulven *et al.*, 2014a; Ulven *et al.*, 2014b; Zheng *et al.*, 2019; Zheng *et al.*, 2018; Zhu *et al.*, 2016]. Studies addressing this issue via study of low temperature peridotite weathering in the Samail ophiolite include Kelemen and Hirth [2012], Malvoisin *et al.* [Malvoisin *et al.*, 2020] and Yoshida *et al.* [2020]. More generally, fracture-related frequency, porosity and permeability in serpentinized peridotites has been studied in OmanDP drill core samples by Katayama *et al.* [2020; 2021].

In general, it has been noted that Samail ophiolite mantle peridotite compositions are slightly displaced toward lower Mg/Si compared to inferred and experimentally observed residues of partial melting, and the composition of residual peridotites dredged from mid-ocean ridges [e.g., Monnier *et al.*, 2006, their Figure 5]. This is most evident where peridotites are strongly weathered, and could be due to magnesium extraction [Snow and Dick, 1995], silicon addition [e.g., de Obeso and Kelemen, 2018] or both. Similarly, Mg/Si in drill core from the MBO is low compared to the residues of partial melting and melt as illustrated and discussed in Section 4.3.

### 1.5 Past studies of groundwater composition and hydrology in the MBO and vicinity

Groundwater composition and hydrology in the mantle section of the Samail ophiolite has been a subject of fairly extensive research [Canovas *et al.*, 2017; Chavagnac *et al.*, 2013a; Chavagnac *et al.*, 2013b; Dewandel *et al.*, 2005; Dewandel *et al.*, 2004; Falk *et al.*, 2016; Leleu *et al.*, 2016; J A M Leong *et al.*, 2021b; J A M Leong and Shock, 2020; Lods *et al.*, 2020; Mervine *et al.*, 2014; Mervine *et al.*, 2015; Miller *et al.*, 2016; Monnin *et al.*, 2014; Neal and Stanger, 1985; Noël *et al.*, 2018; Nothaft *et al.*, 2021a; Nothaft *et al.*, 2021b; Paukert *et al.*, 2012; Rempfert *et al.*, 2017]. As described in a classic paper about peridotite-hosted springs in California [Barnes and O'Neil, 1969], groundwater in peridotite catchments in Oman can be divided into two types. MgHCO<sub>3</sub>-rich "Type I" waters, with pH ~ 8.5 to 10, are common in pools and running water in wadis, and in most shallow wells. These waters are thought to be produced by near-surface weathering of the peridotite, dissolving Mg<sup>2+</sup>, together with uptake of CO<sub>2</sub> from the atmosphere to form bicarbonate.

End-member, Ca(OH)<sub>2</sub>-rich, "Type II" waters have pH > 10, and are generally restricted to alkaline springs with associated travertine deposits, and some wells in peridotite. These waters are thought to form via more extensive, perhaps deeper interaction between ground water and peridotite. Mg and CO<sub>2</sub> are lost, due to precipitation of serpentine and carbonate minerals, while Ca<sup>2+</sup> is dissolved along the flow path. The source of Ca<sup>2+</sup> could be the peridotite [e.g., Barnes and O'Neil, 1969], gabbro and pyroxenite dikes [Streit *et al.*, 2012], and/or calcium-carbonate minerals formed during earlier alteration [Noël *et al.*, 2018].

Both Type I and Type II waters, and apparent mixtures of the two, are present in the aquifers of Wadi Laywani. Prior to OmanDP, the presence of Type II waters in monitoring well NSHQ14 was known. Water sampling and geophysical logging of Hole BA1A, drilled in 2017, established that Type 1 waters were also present, particularly at shallow depths, together with relatively fresh, pH 6-8 water at the top of the Hole, which probably represents less modified, recent rainwater. More substantial data on water composition in the MBO are provided in Section 3.5 and discussed in Section 4.4.

Based on a variety of different lines of reasoning, catchment-scale-, Hole-to-Hole scale-, single Hole scale- and core-sample scale-studies have found that permeability in peridotite hosted aquifers in the Samail ophiolite is > 10<sup>-14</sup> m<sup>2</sup> near the surface, and ~ 10<sup>-14</sup> to 10<sup>-15</sup> below ~ 100 m, with considerable Hole to Hole variability in the depth of this transition within the MBO [Dewandel *et al.*, 2005; Dewandel *et al.*, 2004; Katayama *et al.*, 2020; Katayama *et al.*, 2021; Lods *et al.*, 2020].

## 2. Methods

### 2.1 Core description

Cores were curated on the drill site and then described onboard Drilling Vessel (DV) Chikyu. In addition to visual core description, analysis onboard DV Chikyu included whole core measurements of magnetic susceptibility, sound wave speed, density, and natural gamma radiation. In addition, all cores were analyzed for X-Ray Computed Tomography, and the cut core face was photographed at high resolution. Dozens of thin sections of core samples from Holes BA1B, BA3A and BA4A were prepared, at the University of Southampton and onboard DV Chikyu. X-Ray Diffraction (XRD) measurements were made on powdered samples from core, and from drill cuttings from rotary boreholes BA1A, BA2A and NSHQ14. Full thin section photos, in both plane and cross-polarized light, were made onboard DV Chikyu. Petrographic descriptions of each thin section were completed by the shipboard science teams. All of these data are available at Texas A&M University by the International Ocean Discovery Program (IODP): <http://publications.iodp.org/other/Oman/OmanDP.html>, and specifically in Kelemen *et al.* [Kelemen *et al.*, 2021d; e; f; g].

Images of shipboard thin sections of core samples from Hole BA1B were obtained using a scanner onboard DV Chikyu [Kelemen *et al.*, 2021d]. The color of these images was characterized at Lamont Doherty Earth Observatory. Red (R), green (G), and blue (B) values (range 0-255) of whole or part of thin section images were determined using ImageJ [Abramoff *et al.*, 2004]. Redness, greenness, and blueness (range 0-1) was calculated from RGB values, normalized to 255, by subtracting the value of the color of interest with the average of those of the other two colors. Redness and greenness values used in Figure 11 were renormalized to values between 0 and 1 via (observed value – minimum value



for BA1B sections)/(maximum – minimum value for BA1B sections. Total RGB (R+G+B) was calculated to quantify brightness. Another measure for lightness or brightness, luminosity (Y), was calculated using the SMPTE-C (Society of Motion Picture and Television Engineers) RGB luminance values  $Y = 0.21R + 0.72G + 0.07B$ ).

## 2.2 Whole rock geochemistry

Major, minor and trace element analyses, including volatile species CO<sub>2</sub> (all C as CO<sub>2</sub>), H<sub>2</sub>O and total sulfur were made by the OmanDP Science Team onboard Drilling Vessel Chikyu, and during laboratory work at the Université de Montpellier generously done by Marguerite Godard and colleagues to check and complete the “shipboard” geochemical dataset. XRF major and minor element analyses of a subset of samples were also conducted at the University of St. Andrews, which allowed cross-calibration with shipboard whole rock data. Methods used to obtain these data are described in Kelemen et al. [2020c] and results are reported in Kelemen et al. [Kelemen et al., 2021d; f; g], hosted online at <http://publications.iodp.org/other/Oman/OmanDP.html>.

FeO contents of shipboard rock powders from core from Hole BA1A were measured at the Geoscience Laboratories of the Ontario Geological Survey, using methods described online at [https://www.mndm.gov.on.ca/sites/default/files/2021\\_geo\\_labs\\_brochure.pdf](https://www.mndm.gov.on.ca/sites/default/files/2021_geo_labs_brochure.pdf). It is possible that some redox-sensitive minerals became oxidized prior to analysis (for example, brucite may become oxidized in air within a matter of days, Ellison et al. 2021). Fe<sub>2</sub>O<sub>3</sub> contents of our samples were then estimated by subtraction of these FeO contents (recalculated as Fe<sub>2</sub>O<sub>3</sub> from total iron measured as Fe<sub>2</sub>O<sub>3</sub> onboard DV Chikyu. Supplementary Table S1 reports the shipboard geochemical information for Hole BA1B [Kelemen et al., 2021d], plus FeO contents.

Normative “igneous” mineralogy for gabbroic samples in core from Hole BA4A was calculated from the bulk compositions using a standard CIPW norm, assuming all Fe as FeO since magnetite was not reported to be abundant in these samples. Normative serpentinite mineralogy for dunite and harzburgite samples in core from Hole BA1A, in terms of Ca-Mg-Fe carbonates, Mg-FeII lizardite, Mg-Fe brucite, and either FeIII cronstedtite or Fe(OH)<sub>3</sub>, was calculated by mass balance, using measured SiO<sub>2</sub>, CO<sub>2</sub>, CaO, MgO, FeO, and Fe<sub>2</sub>O<sub>3</sub> contents of our samples, “projected” from other elements. Mg and Fe<sup>2+</sup> were treated identically, so that lizardite, brucite, magnesite and cronstedtite all had the same Mg/(Mg+Fe<sup>2+</sup>). All CaO was assigned to calcite. Remaining CO<sub>2</sub> was assigned to magnesite. All Fe<sup>3+</sup> was assigned to either cronstedtite or Fe(OH)<sub>3</sub>. The normative proportions of these minerals were used to calculate a maximum weight percent H<sub>2</sub>O, if all Mg and Fe in the rocks were in carbonates plus hydrous minerals, for comparison to observed H<sub>2</sub>O contents in the samples. The resulting serpentinite norms are also included in Supplementary Table S1.

## 2.3 Electron microprobe analyses of minerals

Compositions of minerals in polished thin sections were quantitatively analyzed using a 5-spectrometer Cameca SX-100 electron microprobe (EMP) at the American Museum of Natural History (AMNH). Calibration was performed using in-house natural and synthetic standards. A grain of San Carlos olivine was measured multiple times as unknowns during the experimental run (n=9) with all major elements within error of the known composition. Semi-quantitative elemental maps of Ni and S were obtained by electron dispersive spectroscopy (EDS) using the new 5-spectrometer Cameca SX5-Tactis at AMNH, operating conditions were 15kV and 40nA. Images were post-processed using Apple Color-Sync Utility to increase exposure and sharpness. Atomic units of major elements in minerals were calculated from wavelength dispersive spectroscopy (WDS) data. Values for chlorite and serpentine were calculated assuming 14 and 7 oxygen atoms per formula unit, respectively. For chlorite minerals (including amesite), Fe<sup>3+</sup> atoms per formula unit were calculated assuming no site vacancies. Electron microprobe WDS data used to calculate mineral compositions are provided in Supplementary Table S2.

## 2.4 Analysis of carbonate veins

Carbonate mineral identification by X-Ray diffraction (XRD) was performed at Lamont Doherty Earth Observatory (LDEO) using an Olympus BTX-II XRD analyzer. Diffractograms were analyzed using Match! Software.

For Sr isotope analysis of carbonate veins, carbonate powder was dissolved in glacial acetic acid. To remove any remaining acetic acid the solution was dried, dissolved in HNO<sub>3</sub> and redried. The residue was redissolved in 3N HNO<sub>3</sub> prior to column chemistry using the Eichrom® Sr resin. Purified Sr splits were analyzed for isotopic compositions with the standard bracketing method using the US National Institute of Standards and Technology (NIST) SRM 987 on a Thermo Scientific Neptune multi-collector ICP-MS at Lamont Doherty Earth Observatory (LDEO). In-run mass fractionations were normalized to <sup>86</sup>Sr/<sup>88</sup>Sr=0.1194. Unknowns were normalized to SRM 987 <sup>87</sup>Sr/<sup>86</sup>Sr value of 0.701248. International standards BHVO-2 yielded <sup>87</sup>Sr/<sup>86</sup>Sr value of 0.703474±20 (2s, n = 2) and BCR-2 yielded 0.705010±18 (2s), which agree with published values from Weis et al. [2006].

Radiocarbon analysis were performed at The National Ocean Sciences Accelerator Mass Spectrometry (NOSAMS) facility at Woods Hole Oceanographic Institution, using methods described online at <https://www2.whoi.edu/site/nosams/>. We sent clean but not etched, carbonate fragments to NOSAMS, where they performed a pre-etch in 10% hydrochloric acid at room temperature to remove modern atmospheric CO<sub>2</sub> adsorbed on mineral surfaces.

Additional analyses of δ<sup>13</sup>C, together with δ<sup>18</sup>O, in carbonate minerals, were performed at LDEO using a Thermo-Fisher Delta V+ mass spectrometer with dual-inlet and Kiel IV carbonate reaction device. Powdered carbonate samples were acidified in the Kiel IV device using ~105% H<sub>3</sub>PO<sub>4</sub> at 70C for 10 min before transferring the CO<sub>2</sub> to the Delta V+. The standard deviation of NBS-19 standards analyzed (n=6) was 0.03‰ for δ<sup>13</sup>C and 0.06‰ for δ<sup>18</sup>O.

Isotope ratio data on carbonate veins are reported in Supplementary Table S3.

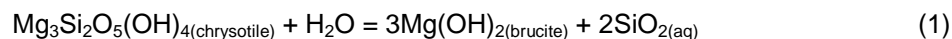
## 2.5 Thermodynamic modeling of water/rock reaction

Simulations of water-rock interactions used the speciation and reaction-path code, EQ3/6 [T Wolery and Jarek, 2003; T.J. Wolery, 1992]. Reaction progress of the water-rock interaction process is quantified by decreasing the water-rock mass ratio (W/R), and simulates a given mass of fluid reacting with an increasing mass of rock as it infiltrates an aquifer. A global average rainwater composition compiled by Hao et al. [Hao et al., 2017] from Berner and Berner [Berner and Berner, 2012] was used in the models. The composition of average harzburgite used in the simulations was calculated from the data of Hanghoj et al. [Hanghoj et al., 2010], including average Cu (20 ppm) and Ni (2000 ppm). We used 300 ppm total sulfur in the reacting harzburgite, which is higher than the range of 6 to 100 ppm measured by Hanghoj et al., but in the 100-500 ppm range measured by Oeser et al. [Oeser et al., 2012] in Samail ophiolite peridotites. Compositions of reacting rainwater and harzburgites are shown in Supplementary Table S4.

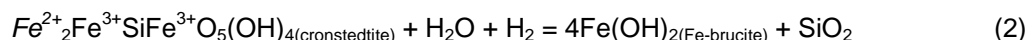
The thermodynamic data used in the simulations are from Klein et al. [2013]. They include data for relevant oxides, sulfides, native metals, and alloys from Klein and Bach [2009], Klein et al. [2009], Helgeson et al. [1978], Leong and Shock [2020] and Wolery and Jove-Colon [2004], and aqueous fluid values from Shock and Helgeson [1988], Shock et al. [1977], and Sverjensky et al. [1997] calculated using the SUPCRT code [Johnson et al., 1992]. The database allows formation of serpentinization-relevant minerals in ideal-site solid solutions and has been successfully used in previous works [de Obeso and Kelemen, 2020; Klein et al., 2009; Klein et al., 2013].

As with Bruni et al. [2002], Paukert et al. [2012] and Leong et al. [2021b], thermodynamic simulations were divided into two steps, both at 35°C. The first step involved reaction of rainwater with peridotites open to the atmosphere from water-rock ratios 10,000 to 10 (i.e., reaction of 1 kg of rock in 10 kg water). The second step involved reaction of fluids generated at the end of first step with the same peridotite, closed to atmospheric input. The first step simulated reactions close to the surface while the second step modeled reactions in deeper aquifers. In contrast to Paukert et al. [2012] and Leong et al. [2021b], first step simulations in this work were allowed to run to higher reaction progress (i.e, towards lower W/R ratio, down to ~10) until modeled dissolved sulfate concentrations approximate field constraints before proceeding to the second step. Results of calculations are shown in Figure 29, for the first and second steps, respectively, and in Supplementary Table S4. The first step produced fluids with composition similar to natural, Mg-HCO<sub>3</sub>-rich "Type I" fluids from shallow peridotite aquifers, while the second step yielded fluids with compositions similar to Ca-OH-rich "Type II" fluids found at peridotite-hosted alkaline springs and deep boreholes, as originally outlined in the classic paper of Barnes and O'Neil [Barnes and O'Neil, 1969].

Using a comprehensive compilation of published data on fluids from peridotite-hosted springs and wells in the Samail ophiolite, the extent of disequilibrium (in kilojoules per mole) between these fluids and chrysotile and brucite was calculated using EQ3/6 with the same thermodynamic data as above, with oxygen fugacities calculated using the published Eh, pH and temperature data [Canovas *et al.*, 2017; J A M Leong *et al.*, 2021b; Nothhaft *et al.*, 2021a; Nothhaft *et al.*, 2021b; Paukert *et al.*, 2012; Paukert Vankeuren *et al.*, 2019; Rempfert *et al.*, 2017]. Results are shown in Supplementary Figure 1. In addition, the extent of disequilibrium for the chrysotile-brucite reaction



and the cronstedtite-ferrous brucite (or ferrous hydroxide) reaction



were also calculated for the compiled data on Samail ophiolite fluids, with results shown in Supplementary Figure 2. In Supplementary Figures 1 and 2, values with positive  $\Delta G_r$  indicate that the reactant side of the reaction is favored, *i.e.*, brucite is metastable with respect to serpentine in all of the peridotite-hosted fluids analyzed so far. Continuing in this theme, we calculated  $f\text{O}_2$  for these fluids, using measured Eh, pH and temperature, as outlined in Section 2.6. While some of the most reduced fluids closely approach (on a log scale!) the low  $f\text{O}_2$  limit where water breaks down to form  $\text{H}_2$ ,  $2\text{H}_2\text{O} = 2\text{H}_2 + \text{O}_2$ , no fluids sampled so far are calculated to be saturated in  $\text{H}_2$  gas (Supplementary Figure 3), consistent with the observation that to date, no gas tight samples from deep boreholes have been  $\text{H}_2$  saturated, though a few have dissolved  $\text{H}_2$  concentrations within a factor of 10 of the saturation value at a the depth of sampling (Hoelher, pers. comm. 2021).

$f\text{O}_2$  and  $f\text{S}_2$  values set by assemblages composed of oxides, sulfides, alloys and native metals were calculated using the same thermodynamic data as above. An  $f\text{O}_2$  vs  $f\text{S}_2$  diagram at 35 °C was created using Geochemist's Workbench [Bethke, 1998]. While these minerals provide constraints on the redox conditions at which they precipitated,  $f\text{O}_2$  is likely set by reactions involving major elements (*i.e.*, Fe). Hence,  $f\text{O}_2$  set by reactions involving Fe endmembers of brucite ( $\text{Fe}^{2+}(\text{OH})_2$ ) and serpentine were also calculated. Fe endmembers of serpentine used in calculations are  $\text{Fe}^{2+}$ -serpentine (greenalite,  $\text{Fe}^{2+}_3\text{Si}_2\text{O}_5(\text{OH})_4$ ),  $\text{Fe}^{3+}$ -serpentine (hisingirite,  $\text{Fe}^{3+}_2\text{Si}_2\text{O}_5(\text{OH})_4$ ), and mixed-valence serpentine (cronstedtite,  $\text{Fe}^{2+}_2\text{Fe}^{3+}\text{SiFe}^{3+}\text{O}_5(\text{OH})_4$ ). In addition, we calculated  $f\text{O}_2$  set by reactions involving Mg-endmember cronstedtite ( $\text{Mg}_2\text{Fe}^{3+}\text{SiFe}^{3+}\text{O}_5(\text{OH})_4$ ) together with Mg-brucite ( $\text{Mg}(\text{OH})_2$ ), Mg-serpentine (chrysotile,  $\text{Mg}_3\text{Si}_2\text{O}_5(\text{OH})_4$ ), greenalite, and Fe-brucite. We found that calculations using Mg-cronstedtite can better account for the  $\text{Fe}^{3+}/\Sigma\text{Fe}$  determined from the cores (up to 0.9) as it allows total oxidation of all reacting ferrous iron. In contrast, using Fe-cronstedtite only allows up to 50% oxidation of starting ferrous iron. Reaction stoichiometries involving these minerals in calculations of  $f\text{O}_2$  are explicitly provide throughout the discussion.

Early theoretical work on redox conditions attained during serpentinization focused on reactions that involved minor phases (sulfides, oxides, alloys, native metals) and reactions involving  $\text{Fe}^{2+}$ -serpentine/talc [Frost, 1985; Frost and Beard, 2007]. Mineral analysis showed that serpentine can incorporate both ferrous and ferric iron into its crystal structure [Andreani *et al.*, 2013; L. E. Mayhew and Ellison, 2020; D. S. O'Hanley and Dyar, 1993]. Thus, more recent studies often incorporate mixed-valence serpentine (*i.e.*, Fe- and/or Mg-cronstedtite) into thermodynamic models [K A Evans *et al.*, 2013; Klein *et al.*, 2013; Lazar, 2020; J A M Leong and Shock, 2020; B. M. Tutolo *et al.*, 2019; B. M. Tutolo *et al.*, 2020; Zolotov, 2014] (Klein *et al.*, 2013; Zolotov, 2014; Evans *et al.*, 2013; Tutolo *et al.*, 2019; 2020; Lazar, 2020; Leong and Shock, 2020). Oxidation of ferrous iron hosted in  $\text{MgFe}^{2+}$ -brucite and  $\text{MgFe}^{2+}$ -serpentine into ferric iron in cronstedtite ( $\pm$  hisingirite) is dependent on the  $\text{SiO}_2$  activity constrained by these mineral assemblages. In this work, calculations incorporating variable  $\text{SiO}_2$  activities were used, ranging from  $a(\text{SiO}_2)$  dictated by Mg-serpentine (chrysotile) and Mg-brucite to higher  $a(\text{SiO}_2)$  dictated by Mg-serpentine and talc. These, encompass the range of  $a(\text{SiO}_2)$  in pH >9 fluids from the Samail ophiolite [J A M Leong *et al.*, 2021b].

## 2.6 Downhole logging of borehole water Eh, pH, conductivity, temperature and pressure

Borehole water properties were measured via wireline logging using slimline QL40-Ocean, QL40-MUSET and Robertson water quality probes as described in Kelemen *et al.* [Kelemen *et al.*, 2020c].

The oxidation-reduction potential measured by the Ag/AgCl electrode ( $E_{\text{measured}}$ , in volts) was converted to  $E_h$  (relative to the standard hydrogen electrode, in volts) using a temperature-dependent calibration based on data provided by the manufacturer:

$$E_h = E_{\text{measured}} + 0.22323 - 0.001046(T - 298.15) \quad (3)$$

Where  $T$  is the measured temperature in Kelvin. For oxygen reduction the standard reduction potential  $E^0$  (in volts) can be calculated:

$$E^0 = 1.2291 - 0.0008456(T - 298.15) \quad (4)$$

[Bratsch, 1989]. Then oxygen fugacity was calculated by solving the Nernst Equation as a function of  $E_h$ , pH and temperature:

$$\log(fO_2) = \frac{4F}{RT\ln(10)} (E_h - E^0) + 4pH \quad (5)$$

in which  $R$  is the universal gas constant, and  $F$  is Faraday's constant. It should be noted that a single system-wide  $E_h$  value cannot be defined or measured when this method is applied to fluids that contain significant concentrations of multiple, redox sensitive solutes (e.g.,  $O_2$ ,  $H_2$ ,  $Fe^{2+}$ ,  $Fe^{3+}$ ,  $H_2S$ ,  $SO_4^{2-}$ ,  $NO_3^-$ ,  $NH_3$  subject to electron transfer via  $NH_3$  to  $NO_3^-$ ,  $H_2S$  to  $SO_4^{2-}$ ,  $Fe^{2+}$  to  $Fe^{3+}$ ,  $H_2$  to  $H_2O$  or  $H^+$ , and so on), that are not in mutual equilibrium. Different species may record different redox potentials [e.g., Shock *et al.*, 2010], and the reference electrode may not respond to the various dissolved redox-sensitive species equally [Anderson, 2017; Lindberg and Runnells, 1984]. However, among these,  $H_2$  is the most abundant species in serpentinization-generated fluids at depth. For example, Supplementary Figure S4 illustrates that the concentration of dissolved  $H_2$  in borehole water samples from the Samail ophiolite is greater than or equal to the combined concentration of all other redox sensitive solutes. As a result, the measured  $E_h$  and derived  $fO_2$  are likely to correspond well (on a log scale!) to dissolved  $H_2$  concentrations.

We also calculated the oxygen fugacity of water in equilibrium with  $H_2$  at the measured pressure. This represents the stability limit of water, at which no further decrease in oxygen fugacity could occur because  $H_2O$  would form  $H_2$  which would exsolve from solution. This lower limit oxygen fugacity ( $fO_{2(\text{limit})}$  in bars) was calculated as a function of temperature and pressure in the boreholes as:

$$\log(fO_{2(\text{limit})}) = -E^0 \frac{4F}{RT\ln(10)} - 2\log(P) \quad (6)$$

where  $P$  is the measured pressure in bars.

We estimated the uncertainty on  $\log(fO_{2\_in\_bars})$  and  $\log(fO_{2\_limit\_in\_bars})$  based on manufacturer reported uncertainties in the measured  $E_h$  ( $\sigma_{Eh}$ ) of 1 mV, pH ( $\sigma_{pH}$ ) of 0.01, temperature ( $\sigma_T$ ) of 0.005°C, and pressure ( $\sigma_P$ ) of 0.5 bars. Practical uncertainties of field-based measurements were determined by multiplying the manufacturer specifications for uncertainty of the instruments by a factor of 10. The uncertainty on  $\log(fO_2)$ ,  $\log(fO_{2(\text{limit})})$ , and the difference  $\Delta\log(fO_2) = \log(fO_2) - \log(fO_{2(\text{limit})})$  were calculated from the uncertainties on the individual measurements using standard error propagation (Supplementary text, Section 3). While the uncertainties vary slightly as functions of  $E_h$ , pH,  $T$ , and  $P$ , they are consistently less than 1 log unit, and therefore we have used  $\pm 1$  log unit as the estimated upper bound uncertainty for these measurements.

### 3. Results

#### 3.1 Major elements

Figure 6 illustrates downhole variation of major elements in core from Hole BA1B [Kelemen *et al.*, 2021d]. Similar plots for Holes BA3A and BA4A can be found in Kelemen *et al.* [2021f; g]. While the other two Holes do not show systematic variation in bulk composition with depth, Hole BA1B extends 400 meters below the surface, 100 meters deeper than the other two Holes, and this reveals trends that might not be apparent in the others.



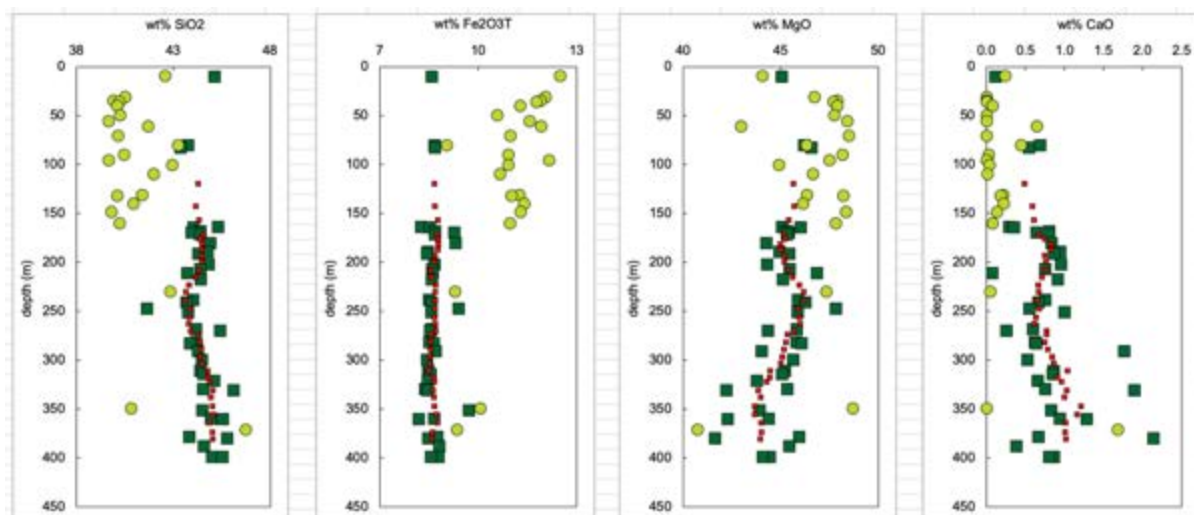


Figure 6: Major element variation in core from Hole BA1B [Kelemen et al., 2021d]. Light green circles: dunite, dark green squares, harzburgite. Small red squares, five point running average of harzburgite compositions.

As expected, there is a sharp break between harzburgite and dunite compositions in all three holes, with dunites having higher total iron (expressed as  $\text{Fe}_2\text{O}_3\text{T}$ ) and  $\text{MgO}$  concentrations, and lower  $\text{SiO}_2$  and  $\text{CaO}$  contents.  $\text{Fe}_2\text{O}_3\text{T}$  contents in dunites are  $\sim 30\%$  higher than in harzburgites ( $\sim 12$  vs  $8$  wt%), whereas  $\text{MgO}$  is only  $\sim 7\%$  richer in dunites compared to harzburgites ( $\sim 47$  vs  $44$  wt%). As a result, molar  $\text{Mg}\#$  (molar  $\text{MgO}/(\text{MgO} + \text{FeO})$ , where all Fe is expressed as FeO) is systematically lower in dunites compared to harzburgites, as illustrated and discussed in Section 4.1.

Calcic pyroxenes (cpx) and orthopyroxenes (opx) in Samail ophiolite mantle peridotites typically contain  $\sim 24$  and  $1$  to  $2$  wt%  $\text{CaO}$  respectively [M Godard et al., 2000; Hanghøj et al., 2010; Monnier et al., 2006]. As a result, normative mineral compositions for these samples, in terms of olivine, cpx, opx and spinel, contain less than  $5\%$  cpx, and would commonly contain no cpx when opx contains several wt%  $\text{CaO}$  at high temperature. However, these samples have been substantially modified by later alteration, as discussed further in Section 4.3, and their high temperature  $\text{CaO}$  contents may have been obscured by this process,

### 3.2 Whole rock alteration

Peridotite core samples from Hole BA1B are pervasively altered, with typical mesh-textured serpentinites near the surface, containing some relict olivine and pyroxene grains at depth. This qualitative observation is quantified in Figures 7 to 16, illustrating systematic decreases in  $\text{CO}_2$ ,  $\text{H}_2\text{O}$  and S contents with increasing depth. These trends are apparent for harzburgites and dunites together, and for harzburgites alone. This is important, because Samail ophiolite dunites are more serpentinitized than other peridotites (e.g., [Kelemen et al., 2021d; e; f; g; h; i]) so that lithological variation alone – with dunites at the top of the hole and harzburgites at greater depth – could give rise to a downhole trend. However, the data from Hole BA1B illustrate a trend that is independent of lithology. These systematic trends are also evident in data on physical properties, from continuous, automated logs of the entire core and shipboard analyses of discrete samples (Figure 7). Downhole variation in the concentration of volatile components is less apparent in core from Hole BA3A and BA4A, as can be seen in plots similar to Figure 8 in Kelemen et al. [2021f; g].

Figure 9 illustrates normative proportions (in weight units) of  $\text{Mg-Fe}^{2+}$ -serpentine,  $\text{Mg-Fe}^{2+}$ -brucite and  $\text{Fe}(\text{OH})_3$  calculated from whole rock compositions, projected from calcite and magnesite. Harzburgites contain more  $\text{SiO}_2$  than dunites, and thus generally have a higher serpentine/brucite ratio.

The normative mineral proportions can then be used to calculate how much  $\text{H}_2\text{O}$  a fully hydrated peridotite of a given bulk composition could contain. These  $\text{H}_2\text{O}$  contents can then be compared to measured bulk rock  $\text{H}_2\text{O}$  concentrations, to quantify the percent hydration of each sample, illustrated in the righthand panel of Figure 8. As expected, dunites are almost fully hydrated, whereas harzburgites record  $\sim 65$  to  $100\%$  hydration. Less predictably, the extent of harzburgite hydration decreases downhole, as does the calculated proportion of brucite in harzburgite (not shown).

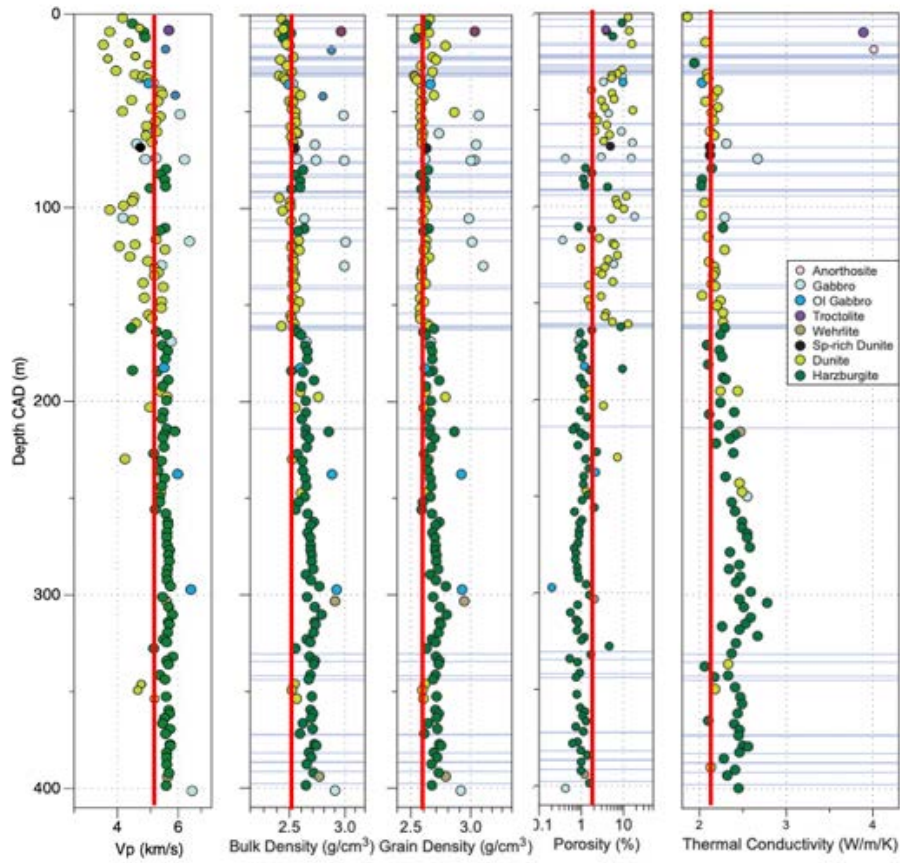


Figure 7: Shipboard measurements of physical properties of discrete samples of core from Hole BA1B [Kelemen et al., 2021d]. Symbols as for Figure 6, with symbols for additional lithologies given in the legend.

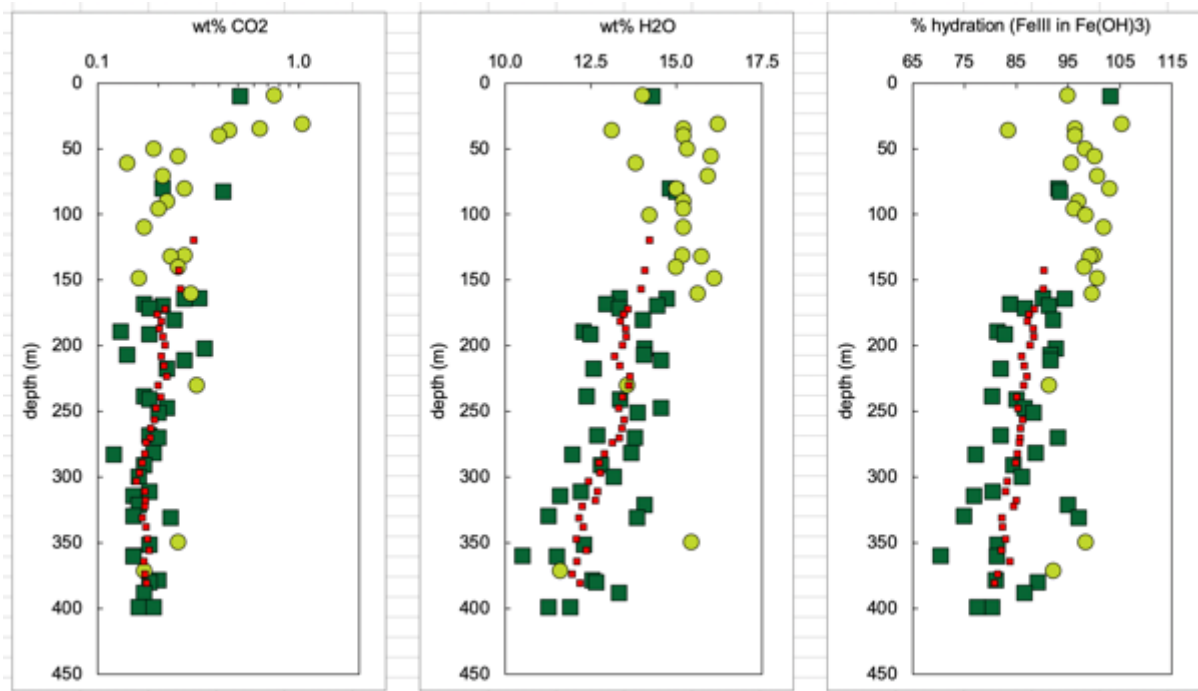


Figure 8: Volatile contents of core from Hole BA1B [Kelemen et al., 2021d]. Righthand panel illustrates the “percent of maximum hydration”, based on observed H<sub>2</sub>O contents divided by water content of a completely hydrated rock, determined from normative proportions of calcite, magnesite, lizardite, brucite and ferrihydrite calculated from the major element and CO<sub>2</sub> contents of each sample. Only three harzburgites contain “negative brucite”. If fully hydrated, these three samples would contain some talc, rather than brucite). We also calculated mineral norms with all Fe<sup>3+</sup> in Mg-Fe<sup>2+</sup>-cronstedtite rather than Fe(OH)<sub>3</sub>. This yields higher normative proportions of brucite in all samples. Symbols as in Figure 6.



Figure 9: Normative proportions of lizardite, brucite and ferrihydrite, projected from calcite and magnesite, in core from Hole BA1B, calculated from the major elements and CO<sub>2</sub> contents of each sample. Symbols as in Figure 6.

Full resolution versions of all figures in this paper are provided in a separate file.

Full thin section images of core samples from Hole BA1B reveal a pattern of color variation, with red, “rusty” sections predominant at the top, a zone of “black serpentinites” at ~ 50 to 150 meters depth, and green, partially serpentinitized peridotites in cores from the deeper part of the hole. Figure 10 provides end-member examples of these three color zones. The red and green color variations are present, but less marked, in core from Holes BA3A and BA4A; the black zone was only prominent in core from Holes BA1B and BA4A. We used image analysis of thin sections to quantify these variations for all of the shipboard thin sections from Hole BA1B. High “redness and low “greenness” characterize the rusty colored sections, low luminance characterizes the black serpentinite sections, and high greenness-redness defines the green sections.

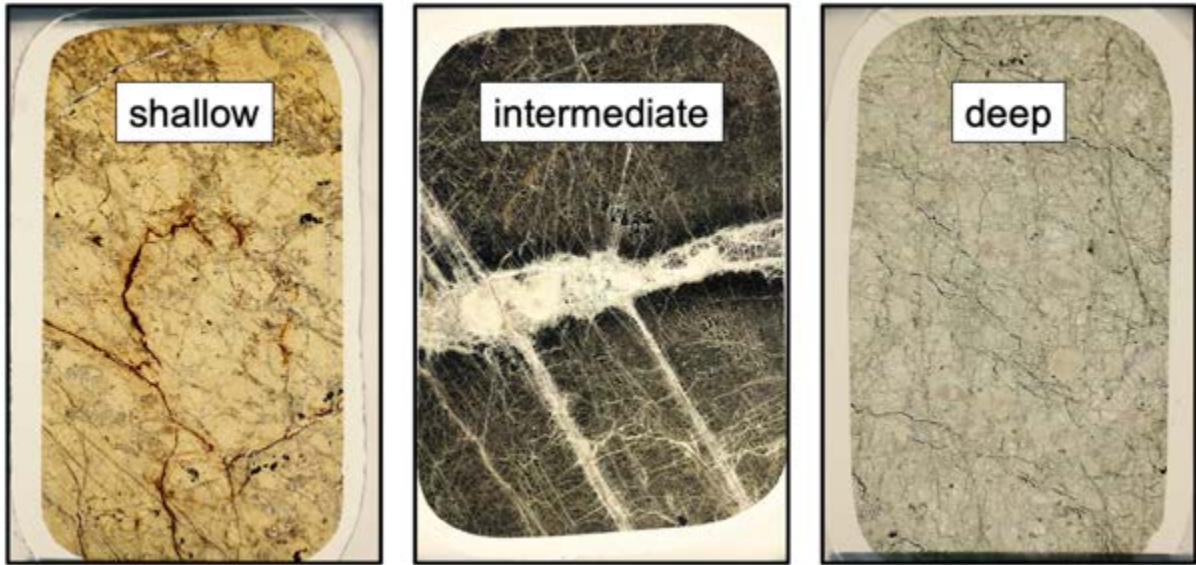


Figure 10: Representative plane polarized photomicrographs of thin sections of core from Hole BA1B. Left BA1B\_4\_2\_43\_48, 10 m depth, center BA1B\_44\_2\_73\_78, 109 m depth, right BA1B\_114\_4\_51\_56, 321 m depth.

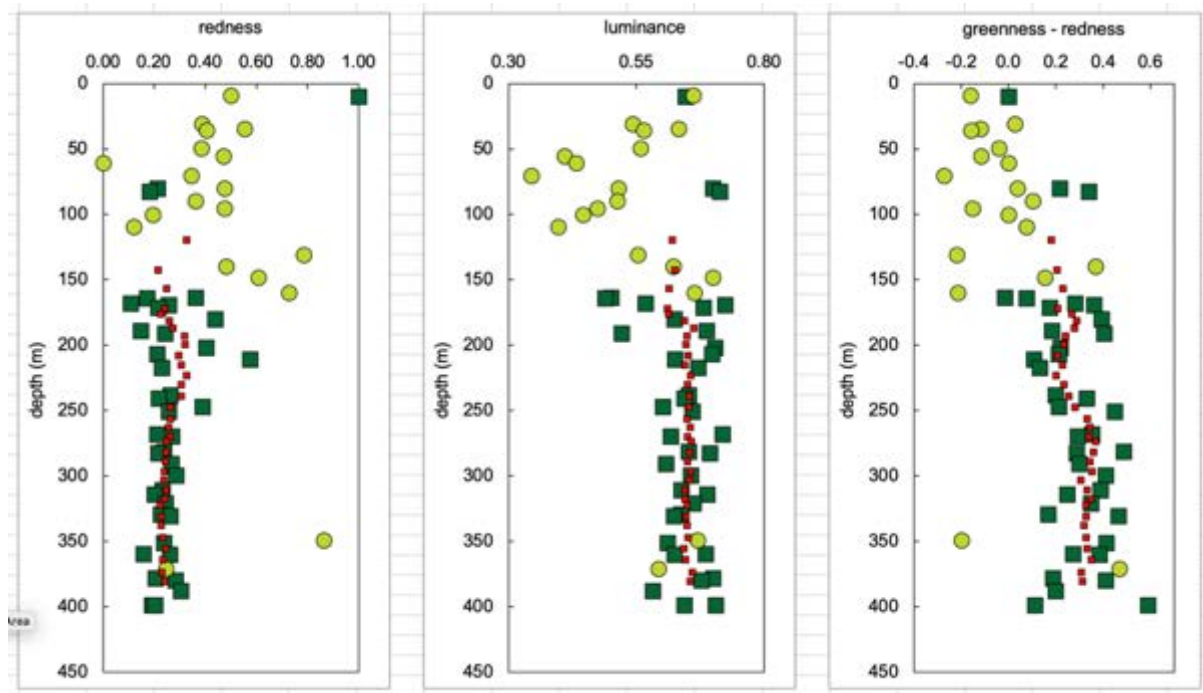


Figure 11: Color data from plane polarized optical measurements of thin sections of core from Hole BA1B. See Section 2.1 for analytical methods. Symbols as in Figure 6.

Intuitively, it is obvious that the red, rusty cores contain a higher proportion of ferric to ferrous iron, and indeed this is borne out by our quantitative data (compare Figures 11 and 12). What is less evident is that the black serpentinites – which, based on our extensive, ongoing electron microprobe investigations (e.g., Figure 14), lack significant proportions of opaque, iron oxide minerals – have relatively high sulfur concentrations, as documented in Figures 12 and 13. Similar sulfide enrichments are also present in black serpentinites in core from Hole BA4A [Kelemen *et al.*, 2021d], which contain up to 0.4 wt% S (Supplementary Figure S5), though the color zoning in BA4A core is more patchy rather than restricted to a limited depth interval. In contrast, sulfur was below detection limit in all analyzed samples from Hole BA3A [Kelemen *et al.*, 2021f].



Figure 14 provides X-Ray maps of both S and Ni contents of one black serpentinite sample; sulfur abundances are generally low, but it is clear that sulfur (and Ni) are present in one or more microscopic to sub-microscopic phases, within and rimming serpentinite mesh cores. While we are not sure of the nature of these phases, we hypothesize that they include tochilinite, valleriite and/or haapalite, mixed sulfide-hydroxide  $\pm$  carbonate minerals and amorphous materials reported in core from the MBO [Kelemen et al., 2021g; A Templeton et al., 2021; B. M. Tutolo and Evans, 2018] and in weathered serpentines from other localities [Alt and Shanks III, 2003; J. S. Beard, 2000; J. S. Beard and Hopkinson, 2000; Hopkinson et al., 2000; Schwarzenbach et al., 2012]. In some cases, these phases may be intergrown with serpentinite at the nano-scale (Leong, pers. comm. 2021).

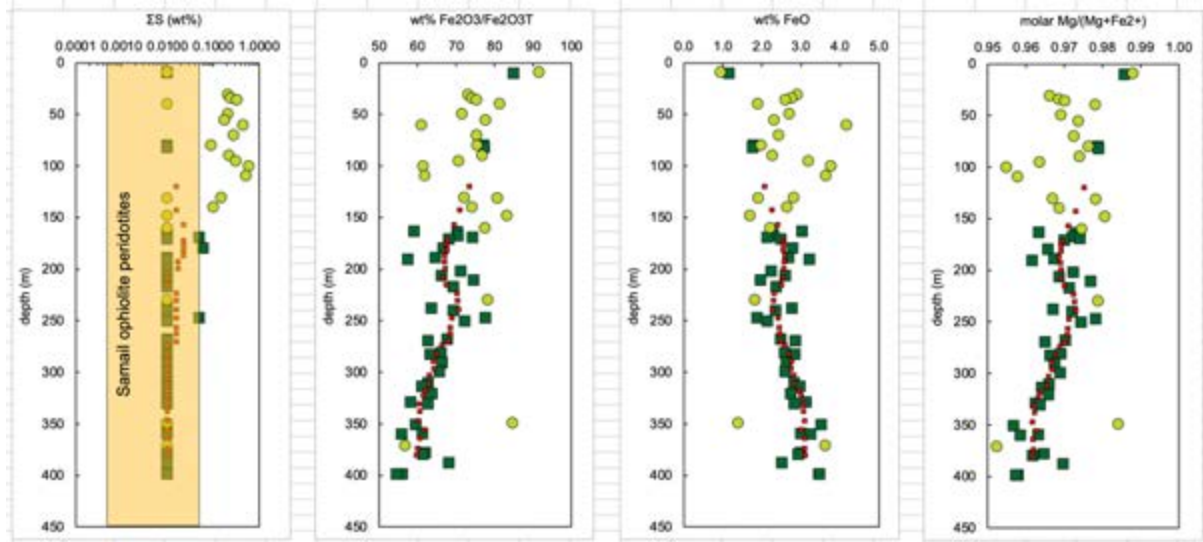


Figure 12: Sulfur concentration [Kelemen et al., 2021d], and ferric iron/total iron ratio, measured FeO concentration and molar  $Mg/(Mg+Fe^{2+})$  ratio in core from Hole BA1B (Supplementary Table S1). Sulfur concentrations below the detection limit of shipboard analyses were assigned a value of 0.01 wt% (100 ppm). Orange bar in lefthand panel illustrates previously measured range of sulfur concentration in mantle harzburgites and dunites in the Samail ophiolite, from 5 to 500 ppm [Hanghøj et al., 2010; Oeser et al., 2012]. Symbols as in Figure 6.

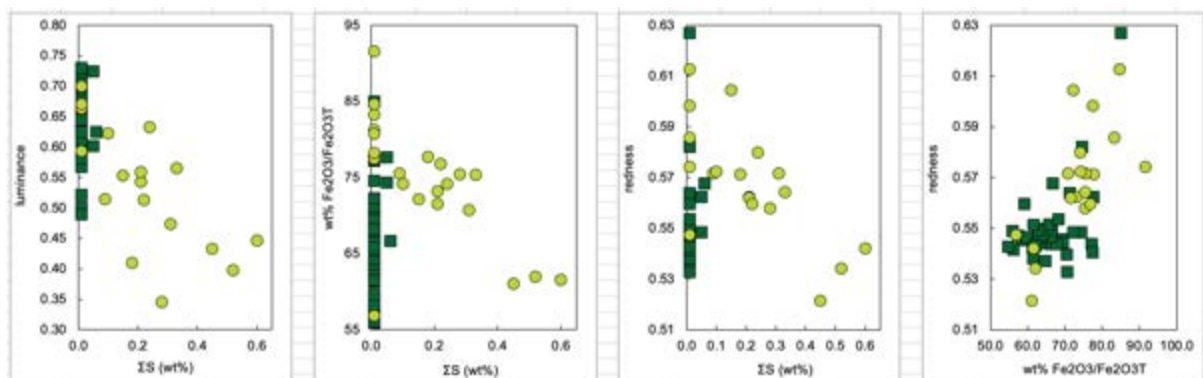


Figure 13: Relationship of sulfur content with optical properties of thin sections (Figure 11) and ferric iron/total iron ratios. As discussed in the text, these relationships indicate that sulfur concentrations are highest in the “black serpentinite zone” extending from  $\sim$  30 to 150 m depth, characterized by low  $Fe^{3+}/Fe_T$ , and relatively low in the oxidized, red zone at depths less than 30 m. Symbols as in Figure 6.

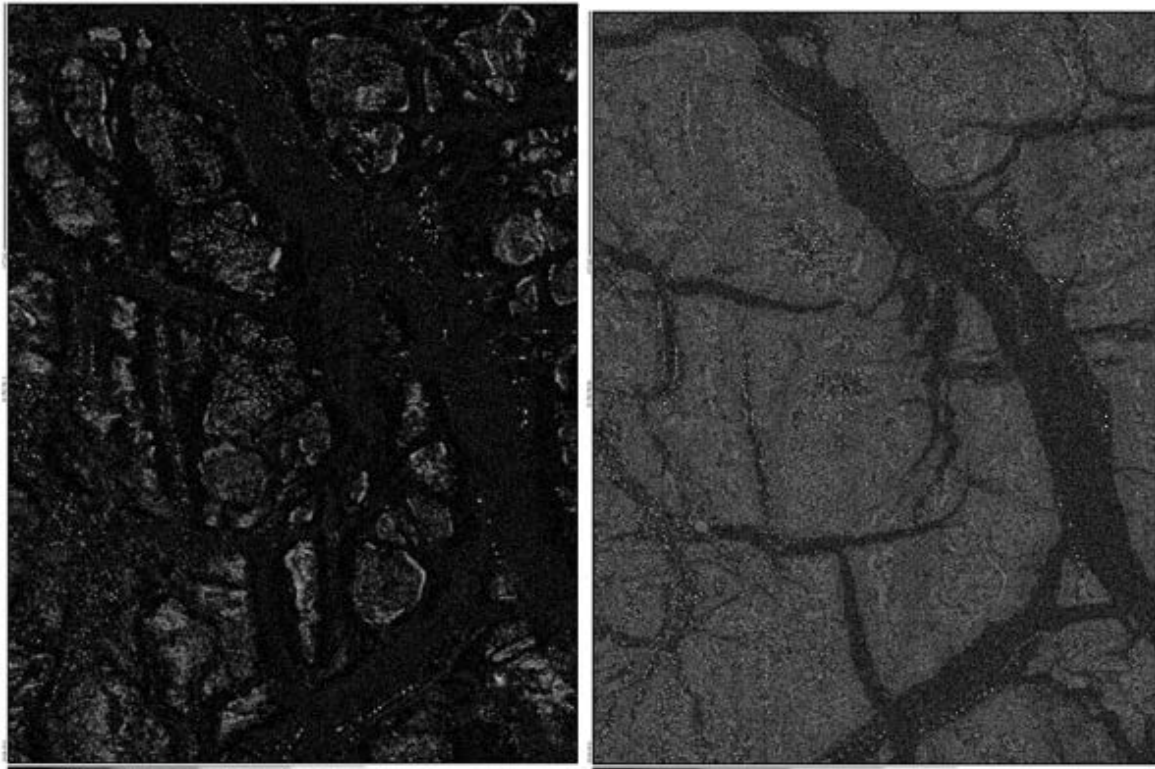


Figure 14: Electron microprobe, X-ray intensity maps for sulfur (left) and nickel (right) in core from Hole BA4A, sample BA4A\_82-2 43-45cm, 200 m depth. Field of view, 300 microns tall.

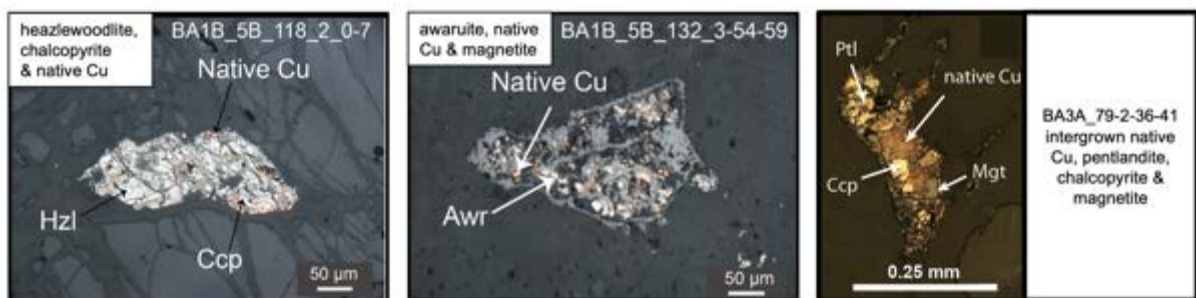


Figure 15: Observed intergrowths of sulfides, oxides and metals in core. Left: BA1B\_118-2\_0-7, 330 m depth, center BA1B\_132-3\_54-59, 371 m depth, and BA3A\_79-2-36-41, 199 m depth. Cross polarized reflected light images excerpted from Eslami et al. [Eslami et al., 2018] and Figure F32 in Kelemen et al. [Kelemen et al., 2021f]. Abbreviations used in this figure: Hzl: heazlewoodite; Ccp: chalcopyrite; Awr: Awaruite; Mgt: magnetite; Ptl: Pentlandite.

The matrix alteration of peridotites in core from the MBO formed oxide, sulfide and metal phases that were identified in thin section via reflected light microscopy onboard DV Chikyu [Kelemen et al., 2021d; f, g], and later verified by electron microprobe analyses [Eslami et al., 2018]. Figure 15 illustrates examples of intergrown heazlewoodite, chalcopyrite, native copper, awaruite, pentlandite and magnetite. These can be used to constrain oxygen fugacity during pervasive matrix alteration, as discussed below and in Sections 4.4 to 4.6.

Figure 16 illustrates the stability of these minerals at 35°C as a function of oxygen and sulfur fugacity. Aside from the absence of bornite in our samples, and assuming that intergrown minerals formed in equilibrium with each other, assemblages juxtaposing (a) chalcopyrite, heazlewoodite and native copper, and (b) chalcopyrite, pentlandite, magnetite and native copper are indicative of  $fO_2$  close to the low  $fO_2$  limit where  $H_2O$  is reduced to form  $H_2$ .

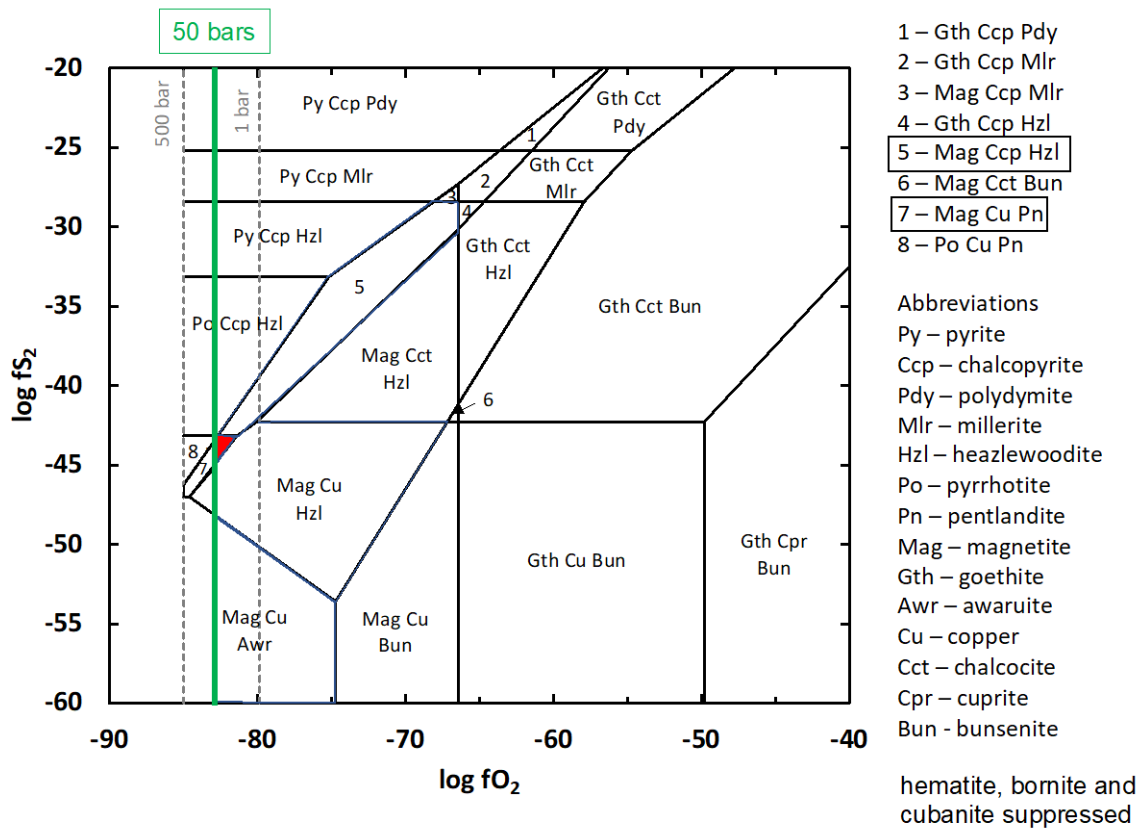


Figure 16: Phase diagram in terms of log  $O_2$  fugacity versus log  $S_2$  fugacity, for Fe, Ni and Cu sulfides, oxides and metals at 35°C and 500 bars  $H_2O$ , with isopleths for the limit where  $H_2O$  is reduced to form  $H_2$  at 1 bar, 50 bars (green) and 500 bars. The positions of other phase fields are not strongly pressure dependent in the range of  $P(H_2O)$  from 1 to 500 bars. Green fields contain assemblages with native copper and magnetite, ± heazlewoodite (light green) and awaruite (darker green). Red field contains assemblages with magnetite, native copper and pentlandite. Blue field contains magnetite, chalcopyrite and heazlewoodite. Magnetite, copper and awaruite (Figure 15 center) can coexist along the isothermal, isobaric univariant line between the two green fields. Copper, heazlewoodite and chalcopyrite (Figure 15, left) are stable together along the univariant line between the blue and light green fields, at  $f_{O_2}$  from  $10^{-30}$  to  $10^{-32}$  bars. Only a small corner of field 7, for pentlandite-bearing assemblages, is stable at  $f_{O_2}$  above the  $H_2O$ - $H_2$  limit at less than 50 bars total pressure. Pentlandite, magnetite, copper and chalcopyrite (Figure 15, right) can stably coexist along the univariant line between red and blue, restricting  $f_{O_2}$  to less than  $\sim 10^{-62}$  bars. Abbreviations for minerals: Py – pyrite, Ccp – chalcopyrite, Pdy – polydymite, Mlr – millerite, Hzl – heazlewoodite, Po – pyrrhotite, Pn – pentlandite, Mag – magnetite, Gth – goethite, Awr – awaruite, Cu – copper, Cct – chalcocite, Cpr – cuprite, Bun – bunsenite.

### 3.3 Vein types and proportions

The Proceedings of the Oman Drilling Project include extensive information about the different types of veins cutting the mesh-textured serpentinites in the MBO, and their cross-cutting relationships. [Kelemen et al., 2021d; f; g]. It is beyond the scope of this paper to review all that material. However, we can make some important overall points.

**First**, systematically counting and measuring veins in mesh-textured serpentinite is difficult, because the mesh itself is defined by a grid of  $\sim 5$  to 50 micron wide veins,  $\sim 50$  to 200 microns apart, with “mesh cores” between them. The shipboard science teams tried not to include the frequency or volume of mesh veins in their logging, but this may have led to systematic errors that differed from observer to observer, and from day to day, particularly as the team became more familiar with subtle features of the core. Figure 17 provides an example of a black magnetite-serpentine vein cutting across the mesh texture. Depending on the level of scrutiny, the nature of the cut core face, and other factors, veins like this one could have been logged, or missed.



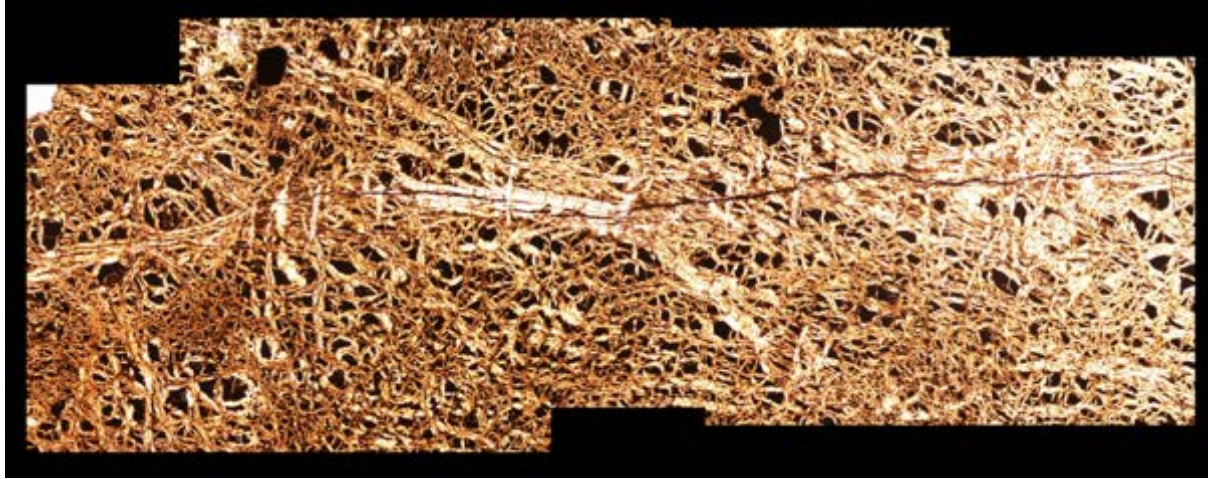


Figure 17: Composite, plane polarized, transmitted light image of a long, black, magnetite-serpentine vein extending horizontally across the image, cutting earlier mesh texture in serpentinized peridotite. Sample BA1B 26-3\_42–45, 57 m depth. Image from Figure F27 in Kelemen et al. [Kelemen et al., 2021d]. Width of image, approximately 4.1 millimeters. During visual core description, mesh veins were not logged, but it was often difficult to distinguish between mesh veins and early serpentine-magnetite veins like the one shown here.

**Second**, as noted in Section 1.4, the veins could record a variety of different events and conditions, potentially ranging from early hydrothermal alteration near an oceanic spreading center, extending into the shallow mantle, through Cretaceous subaerial weathering and by a Late Cretaceous marine transgression, to present day weathering. While cross-cutting relationships provide an indication of relative age, they do not provide absolute age information.

**Third**, the two youngest vein types, based on consistent cross-cutting relationships, were “waxy veins” and carbonate veins. The first group has an aphanitic, glossy appearance on the cut core face. In thin section, these veins have isotropic to microcrystalline serpentine cores, often flanked by fibrous microcrystalline rims with elongate crystals perpendicular to vein contacts. At the thin section scale, the vein contacts are sharp, but curved and irregular rather than planar. Initially this vein type was named “waxy green veins”, but toward the bottom of Hole BA1B, and deep in the other two cored holes, the same textures were seen in white veins, so the color adjective was dropped.

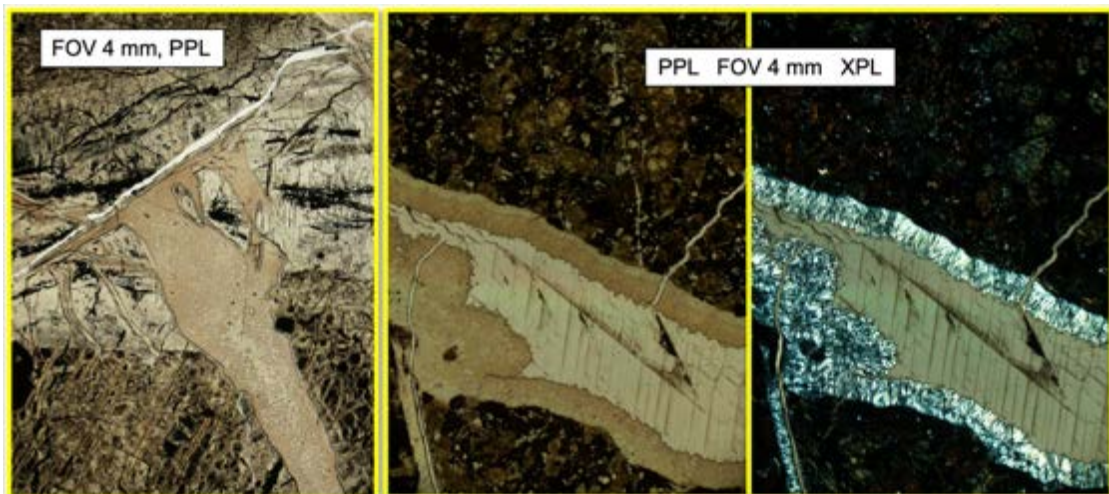


Figure 18: Transmitted light photomicrographs of waxy serpentine veins. Left, plane polarized light image, white carbonate vein cuts (?) brownish waxy serpentine vein, which in turn cuts serpentinite mesh texture and a set of grey, intermediate-aged, coarse serpentine veins, BA1B\_23-4\_37-41. Center (plane-polarized) and right (cross-polarized light) images of vein containing intergrown carbonate and waxy serpentine, cutting mesh textured serpentinite. Serpentine is brown in plane light, with bright-grey interference colors in cross-polarized light; coarse single crystal of carbonate is tan in both images, and contains twin planes that diagonally intersect grain boundaries. BA1B\_17-1\_22-22.5. Righthand pair of photos kindly provided by Wolf-Achim Kahl.



The carbonate veins were typically logged as calcite veins, particularly early in the description of core from Hole BA1B, and in almost every instance when the vein material effervesced in dilute HCl. However, XRD analyses performed at Lamont Doherty Earth Observatory demonstrate that most of these veins contain dolomite, aragonite, magnesite, and huntite (a hydrous Mg-carbonate), instead of, or in addition to, calcite (Supplementary Table S3).  $^{14}\text{C}$ ,  $^{87}\text{Sr}/^{86}\text{Sr}$  and stable carbon and oxygen isotope data on a subset of the carbonate veins are presented in Section 3.4.

Carbonate veins and waxy veins are commonly intergrown, as shown in Figure 18, indicating approximately coeval formation, at least in some instances. Waxy veins, particularly in the deeper parts of BA1B and throughout BA4A, commonly cut contacts between gabbroic veins and surrounding serpentinites.



*Figure 19: Typical textures of waxy serpentine veins in photographs of cut core face [Kelemen et al., 2021g], with field of view about 8 cm tall. Left: BA4A-88Z-3\_8-18, 238 meters depth, “turtle-textured” grid of intersecting veins, right: BA4A-88Z-4\_4-24, 240 m depth, veins cutting altered gabbro dikes, extending a few cm into serpentine surrounding the dike margins.*

Serpentine in waxy veins from one sample of BA1B core contains relatively low  $\text{SiO}_2$  contents, and several weight percent  $\text{Al}_2\text{O}_3$ , indicative of substitution towards the amesite mineral end member (Figure 20, data in Supplementary Table S2). Similarly, elsewhere in the Samail ophiolite and

probably in BA1B core, serpentines have relatively low SiO<sub>2</sub> and high Fe, interpreted to be due to appreciable amounts of the cronstedtite substitution ((Mg,Fe<sup>2+</sup>)<sub>2</sub>Fe<sup>3+</sup>SiFe<sup>3+</sup>O<sub>5</sub>(OH)<sub>4</sub>). On the other hand, analyses of waxy serpentine veins in a sample of core from Hole BA3A have very low Al and Fe<sup>3+</sup> contents, and approximately 2 Si per formula unit. It's likely that continued analyses of the cores will reveal gradients in serpentine contents with depth in BA1B, and generally lower Fe<sup>3+</sup> in BA3A serpentines.

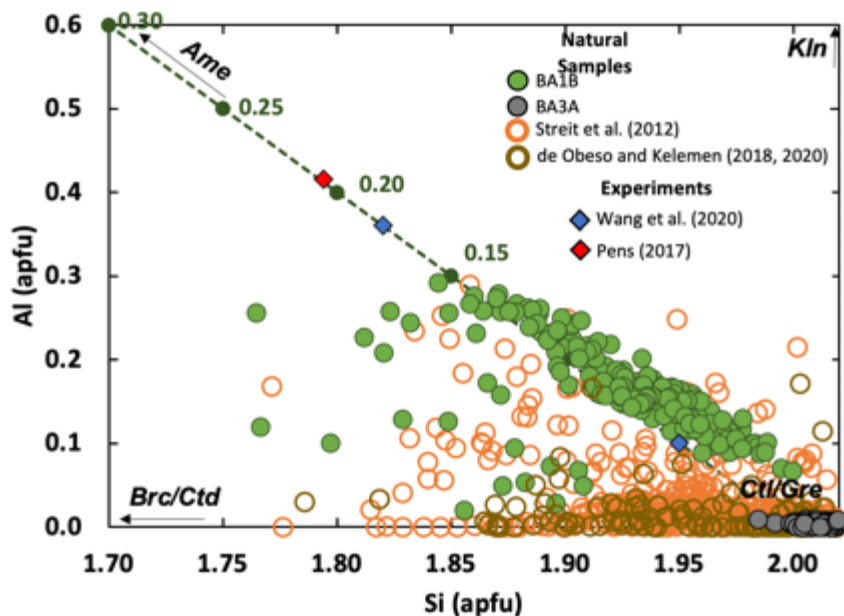


Figure 20: Silicon and aluminum contents of waxy serpentine veins in core from BA1B 17-1 22-25.5, 33 meters depth (filled green circles), cutting an altered gabbroic dike and extending into mesh-textured serpentinite, and BA3A 43-3 24-27, 100 m depth (filled grey circles) cutting mesh-textured serpentinite without gabbroic dikes. These data are, compared to analyses of low temperature serpentine veins formed by young weathering (< 50,000 years, open orange circles, Streit et al. [2012]) and by weathering from just below an unconformity overlain by Late Cretaceous limestones (open brown circles, de Obeso and Kelemen [2018; 2020]). Filled diamonds are compositions of serpentine produced in experiments saturated in Al<sub>2</sub>O<sub>3</sub>; blue: Wang et al. [Wang et al., 2020]; red: Pens [Pens et al., 2016]. All concentrations determined by electron microprobe as described in Section 2.3. Calculated Si and Al apfu values are based on 7 oxygen atoms. Dark green dashed line indicates mixtures of chrysotile/greenalite and amesite. Filled dark green circles are labeled with mole % amesite in these mixtures. Abbreviations for minerals: Ctl – chrysotile (Mg<sub>3</sub>Si<sub>2</sub>O<sub>5</sub>(OH)<sub>4</sub>), Gre – greenalite (Fe<sup>2+</sup><sub>3</sub>Si<sub>2</sub>O<sub>5</sub>(OH)<sub>4</sub>), Kln – kaolinite (Al<sub>2</sub>Si<sub>2</sub>O<sub>5</sub>(OH)<sub>4</sub>), Ctd – Mg-Fe<sup>2+</sup>-cronstedtite ((Mg-Fe<sup>2+</sup>)<sub>2</sub>Fe<sup>3+</sup>SiFe<sup>3+</sup>O<sub>5</sub>(OH)<sub>4</sub>), Brc – Mg-Fe<sup>2+</sup>-brucite ((Mg-Fe<sup>2+</sup>)(OH)<sub>2</sub>), Ame – Mg-Fe<sup>2+</sup>-amesite ((Mg-Fe<sup>2+</sup>)<sub>2</sub>AlSiAlO<sub>5</sub>(OH)<sub>4</sub>).

Together with relatively Al-rich serpentine, some waxy veins contain andradite-hydrogrossular garnet solid solutions, and microcrystalline chlorite (Figure 21, data in Supplementary Table S2). Combined with the common spatial association of waxy veins with gabbroic dikes, these observations suggest a role for Al in stabilizing serpentine minerals that grow at a geologically appreciable rate in the low temperature weathering environment (rates discussed in Section 4.7).

**Fourth**, the abundance of carbonate veins declines steeply from a few volume percent in the upper tens of meters (poorly sampled during drilling) to near zero in cores from more than 100 m below the surface (Figure 22). The frequency of waxy veins also shows a general decrease with depth in core from Hole BA1B, though no trend is evident in the other two cores. Older sets of black, white and composite serpentine veins do not show systematic variation in frequency with depth. Overall, all cored MBO Holes show decreasing area proportion of veins with increasing depth (Figure 23).

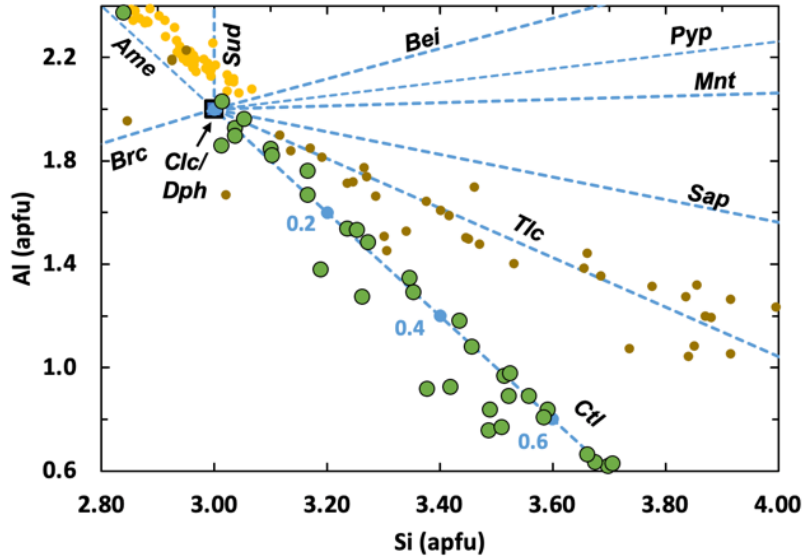


Figure 21: Silicon and aluminum contents of microcrystalline chlorite in waxy serpentine veins cutting an altered gabbroic dike and surrounding, mesh-textured serpentinite (filled green circles, BA1B 17-1 22-25.5, 33 meters depth) compared to chlorite in altered gabbros near OmanDP Site GT1 (orange circles, Zihlmann et al. [2018]) and in altered oceanic crust (brown circles, Alt and Bach [2001]). Calculated Si and Al apfu values are based on 14 oxygen atoms. Endmember minerals are indicated by the blue squares and dashed blue lines. Analyses indicate that the natural chlorites are mixtures including clinocllore (Clc,  $Mg_5AlSi_3AlO_{10}(OH)_8$ ), daphnite (Dph,  $Fe_5AlSi_3AlO_{10}(OH)_8$ , aka chamosite), sudoite (Sud,  $(Mg-Fe^{2+})_2Al_3Si_3AlO_{10}(OH)_8$ ), Mg-Fe<sup>2+</sup>-chrysotile (Ctl,  $(Mg-Fe^{2+})_6Si_4O_{10}(OH)_8$ ), Mg-Fe<sup>2+</sup>-amesite (Ame,  $(Mg-Fe^{2+})_4Al_2Si_2Al_2O_{10}(OH)_8$ ), Mg-Fe<sup>2+</sup>-talc (Tlc,  $(Mg-Fe^{2+})_3Si_4O_{10}(OH)_2$ ), pyrophyllite (Pyp,  $Al_2Si_4O_{10}(OH)_2$ ), beidellite (Bei,  $K_{0.33}Al_2Si_{3.67}Al_{0.33}O_{10}(OH)_2$ ), montmorillonite (Mnt,  $Ca_{0.17}(Mg,Fe^{2+})_{0.33}Al_{1.67}Si_4O_{10}(OH)_2$ ), and/or saponite (Sap,  $Ca_{0.17}(Mg,Fe^{2+})_3Si_{3.67}Al_{0.33}O_{10}(OH)_2$ ). Clinocllore, daphnite, and sudoite endmembers belong to the chlorite group of minerals. Chrysotile and amesite endmembers belong to the serpentine group while beidellite, montmorillonite, and saponite endmembers are clay minerals. The chrysotile and amesite endmembers used in this figure are two times the formula units used in Figure 20 to be consistent with chlorite stoichiometry (2x serpentine).

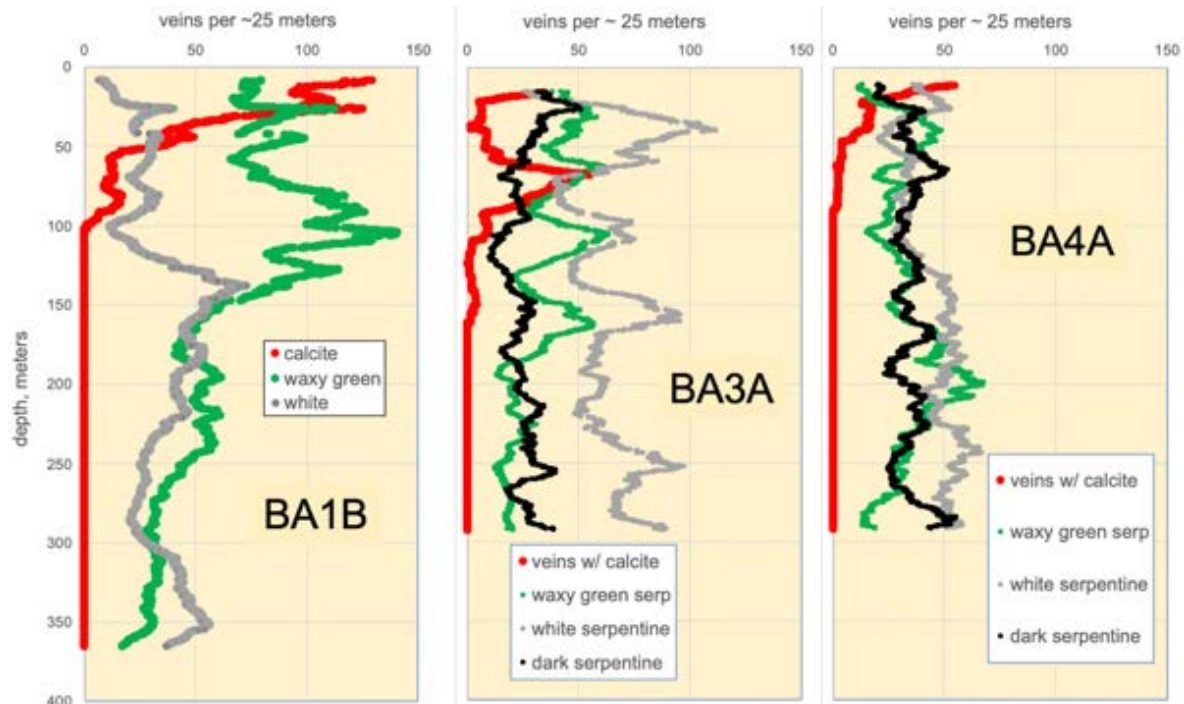


Figure 22: 25 meter running average vein frequency from shipboard visual core description, Left: Figure F30 from Kelemen et al. [Kelemen et al., 2021d]. Center: Figure F28 from Kelemen et al. [Kelemen et al., 2021f]. Right: Original plot from data in Kelemen et al. [Kelemen et al., 2021g].



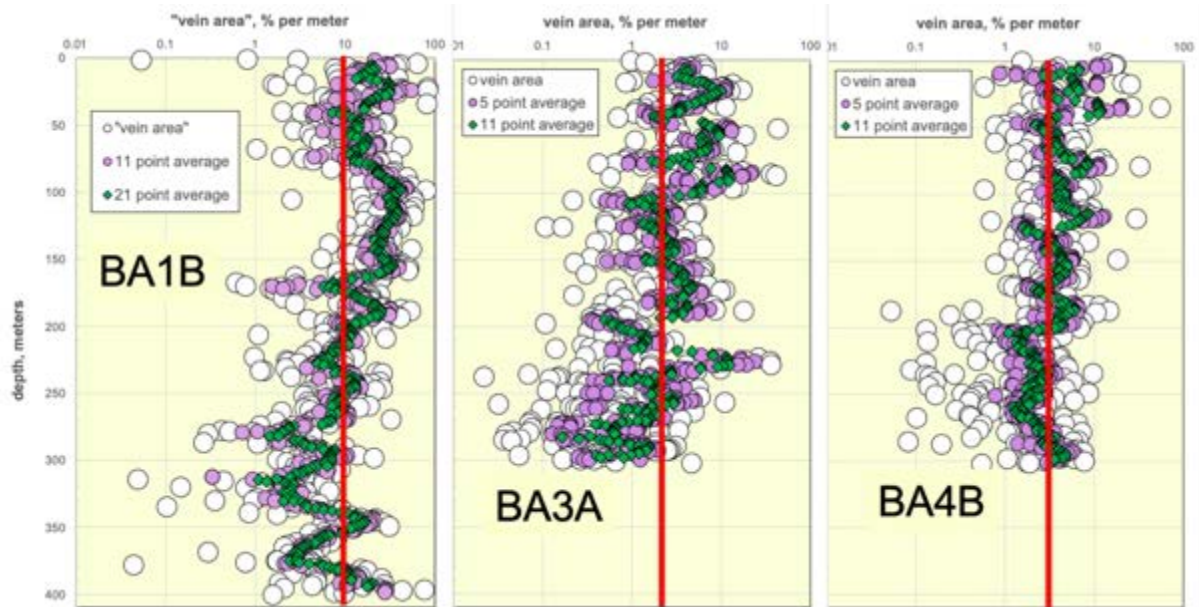


Figure 23: Core section and running average data on vein area, in units of percent volume fraction of the core, calculated from vein widths and frequency data from shipboard visual core description logs. Left: Figure F28 from Kelemen et al. [Kelemen et al., 2021d]. Center: Figure F27 from Kelemen et al. [Kelemen et al., 2021f]. Right: Original plot from data in Kelemen et al. [Kelemen et al., 2021g].

**Fifth**, though vein volumes were not well constrained during core description onboard DV Chikyu, a combination of data on vein frequency and width allowed the shipboard science team to approximately quantify the overall volume fraction of veins in the core as a function of depth.

### 3.4 Isotopic characteristics of carbonate veins

Supplementary Table S3 reports new data on  $^{14}\text{C}$ ,  $^{87}\text{Sr}/^{86}\text{Sr}$ ,  $\text{d}^{13}\text{C}$  and  $\text{d}^{18}\text{O}$ , collected for this paper.

$^{14}\text{C}$  contents are reported as fraction modern carbon, and as the  $^{14}\text{C}$  “age” of samples. The “age” assumes that they formed at a single time from a source equilibrated with atmospheric  $\text{CO}_2$  at that time. About 2/3 of analyzed samples contained measurable  $^{14}\text{C}$  (7 of 15 from 3 to 57 m in BA1B, 6 of 6 from 5 to 9 m in BA3A, 10 of 14 from 1 to 32 m in BA4A). The chances of sample contamination are low – samples were acid washed to remove young carbon introduced during drilling and sample preparation, and in any case it is difficult to contaminate carbonate samples with carbon. Fraction modern  $^{14}\text{C}$  abundances range from zero to  $0.0782 \pm 0.00001$ , corresponding to nominal ages ranging from greater than ~ 50,000 years to  $20,300 \pm 100$  years. The sample with the lowest measurable  $^{14}\text{C}$  abundance contains  $0.16 \pm 0.05$  % modern carbon, corresponding to a nominal age of  $52,600 \pm 2300$  years. Thus, about 2/3 of the carbonate veins appear to have formed, or incorporated a young carbon component, in the last 53,000 years.  $^{14}\text{C}$  abundance does not have any discernable variation with depth.

$\text{d}^{13}\text{C}$  and  $\text{d}^{18}\text{O}$  ranges (-5.7 to -16.0 ‰ relative to VPDB, 23.5 to 34.3 ‰ relative to SMOW, respectively) are similar to those reported for peridotite-hosted carbonate veins sampled from outcrops and road cuts in Samail ophiolite peridotites, with values that are generally higher than in young travertines deposited at peridotite-hosted alkaline springs. (Kelemen and Matter 2008; Kelemen et al. 2011; Mervine et al. 2014; Falk et al. 2016; de Obeso and Kelemen 2018). If we apply published oxygen isotope exchange thermometers for dolomite [O’Neil et al., 1969; Vasconcelos et al., 2005] together with the observation that present-day Oman well and spring water has  $\text{d}^{18}\text{O}$  within two per mil of seawater ( $\text{d}^{18}\text{O}$  SMOW = 0), we obtain temperatures of ~ 10 to 45°C. Using  $\text{d}^{18}\text{O}$  exchange thermometers for calcite [Chacko and Deines, 2008; O’Neil et al., 1969], applied to  $\text{d}^{18}\text{O}$  data for aragonite, yields temperatures of ~ 22 to 50°C. These low temperatures, together with a mean annual surface temperature of 30°C in northern Oman, and an approximate geothermal gradient of 20 to 25°C estimated from temperature profiles measured in MBO boreholes, are

consistent with the  $^{14}\text{C}$  ages, and both data sets are indicative of vein formation via water-rock reaction near the present-day erosional surface.

Present day  $^{87}\text{Sr}/^{86}\text{Sr}$  ratios in eleven carbonate vein samples range from  $0.708216 \pm 0.000016$  to  $0.708596 \pm 0.000015$ , averaging  $0.708492 \pm 0.000066$  (2 std error). These values are similar to  $^{87}\text{Sr}/^{86}\text{Sr}$  previously reported for peridotite-hosted spring and well water, and for young, low temperature carbonate veins, in the Samail ophiolite mantle section [Kelemen *et al.*, 2011; Weyhenmeyer, 2000]. They are higher than  $^{87}\text{Sr}/^{86}\text{Sr}$  in seawater from 20 Ma to 96 Ma [McArthur *et al.*, 2020], where 96 Ma is the age of Samail ophiolite crustal formation and hydrothermal alteration near an oceanic spreading center [Rioux *et al.*, 2012; Rioux *et al.*, 2013; Tilton *et al.*, 1981; Warren *et al.*, 2005]. However, the Sr isotope ratios in our carbonate vein samples are lower than present-day seawater and rainwater, most likely due to mixing between a young seawater component and small amounts of mantle-derived Sr with  $^{87}\text{Sr}/^{86}\text{Sr} \sim 0.703$ .

### 3.5 Borehole water properties

Borehole water properties were measured as described in Kelemen *et al.* [Kelemen *et al.*, 2020c]. We used the measured temperature, pressure, Eh and pH to calculate oxygen fugacity,  $f\text{O}_2$ , as described in Section 2.6. Downhole variation of water  $f\text{O}_2$  and pH is illustrated in Figure 24. Where repeated measurements were made in the same borehole, these are illustrated in separate panels.

In general, pH in borehole waters increases with depth, while  $f\text{O}_2$  decreases with depth. Lubrication for drilling utilized fresh drinking water, thought to be close to equilibrium with air at 1 bar. Thus, drilling introduced oxidized water into the more reduced, peridotite-hosted aquifer(s). Partly for this reason, borehole waters have generally become more alkaline and more reduced over time since drilling. Unfortunately, it is not clear whether this results from (1) advective or diffusive mixing of freshwater introduced during drilling with reduced, alkaline pore water in the surrounding rocks, (2) flow of freshwater away from the Holes, to be replaced by reduced, alkaline pore water from the surrounding rocks, or (3) reaction between the freshwater introduced by drilling and the surrounding rocks.

Holes BA1A and BA1D are about 15 meters from each other. They are hydraulically connected at depth, via a fracture network with a permeability  $\sim 10^{-15} \text{ m}^2$  [Lods *et al.*, 2020]. Hole BA1B is  $\sim 105$  meters from BA1D and 120 meters from BA1A. Water with intermediate pH near the top of BA1A flows rapidly downward from 25 to 60 meters depth, below which flow rates are too low to measure. Below 150 and 50 meters in BA1A and BA1D, respectively, one year after drilling water the lower half of both Holes had become more alkaline and reduced, with oxygen fugacity approaching the  $\text{H}_2\text{O}-\text{H}_2$  limit.

Unfortunately, water properties in BA1B have only been fully logged once, a month after drilling, though downhole pH was measured approximately two years later. A second pH log revealed lower pH in the upper 200 m of the Hole, and higher pH in the lower half of the Hole [Figure 2 in A Templeton *et al.*, 2021]. The early measurements of Eh, pH, temperature and pressure yielded a calculated  $f\text{O}_2$  with a relatively smooth gradient, gradually declining with increasing depth. As for BA1B, BA3A and BA4A were also logged just once, within a few months of drilling. In BA3A, a pH log two years after drilling revealed a small increase in pH throughout the hole, to  $\sim 11$ , suggestive of buffering involving  $\text{Ca}^{2+}$  and  $\text{OH}^-$  [Barnes and O'Neil, 1969; Bruni *et al.*, 2002; J A M Leong *et al.*, 2021b; J A M Leong and Shock, 2020; Neal and Stanger, 1984; Paukert *et al.*, 2012]. BA3A is 5 meters from water monitoring well NSHQ14, drilled in 2004. Aside from a steep gradient in  $f\text{O}_2$  in the upper 50 meters of NSHQ14, the pH and  $f\text{O}_2$  profiles in BA3A and NSHQ14 are similar, suggesting that they are close to steady state.

The maximum pH in BA4A,  $\sim 10$ , is lower than in BA3A and NSHQ14, suggestive of buffering by brucite-water equilibrium [J A M Leong *et al.*, 2021b; J A M Leong and Shock, 2020]. Hole BA2A was essentially dry during drilling. After drilling, the Hole was immediately filled with intermediate alkalinity water pumped from a pool in a nearby canyon. Within 40 days, the Hole had partially collapsed, and the pH had risen to more than 10, up to 11, throughout the remaining open hole. Logging 1 year later yielded pH  $\sim 11$  throughout the  $\sim 120$  m of open hole.



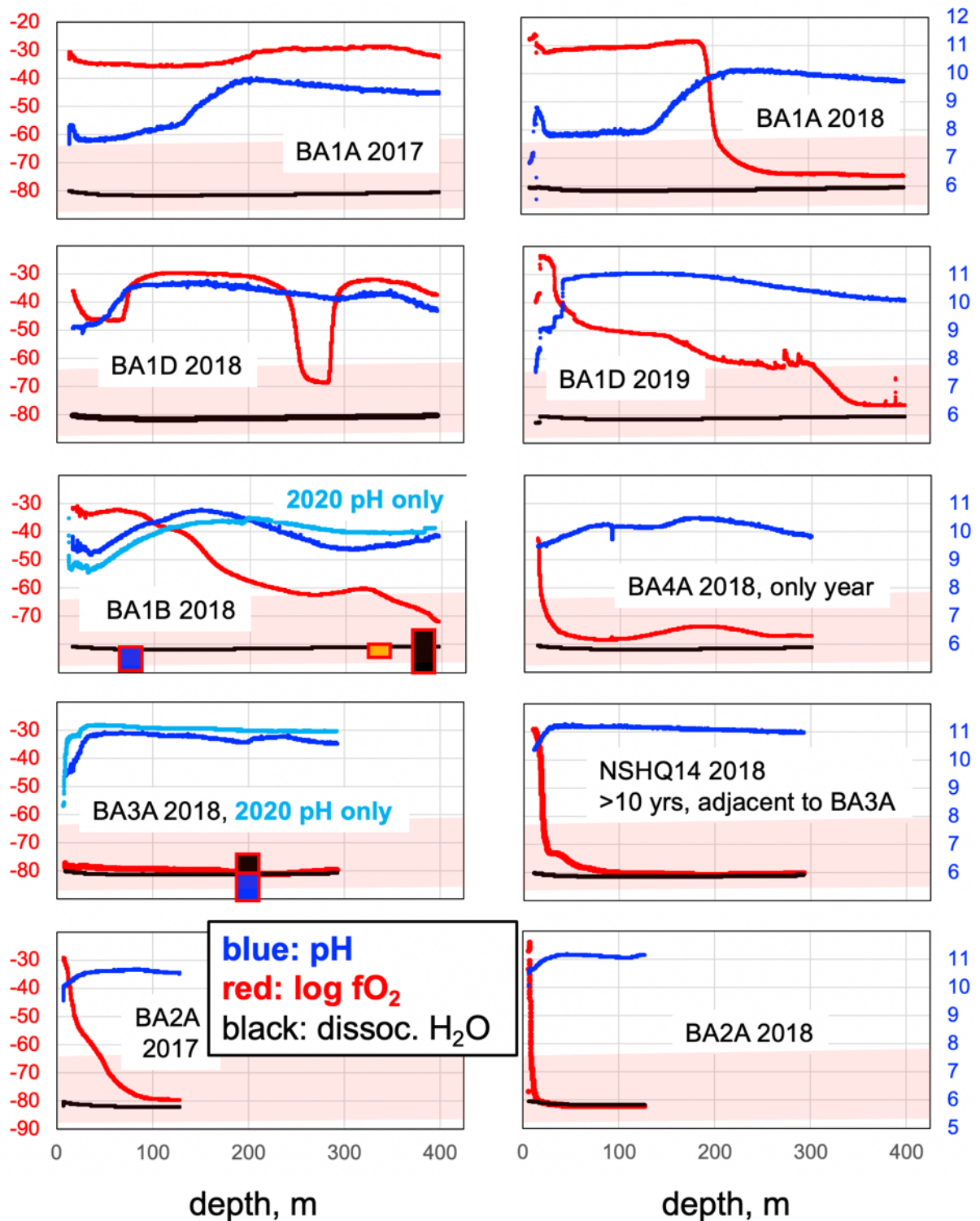


Figure 24: pH and log  $fO_2$  from downhole logging in MBO Holes, and Omani Water Ministry monitoring well NSHQ14.  $fO_2$  from measured Eh, pH, temperature and pressure. Black line illustrates  $fO_2$  below which  $H_2O$  dissociates to form  $H_2$ , calculated from measured temperature and pressure. Rectangles: approximate bounds of  $fO_2$  for selected sulfide-metal associations at 50 MPa from Figure 16. Blue: pentlandite,  $fO_2 < \sim 10^{-82}$  bars; orange: native copper + chalcopyrite,  $10^{-80} > fO_2 > \sim 10^{-82}$  bars; black: awaruite,  $fO_2 < \sim 10^{-75}$  bars. Pink shaded region is bounded on top by the oxygen fugacity buffer  $12 \text{ goethite} = 4 \text{ magnetite} + 6 \text{ H}_2\text{O} + \text{O}_2$ , and on the bottom by the buffer  $\text{magnetite} = 3 \text{ metallic iron} + 2 \text{ O}_2$ .

$fO_2$  throughout Holes BA2A and BA3A, and below 50 meters depth in NSHQ14, appears to be limited by the reduction of  $H_2O$  to form  $H_2$  together with ongoing reduction of remaining ferrous iron in serpentine and brucite (Section 4.8). No calculated  $fO_2$  values fall below the  $H_2O$ - $H_2$  limit at any depth (within the uncertainty of measurement).

## 4. Discussion

### 4.1 Reactive fractionation

Dunite samples in core from the MBO have systematically lower Mg#’s than harzburgites from the same Holes, but the two lithologies have similar contents of Ni, a compatible element during igneous crystal fractionation (Figure 25, left). Dunites in the MBO also have highly variable Ca# (molar  $CaO/(CaO + NaO_{0.5})$ , Figure 25, right), suggesting enrichment of incompatible elements like Na via igneous crystal fractionation. The juxtaposition of these characteristics, with high, nearly constant compatible element concentrations combined with highly variable incompatible element enrichments, is the signature of “reactive fractionation”, in which cooling, olivine-saturated magma begins to crystallize in the uppermost mantle while reacting with residual peridotite. Compatible element concentrations and Mg# in the resulting magmas are “buffered” by diffusive interaction with, and recrystallization of Ni-rich, high Mg# mantle olivine, together with dissolution of high Mg# mantle pyroxene. Meanwhile, decreasing magma mass leads to accumulation of incompatible elements in the remaining liquids. These characteristics have been previously observed in dunites and “troctolites” (plagioclase-bearing lherzolites, *sensu stricto*) sampled via dredging and drilling along the mid-ocean ridges (Section 1.2). Based on these considerations, we infer that the large dunite body intersected by boreholes at Sites BA1, BA2 and BA4 was the locus of reactive fractionation of primitive magmas in the uppermost mantle beneath the spreading ridge that formed the crust of the Samail ophiolite.

Alternatively, one could ask whether the Mg#, Ni contents or Ca#’s of the dunites and harzburgites in the MBO have been modified by alteration. For example, it has been proposed that low Mg#’s and  $MgO/SiO_2$  in some weathered peridotites are produced by preferential dissolution and export of  $MgO$ , as discussed further in Section 4.3. However, because Mg#’s in these rocks are not correlated with  $MgO/SiO_2$  ratios, we do not think that the lower Mg#’s in dunites compared to harzburgites are the result of preferential  $MgO$  removal from the dunites. It is likely that Na has been removed from some igneous rock compositions via dissolution in reacting fluids (Section 4.2). However, this would serve to decrease the variation in Ca#, so that we don’t think this process has been important in producing the highly variable Ca# observed in the MBO dunites.

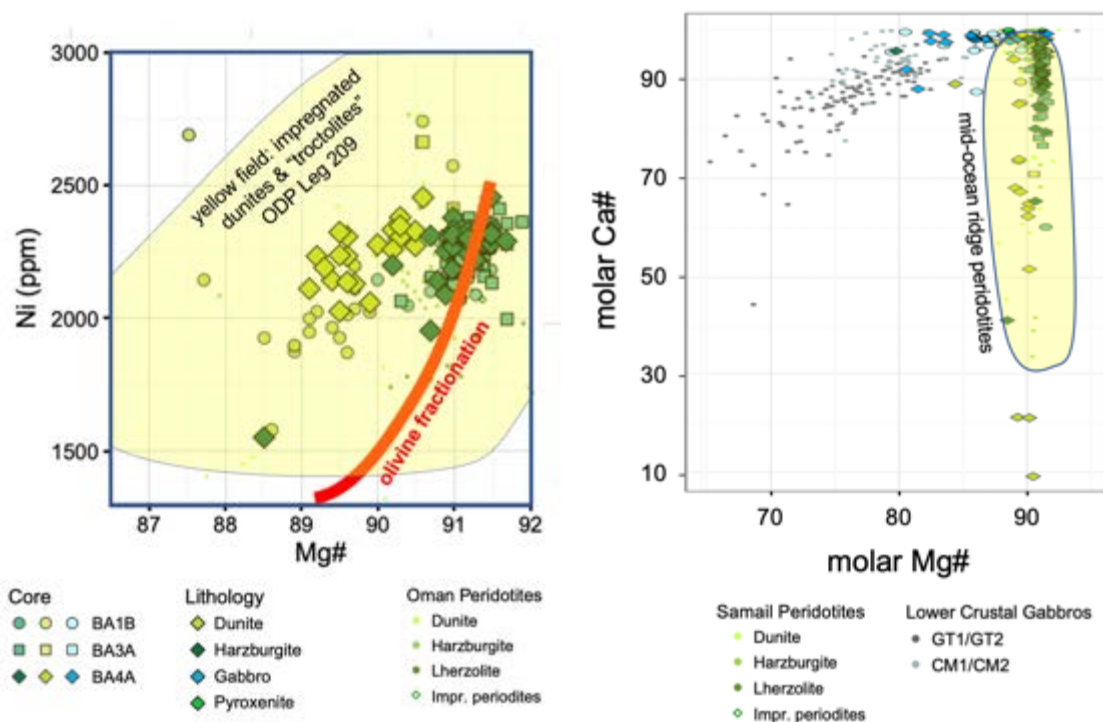


Figure 25: Molar Mg# ( $Mg/(Mg+FeT)$ ) versus Ni concentration (left) and molar Ca# ( $Ca/(Ca+Na)$ ) in bulk compositions of dunite and harzburgite from MBO core, together with lower crustal gabbros from OmanDP Holes GT1A and GT2A, and compiled data on Samail ophiolite mantle samples ("Oman peridotites. Yellow field in the left panel outlines bulk rock compositions of harzburgites, dunites and "troctolites" sampled by drilling at 14-16°N the Mid-Atlantic Ridge on ODP Leg 209 [Kelemen et al., 2007; Seyler et al., 2007; Suhr et al., 2008]. Yellow field in the right panel is for bulk compositions of peridotites dredged from mid-ocean ridges, calculated by Collier and Kelemen [Collier and Kelemen, 2010] using data from Bodinier and Godard [J-L Bodinier and Godard, 2003], Niu [2004] and Tartarotti et al. [2002]. Figures modified from Figure F51 (left) and F54 (right) in Kelemen et al. [Kelemen et al., 2021g].

#### 4.2 Gabbroic dike compositions

Based on the observations and interpretations of the shipboard science team, the protoliths of igneous dikes in core from the MBO appear to have been dominantly wehrlites, clinopyroxenites, olivine gabbros and gabbros [Kelemen et al., 2021d; f; g], rather than websterites and gabbronorites. The latter suite of orthopyroxene-rich rocks forms abundant dikes and small intrusions into the shallow mantle elsewhere in the Wadi Tayin and Samail massifs and is abundant in the northern massifs of the ophiolite (Section 1.3). In this interpretation, the dikes in MBO peridotites are similar to those near the center of the "mantle diapir" inferred to be preserved in the Samail massif, and different from the orthopyroxene-rich dikes that are present in the mantle surrounding the "diapir" [Ceuleneer et al., 1996].

However, interpretation of the MBO dikes in terms of igneous rock compositions should be undertaken with caution. We computed CIPW norms for the bulk compositions of the 40 "gabbro" and "pyroxenite" dikes in MBO core that were analyzed by the shipboard team. In calculating the norms, for simplicity we assumed that all Fe is FeO, and because the science team did not emphasize the presence of relict ferric-iron-bearing oxides in the dikes, perhaps because they are not present.

Most of the dike compositions are distinct from those of common gabbroic and ultramafic, igneous rocks. 65% of the compositions are peralkaline, with normative nepheline, leucite and/or kalsilite. Two peralkaline samples also contain corundum in the norm. None of these low SiO<sub>2</sub> minerals has been observed in less altered mantle dikes, or in crustal gabbros, of the Samail ophiolite. Their presence in the norms is indicative of alkali addition, aluminum addition, and/or SiO<sub>2</sub> extraction during alteration. All but two of the 14 samples that are not peralkaline contain normative orthopyroxene. As noted above, orthopyroxene is common in most Samail mantle dikes, where it is the most SiO<sub>2</sub>-rich mineral. Given the possibility of extensive SiO<sub>2</sub> extraction during alteration, perhaps (some of) the protoliths of peralkaline dikes in MBO drill core were gabbronorites and websterites, after all.

Moreover, 60% of the norms contain more than 50% olivine, whereas gabbroic dikes and intrusions commonly contain approximately cotectic proportions of olivine and plagioclase, ± calcic pyroxene, with less than 30% olivine. On the other hand, ultramafic dikes commonly contain no plagioclase at all. Again, the presence of > 50% olivine in most of the CIPW norms for "gabbroic" dikes may be indicative of SiO<sub>2</sub> removal during alteration, rather than a record of the proportion of olivine present in the igneous protolith of these rock compositions, which have been very substantially modified during alteration.

Finally, the CIPW norms consistently have high molar anorthite contents (An) in normative plagioclase. All have normative An in plagioclase greater than 90%, all but one have normative An > 95%, and 78% have An of 100%. In contrast, igneous plagioclase with more than 90% An is rare, and igneous plagioclase with 100% An is never observed in fresh igneous rocks [Kohut and Nielsen, 2003]. Thus, it seems likely that Na has been removed from these rock compositions during alteration.

#### 4.3 Pervasive silica addition to peridotites

Figure 26 illustrates the compositions of MBO dunites and harzburgites in terms of wt% Al<sub>2</sub>O<sub>3</sub>/SiO<sub>2</sub> versus wt% MgO/SiO<sub>2</sub>. For brevity, throughout the rest of this section, we will refer to these ratios as Al/Si and Mg/Si. This commonly used diagram was first used by Jagoutz et al. to infer the composition of the bulk silicate Earth [Jagoutz et al., 1979]. Such diagrams consistently show that partially serpentinized harzburgites and lherzolites have low Mg/Si at a given Al/Si ratio, compared to the

residues of partial melting and melt extraction in the upper mantle. Dunites, of course, have higher Mg/Si than harzburgites. Mixtures of high Mg# olivine and Al-bearing spinel in dunites have high, nearly constant Mg/Si over a large range of Al/Si, forming a nearly horizontal array on such diagrams. Again, partially serpentinized dunites commonly have Mg/Si lower than for the high Mg#, high Mg/Si protolith.

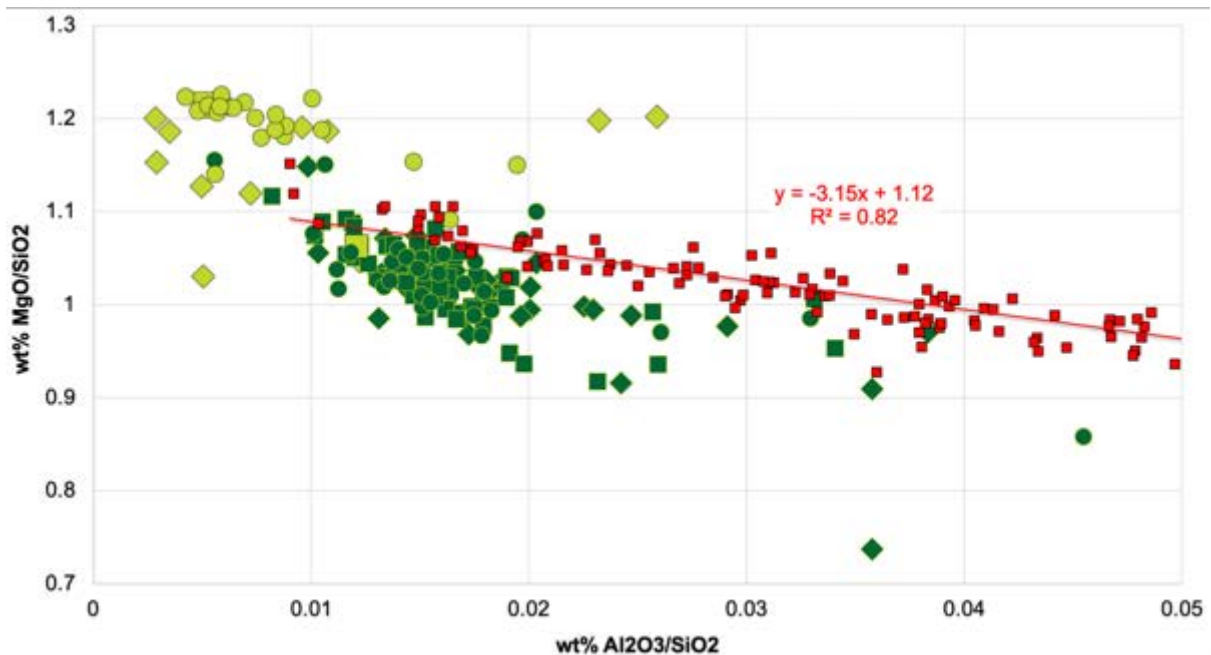


Figure 26:  $\text{Wt\% Al}_2\text{O}_3/\text{SiO}_2$  vs  $\text{wt\% MgO/SiO}_2$  for dunites (light green) and harzburgites (dark green) samples in core from the MBO, compared to estimated and observed compositions of residual mantle lherzolites and harzburgites [red, Asimow, 1999; Baker and Beckett, 1999]. Diamonds: Hole BA1B, squares: Hole BA3A, circles BA4A. MBO data from Kelemen et al. [2021d; f; g].

Low Mg/Si in serpentinized peridotites has often been ascribed to either (1) Mg dissolution and removal from the rocks [Beinlich et al., 2010; de Obeso and Kelemen, 2020; de Obeso et al., 2021; Monnier et al., 2006; Snow and Dick, 1995], or (2) Si addition [de Obeso and Kelemen, 2018]. To these two possible explanations, one might add a third: Perhaps igneous “impregnation”, for example by crystallization of small amounts of relatively Al-rich, Si-rich, Mg-free plagioclase feldspar in pore space in residual peridotites in the shallow mantle, does not follow the same trend as melt extraction, and produces rocks with low Mg/Si at a given Al/Si. This third hypothesis is quantitatively evaluated, and rejected, in Supplementary Text Section 5.

There is little doubt that both processes (1) and (2) occur. For example, Mg dissolution from peridotites is required, as the source of Mg in meter-wide magnesite veins in peridotite elsewhere in the Samail ophiolite. However, the Mg in these veins could be produced by large amounts of Mg removal from small volumes of peridotite, or small amounts of removal from larger volumes. Thus, the relative importance of Mg removal versus Si addition, in producing observed, low Mg/Si ratios in serpentinized peridotites, remains uncertain, and could vary from place to place.

If the low Mg/Si contents were produced mainly by preferential dissolution and export of Mg, one would expect that the size of the Mg/Si deficit, at a given Al/Si, would be positively correlated with Fe/Mg and negatively correlated with bulk rock Mg#. Based on the relationships evident in residual mantle peridotites and MBO dunite samples, we can quantify this by computing the Mg/Si deficit in harzburgites as

$$\text{Mg/Si}_{\text{deficit}} = \text{predicted\_residual\_peridotite\_wt\%\_MgO/SiO}_2 - \text{observed\_wt\%\_MgO/SiO}_2 \quad (7)$$

where

$$\text{predicted\_residual\_peridotite\_wt\%\_MgO/SiO}_2 = -3.15 \times \text{observed\_wt\%\_Al}_2\text{O}_3/\text{SiO}_2 + 1.12 \quad (8)$$

and the Mg/Si deficit in dunites as

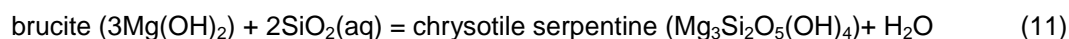
$$\text{Mg/Si\_deficit} = \text{fresh\_dunite\_wt\%\_MgO/SiO}_2 - \text{observed\_wt\%\_MgO/SiO}_2 \quad (9)$$

where

$$\text{fresh\_dunite\_wt\%\_MgO/SiO}_2 \sim 0.30 * \text{observed\_wt\%\_Al}_2\text{O}_3/\text{SiO}_2 + 1.21 \quad (10)$$

assuming spinel-free dunites have Mg/Si of 1.21 (as in many of our dunite samples at low Al/Si), and spinels in dunites contain ~ 50 mole % MgAl<sub>2</sub>O<sub>4</sub> and 50 mole % FeCr<sub>2</sub>O<sub>4</sub>, as is typical.

Supplementary Figure S8 demonstrates that the Mg/Si deficits, estimated in this way, are not correlated with Mg# in dunites or peridotites, nor are they correlated with depth below the surface. Thus, though small amounts of Mg removal may have occurred, it is likely that the pervasively low Mg/Si in MBO harzburgites and dunites has been produced mainly by SiO<sub>2</sub> addition. In particular, many workers have proposed that serpentine can form, in part, via addition of dissolved SiO<sub>2</sub> to brucite, in general [Bach et al., 2004; Bach et al., 2006; J.S. Beard et al., 2009; Frost et al., 2013; Klein and Bach, 2009; Klein et al., 2009; B.M. Tutolo et al., 2018] and related to specific observations in the MBO [Ellison et al., 2021; L.E. Mayhew et al., 2018; Miller et al., 2016; A Templeton et al., 2021; A S Templeton and Ellison, 2020]. Evaluating the likely effect of water/rock reaction, using observed fluid compositions from the MBO and elsewhere in Oman, provides substantial support for the SiO<sub>2</sub> addition hypothesis. Because fluids from peridotite-hosted springs and boreholes in the Samail ophiolite contain appreciable dissolved SiO<sub>2</sub>, in all cases the reaction



is predicted to proceed from left to right, consuming brucite, adding SiO<sub>2</sub> to the rock, and producing serpentine (Supplementary Figure S2). As noted above, fO<sub>2</sub> calculated from Eh, pH, temperature and pressure in some deep borehole waters is very low, closely approaching the limit where H<sub>2</sub>O is reduced to form H<sub>2</sub>. However, in the presence of fluids with appreciable dissolved SiO<sub>2</sub>, even these low fO<sub>2</sub> conditions favor oxidation of the Fe component in brucite, to form ferric-iron-bearing serpentine via



as quantitatively illustrated in Supplementary Figure S2, together with



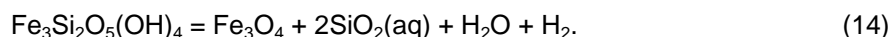
The bulk compositions of almost all dunites and harzburgites in the MBO still retain molar (Mg+Fe<sup>2+</sup>)/Si ratios greater than 1.5 (for example, wt% MgO/SiO<sub>2</sub> greater than ~ 0.9 for a sample with molar Mg/(Mg+Fe<sup>2+</sup>) = 0.9), and thus they require the presence of brucite or cronstedtite as well as serpentine in fully hydrated normative mineral proportions. However, almost all of these calculated, fully hydrated mineral paragenesis are metastable with respect to the observed fluid compositions in peridotite-hosted springs and boreholes, which contain appreciable dissolved SiO<sub>2</sub>. As a result, ongoing, gradual silica addition will continue to shift Mg/Si to lower values over time.

The question arises, if brucite is a common phase throughout most of the core, yet most or all borehole waters contain dissolved SiO<sub>2</sub> concentrations higher than fluids in equilibrium with brucite, what is the source of the SiO<sub>2</sub>? Bach et al. [2004] and Frost et al. [2013] suggested that SiO<sub>2</sub> for conversion of brucite to serpentine could be derived from alteration of orthopyroxene. However, while this silica source may contribute in some parts of the system, many of the cores from the MBO are so highly serpentinized that they contain no relict pyroxene. Paulick et al. [2006] suggested that silicification of peridotites at ODP Site 1268 involved fluids derived from relatively SiO<sub>2</sub>-rich gabbroic rocks, but the proportion of gabbroic lithologies in the MBO is too limited to explain the widespread presence of relatively SiO<sub>2</sub>-rich groundwater in altered peridotites. Similarly, one might consider that SiO<sub>2</sub> is derived from the continental crust and shelf sediments that underlie the Samail ophiolite. However, low Sr isotope ratios in altered peridotites rule out a continental component in fluids during weathering [Supplementary Figure S3 and related text in Kelemen et al., 2011], except in specific

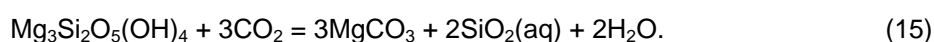


locations just above the basal thrust beneath the ophiolite [Kelemen et al., 2021j] and just below the Cretaceous unconformity above the ophiolite [de Obeso and Kelemen, 2018].

Other suggestions regarding the source of SiO<sub>2</sub> for silicification of brucite involve weathering reactions within the serpentinites themselves. Thus, Klein et al. [2009] and Beard et al. [J.S. Beard et al., 2009] invoked silica dissolution during oxidation of Fe<sup>2+</sup> from serpentine to form magnetite via



On the one hand, this kind of reaction might not be an important source of SiO<sub>2</sub> in the MBO, since many investigators have concluded that formation of magnetite during oxidative, hydrous alteration of peridotite is uncommon below ~ 200°C [e.g., Klein et al., 2014; Klein et al., 2009; McCollom and Bach, 2009; McCollom et al., 2016; Streit et al., 2012]. On the other hand, however, whole core magnetic susceptibility data [Kelemen et al., 2021d; f; g; A Templeton et al., 2021] indicate an average abundance of less than 1.5 wt% magnetite throughout most of the core [e.g, Figure 1 and related calculations in Ellison et al., 2021]. Alternatively, Streit et al. [2012] and Ellison et al. [2021] suggested that dissolved SiO<sub>2</sub> rises due to carbonation reactions such as



Formation of Mg-carbonate minerals by reaction of dissolved CO<sub>2</sub> with peridotite certainly does increase SiO<sub>2</sub> activity, driving up the Si/Mg ratio in silicate minerals [e.g., Falk and Kelemen, 2015; Frost, 1985; Kelemen et al., 2011; Klein and Garrido, 2011; Streit et al., 2012], and indeed, veins in core record Mg-carbonate formation in the shallow portions of Holes BA1B, BA3A and BA4A [Section 3.3 and Kelemen et al., 2021d; f; g]. However, it remains unclear to us whether the proportion and rate of carbonation in the uppermost part of the peridotite-hosted aquifer is sufficient to overcome the buffering capacity of brucite-bearing serpentines and produce the relatively high SiO<sub>2</sub> contents observed in almost all borehole water samples.

In any case, mass balance requires the continued presence of brucite in fully hydrated MBO dunite and harzburgite compositions (Figure 9 and related calculations). In keeping with these calculations, brucite is observed in the MBO core. For example, although sampling for X-ray diffraction onboard DV Chikyū was commonly focused on identifying relatively coarse-grained minerals in veins, shipboard X-ray diffraction data for serpentine-bearing samples detected the presence of brucite in 10 to 15% of analyzed samples, while less biased, electron microprobe, X-Ray diffraction and Raman analyses revealed the presence of brucite in a significant proportion of samples in drill cuttings from rotary boreholes NSHQ14, BA1A and BA2A [Kelemen et al., 2021d; e; L.E. Mayhew et al., 2018; Miller et al., 2016]. Finally, 6 of 11 samples from Hole BA3A, 13 of 15 samples from Hole BA4A, and 21 of 23 samples from Hole BA1B analyzed by quantitative XRD contained appreciable brucite [Ellison et al., 2021] [A Templeton et al., 2021].

In this context, the presence of brucite in the mesh-textured, serpentinite matrix is similar to the presence of highly reduced sulfides in cores from shallow depths in the MBO. While equilibrium may be closely approached at the micro- to nano-scale in these samples, it is likely that mesh cores are far from equilibrium with fluids in nearby fractures that are similar to spring and borehole waters.

#### 4.4 Correlation of water properties and core composition

The shipboard science team quickly realized that there is a strong correlation between carbonate vein abundance and pH in borehole waters, in data from Holes BA1B and BA4A (Figure 27, left; BA1B log vein frequency per 25 m = 11.9 – 1.056 x – pH, R<sup>2</sup> = 0.90; BA4A, log vein frequency per 25 m = 17.443 – 1.68 x pH, R<sup>2</sup> = 0.92). Indeed, interpreting C concentration and <sup>14</sup>C data for peridotite hosted carbonate veins and travertines in the Samail ophiolite, Kelemen and Matter [Kelemen and Matter, 2008] inferred the presence of a shallow horizon of carbonate vein deposition just beneath the surface, with most carbonate veins in a ~ 15 m layer below the present-day erosional surface. This relationship is not as clear in data from Hole BA3A, where a fault at ~ 70 m depth is associated with a peak in carbonate vein frequency. Consistent with the observed correlation in BA1B and BA4A, less comprehensive observations of carbon concentration in core samples show a correlation between the pH of borehole water and the carbon content of core from Hole BA1B (Figure 27, right).

Since the solubility of carbonate minerals decreases rapidly with increasing pH, the shipboard team attributed the correlation of carbonate vein abundance with depth to carbonate precipitation as pH increased along a reaction path, as water descending through the porous aquifer interacts with increasing amounts of peridotite. This seems evident, even obvious... except that it does not explain the correlation between present-day fluid compositions and carbonate abundance, unless the carbonate veins are also young, precipitated from descending fluids near the present-day erosional surface.

As for borehole pH and the carbon content of core, since both the ferric to ferrous iron ratio in core samples and the oxygen fugacity in borehole waters systematically decline with increasing depth in Hole BA1B, one might expect a correlation between borehole water  $fO_2$  and whole rock  $Fe^{3+}/Fe^{2+}$ . As shown in Figure 27, center, this correlation may be present, though it is not very strong.

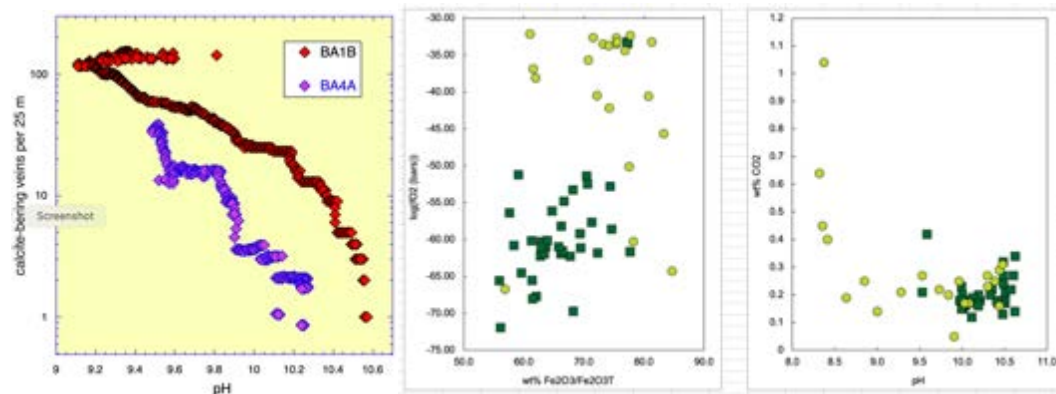
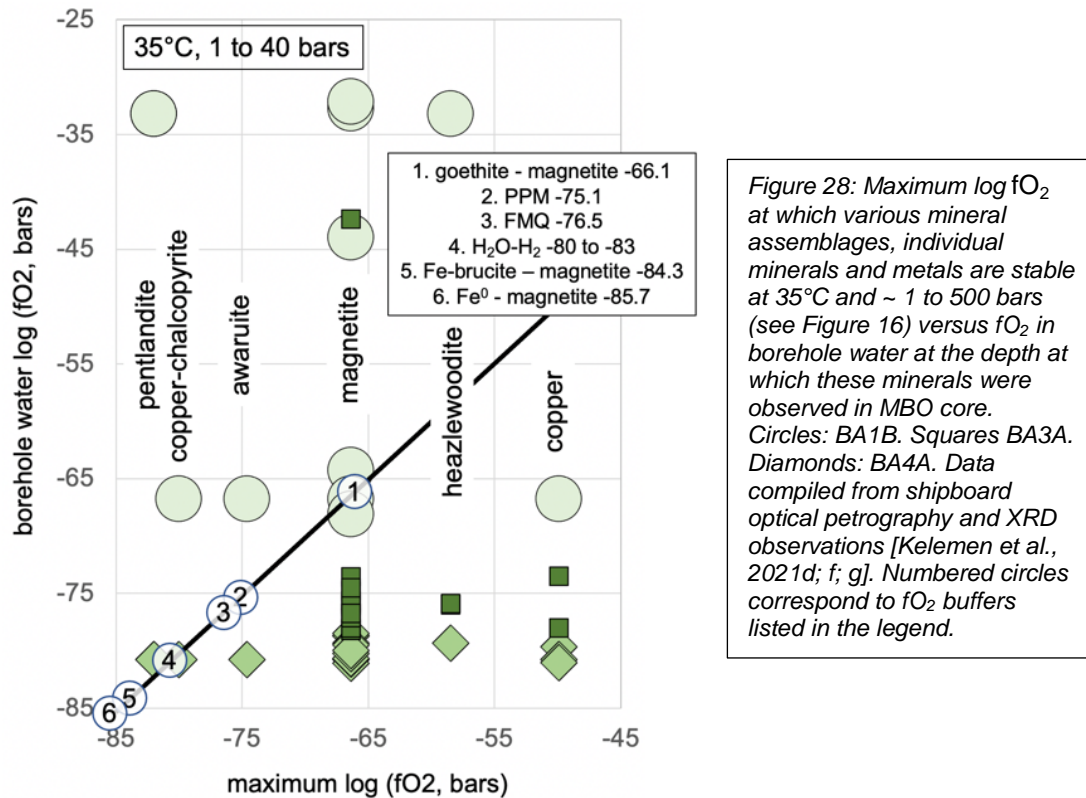


Figure 27: Relationships of core observations to water compositions in boreholes at the same depth. The log of carbonate vein frequency (25 m running average) in Holes BA1B and BA4A decreases with increasing pH in borehole fluids. Ferric to total iron ratios in core from Hole BA1B are weakly correlated with  $fO_2$  in borehole water from the same depth.  $CO_2$  content in core from Hole BA1B is high at relatively low pH, while it is low and less variable at high pH in borehole waters. [Data from this paper and Kelemen et al., 2021d; g].

Carbonates in core from the MBO are generally in veins within fractures, which are macroscopic conduits for fluid flow and probably record high time-integrated water/rock ratios. Thus, one might expect a reasonably strong correlation between carbonate mineral abundance in core, and the composition of water in larger fractures, and in boreholes that are filled primarily by flow in larger fractures.



In contrast, nickel-, copper- and iron-bearing minerals are found throughout our rock samples, in mesh cores as well as veins. These different micro-environments record very different oxidation states which could all be present in peridotite-hosted aquifers at the same time, juxtaposed on very short length scales. For example, as emphasized by de Obeso and Kelemen [2020], some peridotite outcrops elsewhere in the Samail ophiolite preserve almost the entire range of  $fO_2$  on Earth, over a length scale  $\sim 10$  cm, from native metals and highly reduced sulfides in dark serpentinites to rusty orange, clay-bearing assemblages in which all iron is ferric.

Similarly, as noted in Section 3.2, Kelemen et al. [2021d; f, g] and Eslami et al. [Eslami et al., 2018], awaruite, native copper, heazlewoodite, pentlandite and magnetite are found – in various combinations – in the serpentinite matrix of samples from a range of depths, and a corresponding range of  $fO_2$  in borehole waters logged at the same depth (Figure 28). Similar assemblages are reported in other peridotite massifs [e.g., Alt et al., 2013; de Obeso and Kelemen, 2018; 2020; Schwarzenbach et al., 2012; Schwarzenbach et al., 2016; Schwarzenbach et al., 2021].

#### 4.5 Sulfur-rich, “black serpentinite” zone from 30-150 m depth in Hole BA1B

The relatively high sulfur content, up to 0.6 wt% of the BA1B core in some samples located between  $\sim 30$  and 150 meters depth (Figure 12) – is almost certainly hosted in microscopic Ni sulfide together with sulfide – hydroxide  $\pm$  carbonate minerals such as tochilinite and haapalite (Section 2.6) – suggests another potential correlation between the mineralogy of the core and present-day borehole fluid compositions. Sulfur concentrations in the core in this interval [Kelemen et al., 2021d] are 10 to 100 times higher than in samples from outcrops of less weathered, residual mantle dunites and harzburgites from other parts of the Samail ophiolite (5 to 100 ppm in 21 samples from Hanghoj et al. [2010], 100 to 500 ppm in 5 samples from Oeser et al. [2012]). This observation, coupled with the weathering-related redox gradients in the MBO – recorded by the decline in  $Fe^{3+}/(total\ Fe)$  ratios with depth in core compositions, and by declining  $fO_2$  with depth in borehole waters – calls to mind well-known enrichments of Ni and Cu in laterites and supergene ore deposits. These deposits are generally thought to form via dissolution of metals in oxidized, near-surface ground waters, and re-precipitation of those components at greater depth, as downward migrating fluids become reduced by reaction with surrounding rocks.

Indeed, protracted, Late Cretaceous sub-aerial weathering of peridotite elsewhere in Oman formed laterite deposits [S Al Khirbash, 2015; S A Al Khirbash, 2016; 2020]. It could be that the enriched sulfur horizon from ~ 30 to 150 m depth in BA1B core contains sulfur that was originally leached from rocks above the current erosional surface, that have since eroded away. Indeed, this seems likely, since a simple interpretation of this process would require accumulation of sulfur leached from a volume of weathered peridotite that was 10 to 100 times larger than the volume of sulfur-enriched peridotite sampled by the core.

On the other hand, we hypothesize that this chromatographic process, with oxidative dissolution of sulfur from near surface rocks coupled with deeper sulfate reduction and sulfide precipitation, is ongoing. As emphasized by Templeton et al. [A Templeton et al., 2021], during drilling of Hole BA1B, large quantities of “black goo”, stinking of H<sub>2</sub>S, were suddenly produced with the core at a depth of about 30 meters. Templeton et al. [A Templeton et al., 2021] report that XRD data on the “black goo”, from this depth, and also from a fault zone at 70 meters depth, contain a peak at 16° 2-theta, that could correspond to the primary peak for tochilinite. A likely interpretation of the data on sulfide concentration in the core, the “black serpentinite” zone in the core, and the presence of stinky black goo possibly containing tochilinite, is that there is ongoing sulfur reduction and sulfide precipitation in this depth range, fed by sulfate-bearing fluids descending from shallower depths, where fluids leach of sulfur from a shallow, oxidative weathering horizon. Consistent with this hypothesis, at peridotite hosted alkaline springs in Oman, Type II fluids (derived from deeper systems) have orders of magnitude lower dissolved sulfate than Type I fluids which are derived from shallower systems (Leong et al., 2021; Paukert et al., 2012; Chavagnac et al., 2013).

In 2018, a few months after drilling, fO<sub>2</sub> in BA1B borehole waters at 30 to 150 m depth was ~ 10<sup>-30</sup> to 10<sup>-40</sup> bars, too high for sulfide saturation at the low dissolved sulfur concentrations we model ( $\Sigma S < 10^{-3}$  molal, Figure 29). As noted in Section 3.5, because drilling operations used fresh, oxidized drinking water for lubrication, **it may be** that steady state fO<sub>2</sub> (and/or dissolved S contents) at these depths had not yet been attained when the Hole was logged. **In any case**, thermodynamic modeling, presented in Section 4.6, shows that fO<sub>2</sub> drops from ~ 10<sup>-35</sup> bars to 10<sup>-65</sup> bars – where sulfide saturation is predicted in our Step 2 models illustrated in Figure 29 – over a very short interval of reaction progress. Thus, a small increment of reaction between borehole waters and surrounding rocks would lead to sulfide precipitation.

**More generally**, borehole waters may record ambient fluid compositions in large fracture systems, which are probably the locus of most fluid flow in the peridotite-hosted aquifer. Thus, prior to drilling, relatively oxidized waters with fO<sub>2</sub> from 10<sup>-30</sup> to 10<sup>-40</sup> bars may have already been present in the larger fracture systems at 30 to 150 m depth. However, where these waters infiltrate smaller fracture systems, and/or react diffusively with surrounding rocks, it is likely that they become highly reduced and sulfide-saturated, contributing to continued accumulation of sulfide minerals in the black serpentinite zone. In this scenario, over time the erosional surface will continue to migrate downward with respect to the present-day surface, and the supergene enrichment zone will also migrate downward, as sulfides at the top of the zone are gradually oxidized by near surface fluids, and begin to dissolve. In this way, such zones can be both ancient, and active.

It has been proposed that the formation of supergene metal enrichment, via low temperature sulfide precipitation, is unlikely without the intervention of sulfate-reducing bacteria [e.g., Tornos et al., 2019; Zammit et al., 2015]. In turn, Templeton et al. [A Templeton et al., 2021] report that sulfate-reducing microbial activity has not yet been detected in extracts from BA1B core samples in the 30 to 150 meter black serpentinite zone. In contrast, extracts from core retrieved from greater depth, where borehole waters record more reducing conditions, show evidence of biological sulfate reduction in the lab. The maximum rates of microbial sulfate reduction occurred in samples from 280 m depth, where fO<sub>2</sub> in borehole water was ~ 10<sup>-62</sup> bars in 2018.

On the basis of these observations, one hypothesis might be that microbial reduction of sulfate at ~ 250 to 300 m depths produces H<sub>2</sub>S, which then migrates **upward** through the rocks – perhaps along fault zones at 30 and 160 meters depth – to produce the observed sulfur enrichment in rocks at 30 to 150 m depth. However, here we suggest a simple alternative, that supergene sulfur enrichment is ongoing, with **descending**, oxidized, near-surface fluids dissolving sulfur from the oxidized red zone from 0 to 30 m depth, and transporting dissolved sulfate **downward**. This continues until the fluids become reduced by reaction with serpentinites, and precipitate sulfides in the black serpentinite zone

from 30 to 150 meters depth. In this alternative interpretation, either microbial activity is not essential to this process, or the microbes that facilitate this relatively shallow process have not yet been detected in samples extracted from core. Indeed, in water samples from obtained from the 41 to 132 m depth interval of Hole BA1A via packer sampling, Nothhaft et al. [2021a] found that 20 to 92% of 16S rRNA gene amplicon sequences were affiliated with a class of bacteria supported by sulfate reduction.

#### 4.6 Reaction path modeling including Cu, Ni and S

In order to quantify the hypothesis that the black serpentine zone observed in BA1B core may form via supergene enrichment, we conducted geochemical reaction path modeling, using methods described in detail in Section 2.5. We followed the general rubric outlined by Barnes and O'Neil [Barnes and O'Neil, 1969] and Neal and Stanger [Neal and Stanger, 1985], and modeled by Bruni et al. [Bruni et al., 2002], Paukert et al. [Paukert et al., 2012] and Leong et al. [J A M Leong et al., 2021b]. In these models, rainwater falling on peridotite dissolves  $Mg^{2+}$  and other components from the rock, charge balanced mainly by uptake of  $CO_2$  from air to form  $HCO_3^-$ . This process forms Mg- $HCO_3^-$ -rich waters with pH ~ 8.5 to 10, which Barnes and O'Neil termed Type I. As extensively discussed elsewhere [e.g., Kelemen et al., 2011 and references therein], Type I waters in the Samail ophiolite are typically sampled from wadis (small canyons) and shallow groundwater wells in the peridotite-hosted aquifer. Some Type I fluids are then thought to continue reacting with peridotite at greater depth, isolated from the atmosphere. Precipitation of serpentine and Mg-bearing carbonates along this reaction path, together with dissolution of Ca-bearing phases, produces low Mg and C, Ca-OH rich fluids with pH > 10 and low  $fO_2$ , which Barnes and O'Neil termed Type II waters. In all of these respects, our new models do not depart significantly from past results.

However, our new models incorporate dissolved S, Ni and Cu, together with a host of metal and sulfide minerals, and thus can be used to evaluate potential mechanisms of supergene sulfide enrichment in the serpentinized peridotites hosting Hole BA1B. The results of these models are depicted in Figure 29. As predicted on qualitative grounds, formation of Type I fluids via reaction open to  $CO_2$ -uptake from air is accompanied by dissolution of sulfur-bearing phases. In turn, reaction of Type I fluids with serpentinite, closed to  $CO_2$  uptake from air, leads to precipitation of serpentine, dolomite and hematite, together with production of highly reduced fluids that precipitate sulfides and native metals. When dissolved  $O_2$  concentrations drop below those of dissolved  $H_2$ , a dramatic drop in  $fO_2$  from  $10^{-35}$  to  $10^{-65}$  bars over a narrow range of water rock ratios ( $10^{3.391195}$  to  $10^{3.390982}$ ). This is accompanied by saturation in native copper and sulfide minerals cubanite, millerite and pyrite. As  $fO_2$  continues to fall, and sulfide precipitation also lowers  $fS_2$ , hematite precipitation is supplanted by magnetite, there is another big drop in  $fO_2$  over a narrow range of reaction progress, overall sulfide precipitation declines, and the sulfide and metal assemblages associated with magnetite that have been observed in serpentinite mesh cores (Section 3.2) – heazlewoodite, chalcopyrite, and ultimately awaruite – are predicted to form.



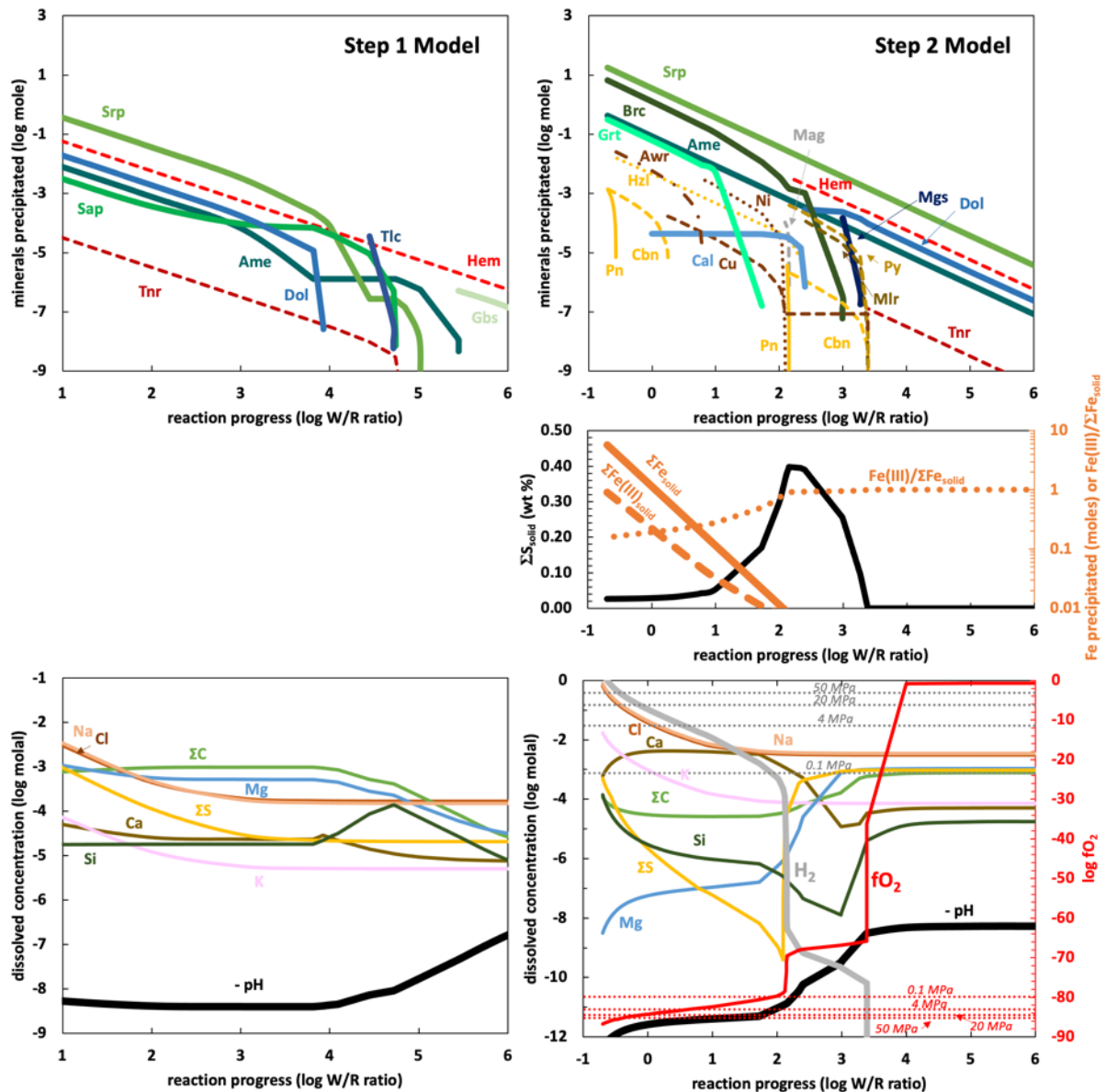


Figure 29: Results of thermodynamic reaction path modeling at 35°C and 50 MPa. From the perspective of fluid gradually reacting with rock, reaction progress increases from right to left, as the water/rock ratio (W/R) decreases.

Because the Klein et al. [2013] thermodynamic database used for this modeling (Section 2.5) is limited to 50 MPa, these results for 50 MPa, whereas the maximum pressure in MBO boreholes is ~ 4 MPa. Fortunately, few relevant equilibria (other than H<sub>2</sub> saturation in water!) are dependent on pressure in this range.

Results are presented in terms of abundance of precipitated minerals (top row) and dissolved species (bottom row). Bottom right panel also illustrates fO<sub>2</sub> (red line), fO<sub>2</sub> values at the H<sub>2</sub>O-H<sub>2</sub> limit where water breaks down to form H<sub>2</sub> (horizontal, dashed red lines), and corresponding dissolved H<sub>2</sub> concentrations at H<sub>2</sub>-gas saturation (horizontal, dashed grey lines) at 0.1, 0.4, 20 and 50 MPa.

Step 1 (lefthand panels) simulates reaction of rainwater with peridotite, in a system in equilibrium with air. Step 2 (righthand panels) simulates reaction between water produced in step 1 and serpentinized peridotite, in a system isolated from air. Step 1 produces oxidized, clay- and hematite-bearing serpentinites (upper left panel) while dissolving sulfur from the protolith, and solute-rich fluids with pH ~ 8 and ~ 1 millimole dissolved sulfur (lower left). Step 2 produces reduced serpentinites with magnetite, sulfides, and metal alloy (upper right), together with sulfur-, magnesium-, silicon- and carbon-poor fluids (lower right).

A sharp sulfide precipitation front accompanies a drop in fO<sub>2</sub> from ~ 10<sup>-35</sup> to 10<sup>-65</sup> bars at a water/rock mass ratio ~ 10<sup>3.39</sup>. Illustrating this, the middle panel on right illustrates sulfur concentration in precipitated solids at a given water/rock ratio (black line). This forms a sulfur-rich zone at water/rock ratios from ~ 10<sup>3.3</sup> to 10, similar in origin to supergene sulfide deposits. Sulfide, Fe-oxide and metallic phases precipitated along the reaction path are further illustrated in Supplementary Figure S9.

The middle panel also illustrates results in terms of iron redox (orange lines). Cumulative  $\text{Fe}^{3+}/(\text{total Fe})$  in all precipitated solids is illustrated with small dashes, cumulative moles Fe precipitated are shown with the solid line, and cumulative moles of  $\text{Fe}^{3+}$  precipitated are tracked with large dashes. Because this reaction path model includes solid solutions, whereas the calculations in Figure 31 are for pure mineral end-members, the results in the middle panel provide a crucial complement to those in Figure 31, for understanding the evolution of  $f\text{O}_2$ . Although  $\text{Fe}^{3+}/(\text{Fe total})$  of precipitating solids declines with reaction progress at a water/rock ratio less than  $\sim 10^2$ , it only falls by a factor of ten in the bulk, and a factor of five in the serpentine (Supplementary Figure S10), whereas the amount of precipitated solids (mostly brucite + serpentine) increases by a factor of  $\sim 100$  from water/rock of  $10^2$  to  $10^{0.8}$ . In this model at 50 MPa,  $\text{H}_2$  partial pressure is not limited to 4 MPa, (dissolved  $\text{H}_2 \sim 30$  mM) but instead increases to 50 MPa saturation (water/rock  $\sim 10^{0.8}$ ,  $\sim 375$  mM dissolved  $\text{H}_2$ ). In the MBO system at  $\sim 4$  MPa, dissolved  $\text{H}_2$  concentration would be limited to  $\sim 30$  mM,  $f\text{O}_2$  would be fixed at about  $10^{80}$  bars, and  $\text{H}_2$  gas would evolve with continued oxidation of  $\text{Fe}^{2+}$  in the protolith to form increasingly large cumulative masses of  $\text{Fe}^{3+}$ -bearing serpentine.

Abbreviations: Serpentine (Srp, chrysotile + greenalite +  $\text{Fe}^{2+}$ -cronstedtite solid solution), talc (Tlc, talc + minnesotaite solid solution), Mg-saponite (Sap), Mg-amesite (Ame), garnet (Grt, andradite + grossular solid solution), magnesite (Mgs), calcite (Cal), dolomite (Dol), gibbsite (Gbs), hematite (Hem), brucite (Brc, Mg and  $\text{Fe}^{2+}$  solid solution), magnetite (Mag), tenorite (Tnr), millerite (Mlr), cubanite (Cbn), pentlandite (Pn), heazlewoodite (Hzl), pyrite (Py), native copper (Cu), native nickel (Ni), and awaruite (Awr). Amesite is treated as an end-member phase, not part of the serpentine solid solution. In natural rocks, amesite is a component in serpentine solid solutions. Similarly, native Ni and awaruite ( $\text{Ni}_3\text{Fe}$ ) are treated as end-member phases in the calculation, whereas in some studies a range of Fe/Ni ratios has been observed.

Some potentially significant departures of model results from observations include saturation in millerite, cubanite and pyrite, which haven't been observed in the core, and precipitation of Ni metal from W/R  $\sim 100$  to 10, prior to formation of awaruite. The latter discrepancy is perhaps explained by the fact that the method used for modeling cannot account for solid solutions. Frost [1985] and Sleep et al. [2004] noted that if there were complete solid solution from Ni to Fe metal, one might use the Fe/Ni ratio as an indicator of  $f\text{O}_2$ . In essence, because Ni-NiO occurs at much higher  $f\text{O}_2$  than Fe-FeO, one could anticipate a negative correlation between oxygen fugacity and the Fe content of NiFe alloys. Low temperature phase equilibria in this system are uncertain [Cacciamani et al., 2010; Howald, 2003; Klein and Bach, 2009; Navak and Meyer, 2015]. Fe-rich "taenite", "awaruite" and "tetraetaenite" are reported in terrestrial serpentinites [Botto and Morrison, 1976; Navak and Meyer, 2015], while Sciortino et al. [2015] and Ellison et al. [2021] analyzed "awaruite" with low Fe contents in serpentinites, including in a sample from 100 m depth in Hole BA3A. Similarly, incomplete observations, and/or lack of solid solution data in the thermodynamic calculations, may be responsible for model predictions of sulfides that have not (yet?) been observed in core, and conversely for the lack of model predictions of sulfides that are observed.

Overall, solid reaction products are predicted to have high total sulfur contents in the range of water rock ratios from  $10^3$  to  $10^1$ , which we propose is the mechanism for the formation of the sulfur-rich, black serpentinite zone from  $\sim 30$  to 150 m depth in BA1B core. More generally, the model whose results are depicted in Figure 29, and other, similar, previous models of the evolution of Type I and Type II fluids in peridotite-hosted aquifers, include the implicit assumption that all of the reactions involved are ongoing, perhaps even at steady state. Of course, this assumption is approximate, and it is likely that the rocks contain armored relicts of earlier mantle and alteration phase assemblages. With that said, specific instances of apparent disequilibrium, relict mantle minerals, or "out of sequence" alteration assemblages **may** be preserved relicts of prior events, but they **could also be** indicative of micro to meter scale variation in fluid/rock ratios in a reactive system that is close to equilibrium at small length scales, over times of tens to hundreds of thousands of years.

#### 4.7 Rate of ongoing alteration

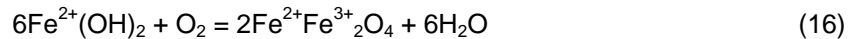
The  $^{14}\text{C}$  data for carbonate veins (Section 3.4, Supplementary Table 3), together with the fact that texturally young, waxy serpentine veins are intergrown with, and locally crosscut, young carbonate veins, indicates that serpentine formation occurred in the Pleistocene and probably continued in the Holocene. Together, waxy serpentine abundances  $\sim 5$  volume percent, and measurable  $^{14}\text{C}$  "ages" of 20 to 50 kyrs for 2/3 of the carbonate samples analyzed, yield an order of magnitude estimate of  $\sim 1$  vol% serpentine formation per 10,000 years, equivalent to a volume fraction of  $3 \cdot 10^{-14}/\text{s}$ . This estimate is roughly consistent with new, experimentally-based estimates of low temperature serpentine formation from olivine [Lamadrid et al., 2021] and estimates of the Fe-redox rate based on observed  $\text{H}_2$  and  $\text{CH}_4$  gas fluxes [J A Leong et al., 2021a]. In keeping with other work and considerations in Section 4.3, we hypothesize that most of the ongoing serpentine formation occurs via addition of

aqueous SiO<sub>2</sub> to brucite to form Mg-rich serpentine, and oxidation of Fe-brucite to form ferric-iron-bearing serpentine.

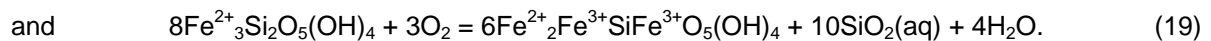
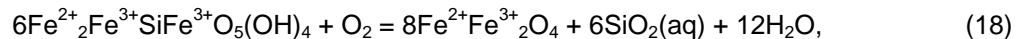
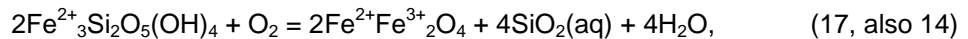
#### 4.8 Controls on fO<sub>2</sub>, pH and dissolved SiO<sub>2</sub> in borehole waters

Figure 30, left, shows that fO<sub>2</sub> in some boreholes very closely approaches the limit where H<sub>2</sub>O is reduced to form H<sub>2</sub>. Also, much has been made of the observation of H<sub>2</sub>-rich gases bubbling out of peridotite-hosted alkaline springs in the Samail ophiolite and elsewhere [e.g., *Boullart et al.*, 2013; *Neal and Stanger*, 1985; *Sano et al.*, 1993; *Vacquand et al.*, 2018]. It is proposed that reactions between water and peridotite produce highly reduced fluids, which evolve free H<sub>2</sub> gas. Indeed, fO<sub>2</sub> in the lower parts of BA3A 2018, NSHQ14 2018, and BA2A appears to be fixed by a combination of the reaction 2H<sub>2</sub>O = 2H<sub>2</sub> + O<sub>2</sub> reaction itself, and some sink for O<sub>2</sub> at low fO<sub>2</sub>. Obviously, in the presence of excess water, fO<sub>2</sub> cannot decline below the value fixed by this reaction at a given temperature and pressure. Conversely, the rocks still contain ~ 3 wt% ferrous iron (Figure 12). Since the average proportion of magnetite inferred from magnetic data is less than 1.5 wt%, and only 31 wt% of magnetite is composed of FeO (accounting for < 0.5 wt% FeO in bulk rocks), some ferrous iron must still reside in serpentine or brucite, as confirmed by X-ray and Raman spectroscopic analyses of serpentine and brucite in BA3A core samples [*Ellison et al.*, 2021].

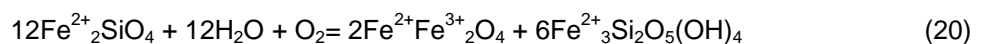
Ongoing oxidation of the remaining Fe<sup>2+</sup> in serpentine and/or brucite, could provide a continuing sink for O<sub>2</sub>, with concurrent production of H<sub>2</sub>, thus pinning fO<sub>2</sub> at the H<sub>2</sub>O-H<sub>2</sub> reaction limit. If this hypothesis is correct, and if we could obtain gas-tight samples of pore fluid from the rocks surrounding the bottoms of these Holes, we predict they would be H<sub>2</sub>-saturated. We are not certain of the nature of the specific reactions that continue to consume O<sub>2</sub>, and produce H<sub>2</sub>, at the H<sub>2</sub>O-H<sub>2</sub> limit. Magnetite is stable with respect to Fe-brucite, down to about 2 log units below H<sub>2</sub>O-H<sub>2</sub> (Figure 31), so that brucite oxidation could play a role via



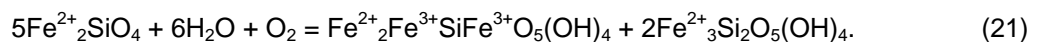
Similarly, remaining Fe<sup>2+</sup> in serpentine (greenalite, cronstedtite) could be oxidized to form magnetite and/or cronstedtite via



Reactions 16, 17 and 18 involve production of magnetite, and thus may be inconsistent with various observations and calculations indicating that magnetite production during peridotite alteration is limited at low temperature (Section 4.3). However, it may be that prior work has not fully explored the very low fO<sub>2</sub> conditions near the H<sub>2</sub>O-H<sub>2</sub> limit at low temperature and pressure, and/or that the thermodynamic data are uncertain. Note that the results of the reaction path model in Figure 29, incorporating solid solutions, include a small amount of magnetite precipitation at a water/rock ratio ~ 200, and a predicted increase in the total amount of Fe<sup>3+</sup> incorporated in serpentine with reaction progress at water/rock less than 200, with fO<sub>2</sub> at the H<sub>2</sub>O-H<sub>2</sub> fO<sub>2</sub> limit. In addition to providing an ongoing sink for O<sub>2</sub> (source of H<sub>2</sub>) at the H<sub>2</sub>O-H<sub>2</sub> limit, reactions 17-19, involving continued reduction of Fe<sup>2+</sup> in serpentine, could also be providing a source of "excess" dissolved SiO<sub>2</sub> for brucite silicification (Section 4.3). An additional potential O<sub>2</sub> sink in the MBO might be ongoing serpentinization of relict olivine, which is observed in less altered core samples, particularly in the lower part of Hole BA1B. This could include reactions such as fayalite-greenalite-magnetite



and/or fayalite-greenalite-cronstedtite



In contrast to the highly reduced water inferred from 2018 data for the deeper parts of Holes BA2A, BA3A and NSHQ14, fO<sub>2</sub> calculated from logging data for Holes BA1A and BA4A in 2018, and BA1D

in 2019 is higher, and appears to approach an asymptote at about 4 log units above the  $H_2O-H_2$  limit toward the bottoms of these Holes. This might be explained by various proposed buffers for  $fO_2$  involving awaruite, andradite, diopside and/or calcite [e.g., *Ellison et al., 2021; Frost and Beard, 2007; J A Leong et al., 2021a*]. However, Ni and Ca, are relatively minor components in the rocks, suggesting that equilibria involving these Ni- and Ca-bearing minerals may have limited buffering capacity. Instead, we suggest that equilibria involving  $Fe^{2+}$ -Mg solid solutions in cronstedtite  $((Mg, Fe^{2+})_2Fe^{3+}SiFe^{3+}O_5(OH)_4)$ , chrysotile  $((Mg, Fe^{2+})_3Si_2O_5(OH)_4)$ , and brucite  $(Mg, Fe^{2+})(OH)_2$  are controlling  $fO_2$  in waters near the bottom of these Holes. Figure 31 illustrates the results of thermodynamic calculations illustrating that, depending on the  $Mg/Fe^{2+}$  content of the cronstedtite, these reactions constrain  $fO_2$  to within 2.5 to 4.5 log units of the  $H_2O-H_2$  reaction. If we consider only the Mg-cronstedtite endmember, then the  $fO_2$  range is 3.5 to 4.5 log units above  $H_2O-H_2$ , which in turn is consistent with the apparent asymptotic  $fO_2$  values for water at the bottom of Holes BA1A 2018, BA1D 2019 and BA4A 2018. The hypothesis that these brucite-serpentine mineral assemblages control  $fO_2$  in serpentinizing systems at depth is appealing, because these minerals are composed of the major elements present in the rocks.

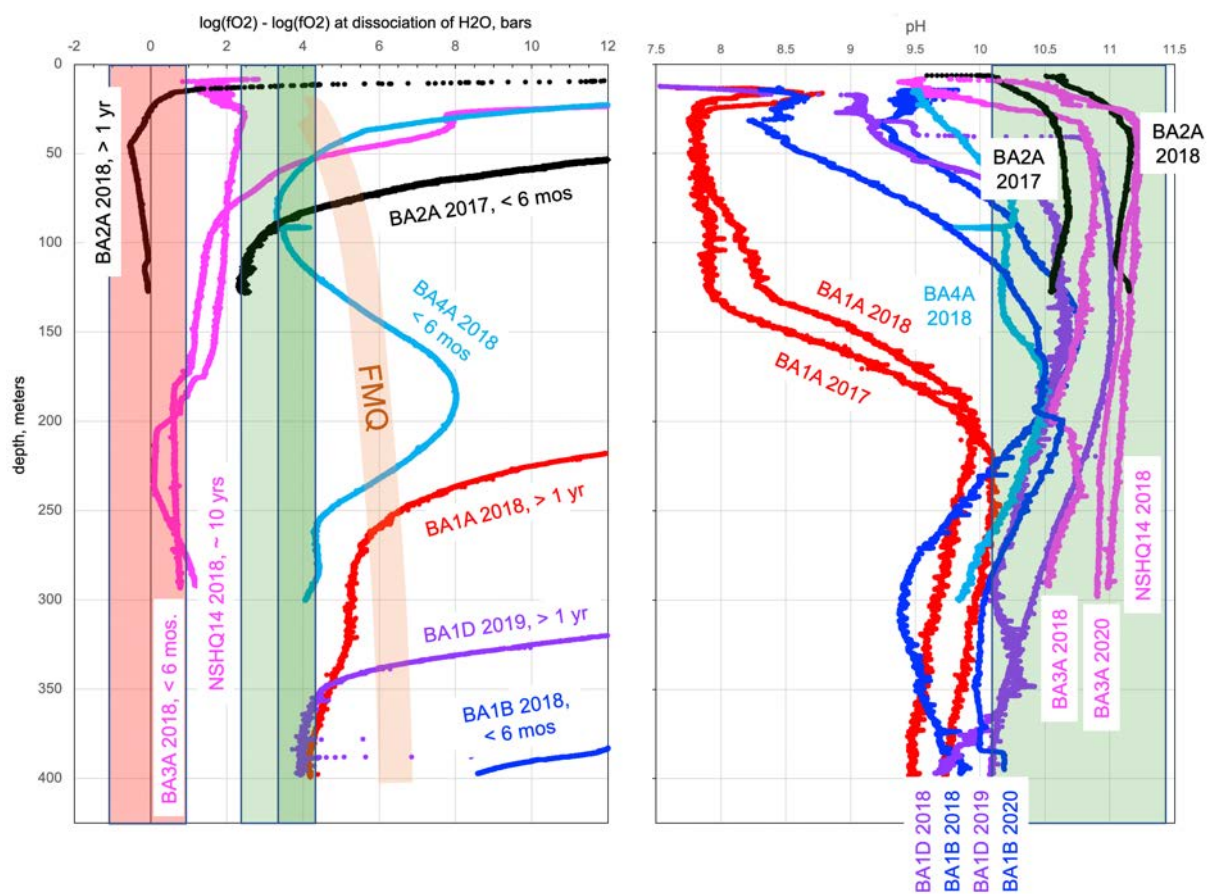


Figure 30: Compiled data on downhole variation in  $fO_2$  (left) and pH (right) in MBO borehole waters. Red rectangle on left illustrates  $fO_2$  for reduction of  $H_2O$  to form  $H_2$  at  $\sim 35^\circ C$  and 40 bars,  $\pm 1$  log unit (likely precision of borehole  $fO_2$  calculated from Eh, pH, temperature and pressure). Green rectangle in lefthand panel illustrates range of  $fO_2$  set by reactions involving brucite, cronstedtite, and chrysotile-greenalite solid solutions. Green rectangle in righthand panel illustrates pH range for coexisting brucite, serpentine and andradite. Orange bar in lefthand panel illustrates the position of the oxygen fugacity buffer FMQ (fayalite +  $O_2$  = magnetite + quartz) along the geotherm measured in our boreholes.

In addition, brucite-serpentine equilibria also have a potentially important control on dissolved  $SiO_2$  concentrations and pH in coexisting fluids. Mg-brucite-Mg-chrysotile and Mg-chrysotile-Mg-talc equilibria constrain  $SiO_2$  activity in fluids to range from  $10^{-8.2}$  to  $10^{-4.7}$ . This range of  $SiO_2$  activities encompasses observed  $aSiO_2$  in almost all peridotite-hosted borehole and alkaline spring water samples from the Samail ophiolite with  $pH > 9$  [*J A M Leong et al., 2021b*]. In turn, Mg-brucite-Mg-chrysotile equilibrium in this  $SiO_2$  activity range constrains pH to be  $\geq 10$ . Mg-brucite and Mg-

chrysotile in combination with andradite, which is commonly intergrown with serpentine in core samples from the MBO [Ellison et al., 2021; Kelemen et al., 2021d; f; g; A Templeton et al., 2021], constrain pH to  $\leq 11.5$ . Though pH in borehole waters increases downward near the top of most holes, it is variable at depth, and does not show the asymptotic patterns that are evident in the  $fO_2$  data. However, with the exception of BA1A 2018, the range of pH in all borehole waters logged more than a year after drilling is 10 to 11.3, consistent with the hypothesis that brucite + serpentine  $\pm$  andradite equilibria control  $fO_2$  in the lower part of these boreholes.

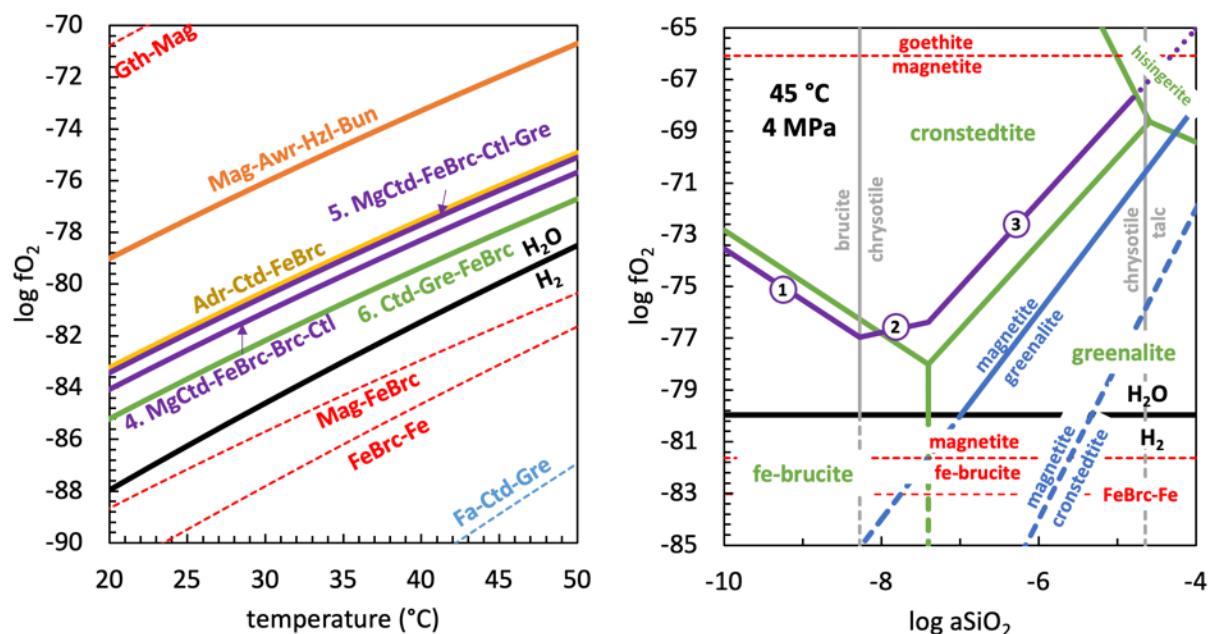
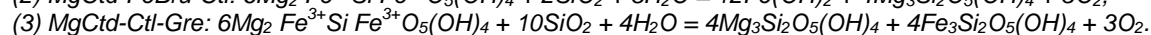
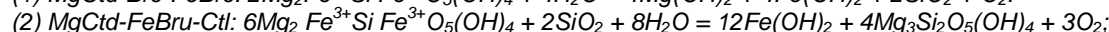
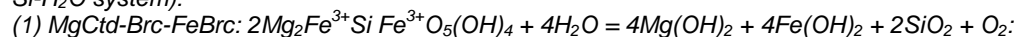
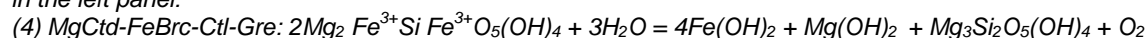


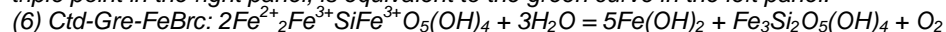
Figure 31: Phase diagrams in terms of temperature vs  $\log fO_2$  (left) and  $\log$  activity of dissolved  $SiO_2$  vs  $\log fO_2$  (right), for various reactions involving Mg- and Fe-brucite (Brc, FeBrc), Mg- and  $Fe^{2+}$ -cronstedtite (MgCtd, Ctd), chrysotile (Ctl), greenalite (Gre), goethite (Gth), magnetite (Mag), awaruite (Awr), heazlewoodite (Hzl), bunsenite (Bun), andradite (Adr), fayalite (Fa) and hisingerite at 45°C and 4 MPa ( $T$  and  $P$  near the bottom of BA1A, BA1B and BA1D). Because of the choice of thermodynamic database, these results do not incorporate solid solutions. In the right panel, the stability fields of Fe-brucite, greenalite, Fe-cronstedtite, and hisingerite in the Fe-Si- $H_2O$  system are indicated by the green lines. Violet lines indicate phase boundaries involving Mg-cronstedtite (Mg-Fe-Si- $H_2O$  system):



The stability of reaction (3) with respect to hisingerite was not calculated and hence this reaction is shown as a dashed violet line where hisingerite is stable in the Mg-free system. Temperature dependent  $fO_2$  set by the intersections between lines (1) and (2) and lines (2) and (3) in the right panel are shown by the two violet curves in the left panel:



(5)  $MgCtd-FeBrc-Brc-Ctl: 6Mg_2Fe^{3+}SiFe^{3+}O_5(OH)_4 + Fe_3Si_2O_5(OH)_4 + 9H_2O = 15Fe(OH)_2 + 4Mg_3Si_2O_5(OH)_4 + 3O_2$   
Temperature-dependent  $fO_2$  set by the greenalite, Fe-cronstedtite, and Fe-brucite assemblage, which is at green triple point in the right panel, is equivalent to the green curve in the left panel:



Thus, to summarize, brucite - serpentine reactions [( $\pm$  andradite, *J A M Leong et al., 2021b*), can potentially explain  $fO_2$ , pH and dissolved  $SiO_2$  contents observed in reduced water at depths greater than 250 meters in BA1A 2018, BA1D 2019, and BA4A 2018, together with the pH and dissolved  $SiO_2$  contents in even more reduced waters observed in BA3A 2018, NSHQ14 2018, and BA2A 2018. While minor phases clearly record  $fO_2$ , pH and/or  $aSiO_2$  conditions in this range, we propose that minerals composed of major elements in the rock largely control these conditions.

Finally, water in BA1A 2017, BA1B 2018, BA2A 2017, and probably BA1D 2018, apparently records addition of fresh, high  $fO_2$  water during drilling, suggesting that more than six months may be required for water in these Holes to reach steady state variation in  $fO_2$  vs depth. Water in BA3A 2018 – highly reduced from top to bottom, and very similar to water in nearby Hole NSHQ14 drilled more than ten



years before logging – appears to be an exception to this “rule”. In interpreting the logging data, an additional factor to consider is that flow measurements indicated that (a) there is a relatively fast flowing, low pH aquifer near the top of BA1A, and 9b) water flowed down the upper part of BA1A for more than a year after drilling, possibly because this is the natural process, and possibly because the borehole connected two previously isolated aquifers.

## 5. Conclusions

In this paper, we've provided an overview of some initial results from the Oman Drilling Project's Multi-Borehole Observatory (MBO). Investigations of water and rock samples, from three cored and four rotary boreholes in the MBO have yielded a wealth of new information, which we have just begun to understand. Host rocks to the boreholes are partially to almost completely serpentinized residual harzburgites and replacive dunites from the upper few kilometers of the mantle section of the Samail ophiolite. Dunites show evidence for “reactive fractionation”, in which cooling, crystallizing magmas in the uppermost mantle continued to react with surrounding harzburgites, producing a distinctive trend of incompatible element enrichment at high, nearly constant Ni concentrations and molar Mg#'s. These mantle lithologies have been 65 to 100% hydrated, to form serpentine and other minerals. Similarly, the ferric to total iron ratio in core varies from 50 to 90%.

In the deepest cored hole, BA1B, the extent of hydration, oxidation, and carbonate vein formation all decrease systematically with increasing depth below the surface, and gradients in borehole water composition are correlated with variation in core composition, suggesting that much of the alteration is relatively young, ongoing, and related to low temperature weathering. This inference is borne out by the presence of young serpentine veins, which are intergrown with, and locally crosscut, carbonate veins with measurable  $^{14}\text{C}$  contents, yielding a mass fraction rate of “serpentinization”  $\sim 10^{-15}/\text{s}$ . Hydration is accompanied by ongoing  $\text{SiO}_2$  addition to all but the most silica rich dunite and harzburgite compositions. We hypothesize that sulfur enrichment at 30 to 150 m depth, is related to ongoing, oxidative leaching of sulfur from the upper 30 m, together with sulfate reduction and sulfide precipitation in an underlying zone of supergene enrichment.

Borehole waters below 200 to 250 m depth, and some mineral assemblages in core, record oxygen fugacity at and approaching the low  $f\text{O}_2$  limit where  $\text{H}_2\text{O}$  forms  $\text{H}_2$ . In Holes BA2A and BA3A, plus older water monitoring well NSHQ14,  $f\text{O}_2$  in water appears to be fixed by a combination of the  $\text{H}_2\text{O}$  to  $\text{H}_2$  reaction itself, together with ongoing oxidation of remaining ferrous iron in serpentine, brucite and olivine. This is intriguing, because discrete sampling of water in the MBO has not yet produced compositions saturated in  $\text{H}_2$  gas, and the origin of  $\text{H}_2$  streaming from some peridotite-hosted alkaline springs elsewhere in the Samail ophiolite is debated.

In water properties logged more than one year after drilling, in Holes BA1A and BA1D, and in logging data from Hole BA4A just a few months after drilling,  $f\text{O}_2$  appears to approach an asymptotic value 3 to 4 log units above the  $\text{H}_2\text{O}$ - $\text{H}_2$  limit. We hypothesize that this is due to equilibria involving cronstedtite  $((\text{Mg},\text{Fe}^{2+})_2\text{Fe}^{3+}\text{SiFe}^{3+}\text{O}_5(\text{OH})_4)$ , chrysotile  $((\text{Mg},\text{Fe}^{2+})_3\text{Si}_2\text{O}_5(\text{OH})_4)$ , and brucite  $(\text{Mg},\text{Fe}^{2+})(\text{OH})_2$ , with cronstedtite compositions close to the Mg-endmember  $\text{Mg}_2\text{Fe}^{3+}\text{SiFe}^{3+}\text{O}_5(\text{OH})_4$  due to the high molar ratio of  $\text{Mg}/(\text{Mg}+\text{Fe}^{2+})$  in the rocks, in turn related to extensive iron oxidation. This mineral assemblage,  $\pm$  the minor phase andradite which is commonly intergrown with serpentine in drill core, may control the limited range of pH (10-11.3) and dissolved  $\text{SiO}_2$  observed in waters from the MBO below 200 to 250 meters depth, and in peridotite-hosted alkaline springs throughout the Samail ophiolite.

Despite all of these indications of ongoing interaction between borehole water and surrounding rocks, including the inference that fluid-mineral equilibria may be controlling the present-day composition of water in the peridotite-hosted aquifer at the MBO, there are many striking indicators of “disequilibrium” in the core. Especially in Hole BA1B, where logging a few months after drilling revealed a gradient in the pH and  $f\text{O}_2$  extending downward for 400 meters, borehole waters are more oxidized than recorded by key minerals and mineral assemblages in core. On a much smaller spatial scale, Ellison et al. [2021] showed that the ferric to total iron ratios in serpentine was highly variable and correlated with texture at the microscale. Similarly, as shown by de Obeso and Kelemen [2020], some peridotite outcrops elsewhere in the Samail ophiolite preserve almost the entire range of  $f\text{O}_2$  on Earth, over a length scale  $\sim 10$  cm, from native metals and highly reduced sulfides in dark serpentinites to rusty orange, clay-bearing assemblages in which all iron is ferric. These different micro-environments

record very different oxidation states which could all be present in peridotite-hosted aquifers at the same time, juxtaposed on short length scales.

It is likely that many of these variations are correlated with texture, in which reduced, low SiO<sub>2</sub> assemblages in mesh cores that record very low water/rock ratios are juxtaposed with adjacent veins recording much higher ratios as reported in core from Hole BA3A by Ellison et al. [2021], and by other workers for outcrop samples and drill core worldwide [e.g., *Bach et al.*, 2004; *Bach et al.*, 2006; *J.S. Beard et al.*, 2009; *Frost et al.*, 2013]. Of course, there are exceptions. Ellison et al. also reported that in samples from above 100 m depth in BA3A, mesh cores generally contained serpentine instead of brucite, and that the latest serpentine veins were more reduced. These observations likely reflect multiple levels of reaction progress (multiple water/rock ratios) and multiple controls on Fe oxidation state in serpentine.

Despite the observed local variability described in the last two paragraphs, overall, on the basis of observed gradients in bulk rock alteration with depth, we infer that the proportion of reduced mesh cores vs relatively oxidized veins increases with depth, and that the difference in  $fO_2$  recorded in cores and veins decreases with depth. Moreover, we suggest that most of the diverse mineral assemblages observed in core could have formed concurrently, at a close approach to equilibrium, on time scales ~ 10,000 years, and indeed that most of these assemblages are continuing to form today.

In general, we hope this paper will be viewed as a starting point, for discussion, and more importantly for continued investigation. Most of the core is intact, and most of the boreholes remain open, for continuing research.

## 6. Author contributions

Peter Kelemen wrote most of the manuscript, asked James Leong and others a lot of questions, and developed some ideas on the genesis and evolution of peridotite protoliths, changes in bulk rock composition due to alteration, and – with Leong – fluid-mineral controls on  $fO_2$ , aSiO<sub>2</sub>, pH and other parameters. Leong led the team in thermodynamic calculations and modeling, and tried to educate Kelemen, while Juan Carlos de Obeso conducted microprobe analyses of serpentine and minor phases including chlorite, andradite and grossular, and performed X-Ray diffraction, carbon, oxygen and strontium isotope analyses of carbonate vein samples. Jürg Matter led the borehole logging effort, and has generously provided the entire OmanDP Science Team with access to the resulting data. Eric Ellison, assisted by Dan Nothaft, provided valuable input on calculation of  $fO_2$  from Eh, pH, temperature and pressure data for observed borehole waters, and  $fO_2$  for the corresponding limit where H<sub>2</sub>O is reduced to form H<sub>2</sub> at a given temperature and pressure, together with the uncertainty in these values. Alexis Templeton and Benjamin Malvoisin, together with Ellison, shared preprints and ideas, in essential discussions that helped frame the questions asked, and the tentative answers provided, in this paper. Compositions of borehole and spring water samples were compiled by Leong et al. (2021), but of course we are greatly indebted to all those who actually gathered and analyzed those samples, via borehole sampling led by Templeton, Nothaft and Ellison, among others. As always, Marguerite Godard ensured the high quality of geochemical data collected onboard DV Chikyu. Matter was ably assisted in downhole logging of Eh, pH, temperature, pressure and depth in borehole waters by Philippe Pézard and his research team. Jude Coggon and Nehal Warsi supervised 100% of core recovery operations. Coggon was also essential as Project Manager throughout the duration of OmanDP and beyond, recalibrating the XRF data and editing the Proceedings chapters long after the money was gone. Coggon and Saebyul Choe were staff scientists, while Godard, Kelemen, Katsu Michibayashi, Eiichi Takazawa and Damon Teagle were co-Chief Scientists onboard DV Chikyu during the monthlong description of 1 km of core from Holes BA1B, BA3A and BA4A. Kelemen, Matter and Teagle were co-PI's of the ICDP Oman Drilling Project, and Zaher Sulaimani was In-Country Project Manager.

## 7. Acknowledgements

The results and ideas in this paper rely heavily on all the hard work and deep thinking of the shipboard scientific team onboard DV Chikyu, together with the many, many volunteers who worked

at the drill sites and helped with the logging. In case you you have not noticed, you are all listed at <http://publications.iodp.org/other/Oman/OmanDP.html> . Drilling and research in the Oman Drilling Project were supported by the Alfred P. Sloan Foundation (in association with the Deep Carbon Observatory, DCO), the International Continental scientific Drilling Program (ICDP), US National Science Foundation (NSF) Research Grant NSF-EAR-1516300, the Japanese Marine Science and Technology Center (JAMSTEC), grant number 16H06347 from the Japanese Society for the Promotion of Science (JSPS), the US National Aeronautics and Space Administration (NASA), including the Rock Powered Life NASA Astrobiology Institute (NNA15BB02A), the European Science Foundation, the German Science Foundation, the Swiss Science Foundation, and the International Ocean Discovery Program (aka International Ocean Drilling Program, IODP), with contributions from the Sultanate of Oman Ministry of Regional Municipalities and Water Resources, the Oman Public Authority of Mining, Sultan Qaboos University, CNRS-Univ. Montpellier, Columbia University of New York, and the University of Southampton. Kelemen's research was also supported with funds from the Arthur D. Storke Chair at Columbia University.

In addition to the authors of this paper, and the drill site and shipboard science teams, a huge group contributed to the success of OmanDP. In Oman, a Project Supervisory Committee chaired by Dr. Said Al Habsi (Director General of Water Resources Assessment in the Ministry of Regional Municipalities and Water Resources, MRMWR), and including Prof. Sobhi Nasir at Sultan Qaboos University, Dr. Ali Al Rajhi, Director of the Geological Survey of Oman, and others, ensured that the project went forward smoothly in accordance with Omani requirements. Members of MRMWR, particularly Ali Al Shukali, ably assisted with downhole logging operations. At Petroleum Development Oman (PDO), Dr. Hamad Shuaili and Dr. Hisham Siyabi kindly facilitated storage of the archive half of all OmanDP core. We particularly thank Dr. Jay Miller and Dr. Brad Clement at IODP TAMU for making the online proceedings volume possible, and Shana Lewis, Rhonda Kappler, Jean Wulfson, Phil Rumford, Lorri Peters, Crystal Wolfe and Kenneth Sherar at IODP TAMU for editorial assistance in preparing the Proceedings of the Oman Drilling Project, more or less following IODP protocols in presenting the results of this decidedly non-standard ICDP project. We thank the technical staff onboard DV Chikyu for fantastic, efficient support and advice over four months in summers 2017 and 2018, especially Lena Maeda, Dr. Yusuke Kubo, and Dr. Chiaki Igarashi. Dr. Nobu Eguchi served as a patient, generous liaison between OmanDP, NSF and JAMSTEC. Core description onboard DV Chikyu would have been impossible without proactive support from JAMSTEC President Asahiko Taira and NSF Program Director Leonard Johnson. Similarly, we received essential assistance with borehole permitting from Professor Ali Al Bemani, Vice Chancellor of Sultan Qaboos University. On a different timescale, we are deeply indebted to His Majesty Sultan Qaboos bin Said Al Said for his open-door policy for scientific research in Oman, and to Professors Françoise Boudier, Bob Coleman, Cliff Hopson and Adolphe Nicolas for establishing the framework for modern studies of the Samail ophiolite. More recently, we thank a host of colleagues – especially Frieder Klein, Ron Frost and Everett Shock – for helpful discussions and scientific input, particularly via a flurry of emails during the last few days prior to completion of the first submitted version.

Finally, we thank Ben Tutolo and Ron Frost for detailed, authoritative, constructive reviews that helped to improve this manuscript.

**Data availability:** The data in this paper (Supplementary Tables S1 through S4) have been uploaded to the Zenodo repository where they are available via Open Access at (<https://zenodo.org/record/5717483#.YZr6dtbMJcs> ).

## 8. References cited

- Abily, B., and G. Ceuleneer (2013), The dunitic mantle-crust transition zone in the Oman ophiolite: Residue of melt-rock interaction, cumulates from high-MgO melts, or both?, *Geology*, *41*, 67-70.
- Abramoff, M. D., P. J. Magalhães, and S. J. Ram (2004), Image processing with Image J, *Biophotonics international*, *11*, 36-42.
- Aharonov, E., J. A. Whitehead, P. B. Kelemen, and M. Spiegelman (1995), Channeling instability of upwelling melt in the mantle, *J. Geophys. Res.*, *100*, 20,433-420,450.
- Al Khirbash, S. (2015), Genesis and mineralogical classification of Ni-laterites, Oman Mountains, *Ore Geol. Reviews*, *65*, 199-212.
- Al Khirbash, S. A. (2016), Geology, mineralogy, and geochemistry of low grade Ni-lateritic soil (Oman Mountains, Oman), *Geochemistry*, *76*, 363-381.

- Al Khirbash, S. A. (2020), Mineralogical characterization of low-grade nickel laterites from the North Oman Mountains: Using mineral liberation analyses–Scanning electron microscopy-based automated quantitative mineralogy, *Ore Geol. Reviews*, *120*, 103429.
- Alabaster, T., J. A. Pearce, and J. Malpas (1982), The volcanic stratigraphy and petrogenesis of the Oman ophiolite complex, *Contrib. Mineral. Petrol.*, *81*, 168-183.
- Alsharan, A. S., and S. J. Y. Nasir (1996), Sedimentological and geochemical interpretation of a transgressive sequence: the Late Cretaceous Oahlah Formation in the western Oman Mountains, United Arab Emirates, *Sedimentary Geol.*, *101*, 227-242.
- Alt, J. C., and W. Bach (2001), Data report: Low-grade hydrothermal alteration of uplifted lower oceanic crust, Hole 735B: mineralogy and isotope geochemistry, *Proc. ODP, Sci. Results*, *176*.
- Alt, J. C., E. M. Schwarzenbach, G. L. Früh-Green, W. C. Shanks III, S. M. Bernasconi, C. J. Garrido, L. Crispini, L. Gaggero, J. A. Padrón-Navarta, and C. Marchesi (2013), The role of serpentinites in cycling of carbon and sulfur: seafloor serpentinization and subduction metamorphism, *Lithos*, *178*, 40-54.
- Alt, J. C., and W. C. Shanks III (2003), Serpentinization of abyssal peridotites from the MARK area, Mid-Atlantic Ridge: Sulfur geochemistry and reaction modeling, *Geochim. Cosmochim. Acta*, *67*, 641-653.
- Alt, J. C., W. C. Shanks III, L. Crispini, L. Gaggero, E. M. Schwarzenbach, G. L. Früh-Green, and S. M. Bernasconi (2012), Uptake of carbon and sulfur during seafloor serpentinization and the effects of subduction metamorphism in Ligurian peridotites, *Chem. Geol.*, *322-323*, 268-277.
- Anderson, G. M. (2017), *Thermodynamics of Natural Systems: Theory and Applications in Geochemistry and Environmental Science 3rd Edition*, Cambridge University Press, Cambridge, UK.
- Andreani, M., M. Muñoz, C. Marcaillou, and A. Delacour (2013),  $\mu$ XANES study of iron redox state in serpentine during oceanic serpentinization, *Lithos*, *178*, 70-83.
- Andrews, J. E., M. G. Stamatakis, I. Mitsis, T. Donnelly, M. R. González-Barros, and A. E. Fallick (2018), Stable isotope evidence for near-surface, low-temperature formation of Mg-(hydro) carbonates in highly altered Greek Mesozoic serpentinites, *J. Geol. Soc.*, *175*, 361-375.
- Arai, S., K. Kadoshima, and T. Morishita (2006), Widespread arc-related melting in the mantle section of the northern Oman ophiolite as inferred from detrital chromian spinels, *J. Geol. Soc. London*, *163*, 869-879.
- Arai, S., and K. Matsukage (1996), Petrology of gabbro-troctolite-peridotite complex from Hess Deep, equatorial Pacific: implications for mantle-melt interaction within the oceanic lithosphere, *Proc. ODP, Sci. Results*, *147*, 135-155.
- Arcilla, C. A., C. S. Pascua, and W. R. Alexander (2011), Hyperalkaline groundwaters and tectonism in the Philippines: significance to natural Carbon Capture and Sequestration, *Energy Procedia*, *4*, 5093-5101.
- Asimow, P. D. (1999), A model that reconciles major- and trace-element data from abyssal peridotites, *Earth Planet Sci. Lett.*, *169*, 303-319.
- Bach, W., C. J. Garrido, H. Paulick, J. Harvey, and M. Rosner (2004), Seawater-peridotite interactions: First insights from ODP Leg 209, MAR 15 N, *G-cubed*, *5*.
- Bach, W., H. Paulick, C. J. Garrido, B. Ildefonse, W. P. Meurer, and S. E. Humphris (2006), Unraveling the sequence of serpentinization reactions: petrography, mineral chemistry, and petrophysics of serpentinites from MAR 15°N (ODP Leg 209, Site 1274), *Geophys. Res. Lett.*, *33*, L13306.
- Bailey, E. H. (1981), Geologic map of Muscat-Ibra area, Sultanate of Oman, *J. Geophys. Res.*, *86*, pocket map.
- Baker, M. B., and J. R. Beckett (1999), The origin of abyssal peridotites: a reinterpretation of constraints based on primary bulk compositions, *Earth Planet Sci. Lett.*, *171*, 49-61.
- Barnes, I., and J. R. O'Neil (1969), Relationship between fluids in some fresh alpine-type ultramafics and possible modern serpentinization, western United States, *GSA Bull.*, *80*(10), 1947-1960.
- Barnes, I., J. R. O'Neil, and J. J. Trescases (1978), Present day serpentinization in New Caledonia, Oman and Yugoslavia., *Geochim. Cosmochim. Acta*, *42*, 144-145.
- Basch, V., E. Rampone, L. Crispini, C. Ferrando, B. Ildefonse, and M. Godard (2018), From mantle peridotites to hybrid troctolites: Textural and chemical evolution during melt-rock interaction history (Mt. Maggiore, Corsica, France), *Lithos*, *323*, 4-23.
- Basch, V., E. Rampone, L. Crispini, C. Ferrando, B. Ildefonse, and M. Godard (2019), Multi-stage reactive formation of troctolites in slow-spreading oceanic lithosphere (Erro–Tobbio, Italy): a combined field and petrochemical study, *Journal of Petrology*, *60*, 873-906.
- Beard, J. S. (2000), Occurrence and composition of tochilinite and related minerals in Site 1068 serpentinites, *Proc. ODP, Sci. Res.*, *173*, 1-9.



- Beard, J. S., B. R. Frost, P. Fryer, A. McCaig, R. Searle, B. Ildefonse, P. Zinin, and S. K. Sharma (2009), Onset and progression of serpentinization and magnetite formation in olivine-rich troctolite from IODP Hole U1309D, *Journal of Petrology*, *50*, 387-403.
- Beard, J. S., and L. J. Hopkinson (2000), A fossil, serpentinization-related hydrothermal vent, Ocean Drilling Program Leg 173, Site 1068 (Iberia Abyssal Plain): Some aspects of mineral and fluid chemistry, *J. Geophys. Res.*, *105*, 16,527-516,539.
- Beinlich, A., H. Austrheim, J. Glodny, M. Erambert, and T. B. Andersen (2010), CO<sub>2</sub> sequestration and extreme Mg depletion in serpentinized peridotite clasts from the Devonian Solund basin, SW-Norway, *Geochim. Cosmochim. Acta*, *74*, 6935-6964.
- Benoit, M., G. Ceuleneer, and M. Polvé (1999), The remelting of hydrothermally altered peridotite at mid-ocean ridges by intruding mantle diapirs, *Nature*, *402*, 514-518.
- Benoit, M., M. Polvé, and G. Ceuleneer (1996), Trace element and isotopic characterization of mafic cumulates in a fossil mantle diapir (Oman ophiolite), *Chem. Geol.*, *199*, 199-214.
- Berndt, M. E., D. E. Allen, and W. E. Seyfried Jr (1996), Reduction of CO<sub>2</sub> during serpentinization of olivine at 300 C and 500 bar, *Geology*, *24*, 351-354.
- Berner, E. K., and R. A. Berner (2012), *Global Environment: Water, Air, and Geochemical Cycles*, Princeton University Press, Princeton NJ.
- Bethke, C. M. (1998), *The geochemist's workbench. Users Guide*, 184 pp.
- Bieseler, B., A. Diehl, N. Jöns, F. Lucassen, and W. Bach (2018), Constraints on cooling of the lower ocean crust from epidote veins in the Wadi Gideah section, Oman Ophiolite, *G-cubed*, *19*, 4195-4217.
- Bodinier, J.-L., and M. Godard (2003), Orogenic, ophiolitic, and abyssal peridotites, in *Treatise on Geochemistry, Volume 2*, edited by R. Carlson, Elsevier, Amsterdam.
- Bodinier, J. L. (1988), Geochemistry and petrogenesis of the Lanzo peridotite body, western Alps, *Tectonophysics*, *49*, 67-88.
- Bosch, D., M. Jamais, F. Boudier, A. Nicolas, J.-M. Dautria, and P. Agrinier (2004), Deep and high-temperature hydrothermal circulation in the Oman ophiolite: Petrological and Isotopic evidence, *Journal of Petrology*, *45*, 1181-1208.
- Botto, R. I., and G. H. Morrison (1976), Josephinite: A unique nickel-iron, *Am. J. Sci.*, *276*, 24-274.
- Boudier, F., A. Baronnet, and D. Mainprice (2010), Serpentine mineral replacements of natural olivine and their seismic implications: Oceanic lizardite versus subduction-related antigorite, *Journal of Petrology*, *51*, 495-512.
- Boudier, F., G. Ceuleneer, and A. Nicolas (1988), Shear zones, thrusts and related magmatism in the Oman ophiolite: Initiation of thrusting on an oceanic ridge, *Tectonophysics*, *151*, 275-296.
- Boudier, F., and R. G. Coleman (1981), Cross section through the peridotite in the Semail ophiolite, *J. Geophys. Res.*, *86*, 2573-2592.
- Boudier, F., A. Nicolas, and B. Ildefonse (1996), Magma chambers in the Oman ophiolite: Fed from the top and the bottom, *Earth Planet Sci. Lett.*, *144*, 239-250.
- Boulart, C., V. Chavagnac, C. Monnin, A. Delacourt, G. Ceuleneer, and G. Hoareau (2013), Difference in gas venting from ultramafic-hosted warm springs: the example of Oman and Voltri ophiolites, *Ophioliti*, *38*, 143-156.
- Boyd, E. S., M. A. Amenabar, S. Poudel, and A. S. Templeton (2020), Bioenergetic constraints on the origin of autotrophic life, *Phil. Trans. Roy. Soc. London*, *A378*, 20190151.
- Bratsch, S. G. (1989), Standard Electrode Potentials and Temperature Coefficients in Water at 298.15 K., *J. Physical & Chemical Reference Data*, *18*, 1-21. <https://doi.org/10.1063/1.555839>
- Braun, M. G., and P. B. Kelemen (2002), Dunite distribution in the Oman ophiolite: Implications for melt flux through porous dunite conduits, *G-cubed*, *3*.
- Brunelli, D., M. Seyler, A. Cipriani, L. Ottolini, and E. Bonatti (2006), Discontinuous melt extraction and weak refertilization of mantle peridotites at the Vema lithospheric section (Mid-Atlantic Ridge), *Journal of Petrology*, *47*, 745-771.
- Bruni, J., M. Canepa, G. Chiodini, R. Cioni, F. Cipolli, A. Longinelli, L. Marini, G. Ottonello, and M. V. Zuccolini (2002), Irreversible water-rock mass transfer accompanying the generation of the neutral, Mg-HCO<sub>3</sub> and high-pH, Ca-OH spring waters of the Genova province, Italy, *Applied Geochem.*, *17*(4), 455-474.
- Cacciamani, G., A. Dinsdale, M. Palumbo, and A. Pasturel (2010), The Fe-Ni system: Thermodynamic modelling assisted by atomistic calculations, *Intermetallics*, *18*, 1148-1162.
- Canovas, P. A., T. Hoehler, and E. L. Shock (2017), Geochemical bioenergetics during low-temperature serpentinization: An example from the Semail ophiolite, Sultanate of Oman, *J. Geophys. Res. Biogeosci.*, *122*, 1821-1847.

- Ceuleneer, G., M. Monnereau, and I. Amri (1996), Thermal structure of a fossil mantle diapir inferred from the distribution of mafic cumulates, *Nature*, *379*, 149-153.
- Chacko, T., and P. Deines (2008), Theoretical calculation of oxygen isotope fractionation factors in carbonate systems, *Geochim. Cosmochim. Acta*, *72*, 3642-3660.
- Chavagnac, V., G. Ceuleneer, C. Monnin, B. Lansac, G. Hoareau, and C. Boulart (2013a), Mineralogical assemblages forming at hyperalkaline warm springs hosted on ultramafic rocks: a case study of Oman and Ligurian ophiolites, *G-cubed*, *14*, 2474-2495.
- Chavagnac, V., C. Monnin, G. Ceuleneer, C. Boulart, and G. Hoareau (2013b), Characterization of hyperalkaline fluids produced by low-temperature serpentinization of mantle peridotites in the Oman and Ligurian ophiolites, *G-cubed*, *14*, 2496-2522.
- Clark, I. D., and J.-C. Fontes (1990), Paleoclimatic reconstruction in northern Oman based on carbonates from hyperalkaline groundwaters, *Quat. Res.*, *33*, 320-336.
- Coleman, R. G., and C. A. Hopson (Eds.) (1981), *Oman Ophiolite Special Issue, J. Geophys. Res.*, 2495-2782 pp.
- Collier, M. L., and P. B. Kelemen (2010), The Case for Reactive Crystallization at Mid-Ocean Ridges, *J. Petrol.*, *51*, 1913-1940, doi:10.1093/petrology/egg043.
- Coogan, L. A., K. A. Howard, K. M. Gillis, M. J. Bickle, H. Chapman, A. J. Boyce, G. R. T. Jenkin, and R. N. Wilson (2006), Chemical and thermal constraints on focussed fluid flow in the lower oceanic crust, *Am. J. Sci.*, *306*, 389-427.
- Cowan, R. J., M. P. Searle, and D. J. Waters (2014), Structure of the metamorphic sole to the Oman Ophiolite, Sumeini Window and Wadi Tayyin: implications for ophiolite obduction processes, *Geol. Soc. London Spec. Pub.*, *392*, 155-175.
- Currin, A., P. E. Wolff, J. Koepke, R. R. Almeev, C. Zhang, B. Zihlmann, B. Ildefonse, and D. A. H. Teagle (2018), Chlorine-rich amphibole in deep layered gabbros as evidence for brine/rock interaction in the lower oceanic crust: A case study from the Wadi Wariyah, Samail Ophiolite, Sultanate of Oman, *Lithos*, *323*, 125-136.
- de Obeso, J. C., and P. B. Kelemen (2018), Fluid rock interactions in residual mantle peridotites overlain by shallow oceanic limestones: Insights from Wadi Fins, Sultanate of Oman, *Chem. Geol.*, *498*, 139-149.
- de Obeso, J. C., and P. B. Kelemen (2020), Magnesium and iron mobility during serpentinization, oxidation and weathering of mantle peridotite at low temperatures: The case of Wadi Fins, *Phil. Trans. Roy. Soc. London*, *A378*, 20180433.
- de Obeso, J. C., D. Santiago Ramos, J. Higgins, and P. Kelemen (2021), A Mg isotopic perspective on the mobility of magnesium during serpentinization and carbonation of the Oman ophiolite, *J. Geophys. Res.*, *126*, e2020JB020237.
- del Real, P. G., K. Maher, T. Kluge, D. K. Bird, G. E. Brown Jr, and C. M. John (2016), Clumped-isotope thermometry of magnesium carbonates in ultramafic rocks, *Geochim. Cosmochim. Acta*, *193*, 222-250.
- Dewandel, B., F. Boudier, H. Kern, W. Warsi, and D. Mainprice (2003), Seismic wave velocity and anisotropy of serpentinized peridotite in the Oman ophiolite, *Tectonophysics*, *370*, 77-94.
- Dewandel, B., P. Lachassagne, F. Boudier, S. Al-Hattali, B. Ladouche, J.-L. Pinault, and Z. Al-Suleimani (2005), A conceptual hydrogeological model of ophiolite hard-rock aquifers in Oman based on a multiscale and a multidisciplinary approach, *Hydrogeology J.*, *13*, 708-726.
- Dewandel, B., P. Lachassagne, and A. Qatan (2004), Spatial measurements of stream baseflow, a relevant method for aquifer characterization and permeability evaluation: Application to a hard-rock aquifer, the Oman ophiolite, *Hydrol. Process.*, *18*, 3391-3400.
- Dick, H., and T. Bullen (1984), Chromian spinel as a petrogenetic indicator in abyssal and alpine-type peridotites and spatially associated lavas, *Contrib. Mineral. Petrol.*, *86*, 54-76.
- Dick, H. J., and J. H. Natland (1996), Late-stage melt evolution and transport in the shallow mantle beneath the East Pacific Rise, *Proc. ODP, Sci. Res.*, *147*, 103-134.
- Drouin, M., M. Godard, B. Ildefonse, O. Bruguier, and C. J. Garrido (2009), Geochemical and petrographic evidence for magmatic impregnation in the oceanic lithosphere at Atlantis Massif, Mid-Atlantic Ridge (IODP Hole U1309D, 30 N), *Chem. Geol.*, *264*, 71-88.
- Drouin, M., B. Ildefonse, and M. Godard (2010), A microstructural imprint of melt impregnation in slow spreading lithosphere: Olivine-rich troctolites from the Atlantis Massif, Mid-Atlantic Ridge, 30 N, IODP Hole U1309D, *G-cubed*, *11*.
- Edwards, C. S., and B. L. Ehlmann (2015), Carbon sequestration on Mars, *Geology*, *43*, 863-866.
- Ehlmann, B. L., and C. S. Edwards (2014), Mineralogy of the Martian surface, *Ann. Rev. Earth Planet. Sci.*, *42*, 291-315.

- Ehlmann, B. L., J. F. Mustard, and S. L. Murchie (2010), Geologic setting of serpentine deposits on Mars, *Geophys. Res. Lett.*, *37*, L06201.
- Ehlmann, B. L., et al. (2008), Orbital identification of carbonate-bearing rocks on Mars, *Science*, *322*, 1828-1832.
- Ehlmann, B. L., et al. (2009), Identification of hydrated silicate minerals on Mars using MRO-CRISM: Geologic context near Nili Fossae and implications for aqueous alteration, *J. Geophys. Res.*, *114*, E00D08.
- El Dien, H. G., S. Arai, L. S. Doucet, Z. X. Li, Y. Kil, D. Fougereuse, S. M. Reddy, D. W. Saxey, and M. Hamdy (2019), Cr-spinel records metasomatism not petrogenesis of mantle rocks, *Nature Communications*, *10*, 1-12.
- Ellison, E. T., A. S. Templeton, S. D. Zeigler, L. E. Mayhew, P. B. Kelemen, J. M. Matter, and Oman Drilling Project Science Party (2021), Low-Temperature Hydrogen Formation During Aqueous Alteration of Serpentinized Peridotite in the Samail Ophiolite, *J. Geophys. Res.*, *126*, e2021JB021981.
- Eslami, A., B. Tutolo, K. Evans, W.-A. Kahl, M. Godard, P. Kelemen, K. Michibayashi, E. Takazawa, D. Teagle, and Oman Drilling Project Phase 2 Science Party (2018), A Reconnaissance Petrographic Study of Opaque Mineral Assemblages in Peridotites and Mafic Dykes from the Oman Drilling Project Holes BA1B, BA3A and BA4A, *AGU Fall Meeting Abstracts*, V23H-2920.
- Etiopie, G., B. L. Ehlmann, and M. Schoell (2013), Low temperature production and exhalation of methane from serpentinized rocks on Earth: a potential analog for methane production on Mars, *Icarus*, *224*, 276-285.
- Evans, B. W. (2004), The serpentinite multisystem revisited: chrysotile is metastable, *Int. Geol. Rev.*, *46*, 479-506.
- Evans, K. A., R. Powell, and B. R. Frost (2013), Using equilibrium thermodynamics in the study of metasomatic alteration, illustrated by an application to serpentinites, *Lithos*, *168*, 67-84.
- Evans, O., M. W. Spiegelman, and P. B. Kelemen (2018), A poroelastic model of serpentinization: Exploring the interplay between rheology, surface energy, reaction and fluid flow, *J. Geophys. Res.*, *123*, 8653–8675.
- Evans, O., M. W. Spiegelman, and P. B. Kelemen (2020), Phase-field modeling of reaction-driven cracking: Determining conditions for extensive olivine serpentinization, *J. Geophys. Res.*, *125*, e2019JB018614.
- Falk, E. S., W. Guo, A. N. Paukert, J. M. Matter, E. M. Mervine, and P. B. Kelemen (2016), Controls on the stable isotope compositions of travertine from hyperalkaline springs in Oman: Insights from clumped isotope measurements, *Geochim. Cosmochim. Acta*, *192*, 1-28.
- Falk, E. S., and P. B. Kelemen (2015), Geochemistry and petrology of listvenite in the Oman Ophiolite: Complete carbonation of peridotite during ophiolite emplacement, *Geochim. Cosmochim. Acta*, *160*, 70-90.
- Ferrando, C., M. Godard, B. Ildefonse, and E. Rampone (2018), Melt transport and mantle assimilation at Atlantis Massif (IODP Site U1309): Constraints from geochemical modeling, *Lithos*, *323*, 24-43.
- Fisk, M. R., and S. J. Giovannoni (1999), Sources of nutrients and energy for a deep biosphere on Mars, *J. Geophys. Res.*, *104*, 11805–11815.
- Fones, E. M., D. R. Colman, E. A. Kraus, D. B. Nothaft, S. Poudel, K. R. Rempfert, J. R. Spear, A. S. Templeton, and E. S. Boyd (2019), Physiological adaptations to serpentinization in the Samail Ophiolite, Oman, *ISME Journal*, *13*, 1750-1762.
- Fones, E. M., D. R. Colman, E. A. Kraus, R. Stepanauskas, A. S. Templeton, J. R. Spear, and E. S. Boyd (2021), Diversification of methanogens into hyperalkaline serpentinizing environments through adaptations to minimize oxidant limitation, *ISME Journal*, *15*, 1121-1135.
- Foustoukos, D. I., and W. E. Seyfried (2004), Hydrocarbons in hydrothermal vent fluids: The role of chromium-bearing catalysts, *Science*, *304*, 1002-1005.
- France, L., B. Ildefonse, and J. Koepke (2009), Interactions between magma and hydrothermal system in Oman ophiolite and in IODP Hole 1256D: Fossilization of a dynamic melt lens at fast spreading ridges, *G-cubed*, *10*.
- Frost, B. R. (1985), On the stability of sulfides, oxides, and native metals in serpentinite, *Journal of Petrology*, *26*, 31-63.
- Frost, B. R., and J. S. Beard (2007), On silica activity and serpentinization, *Journal of Petrology*, *48*, 1351–1368.
- Frost, B. R., K. A. Evans, S. M. Swapp, J. S. Beard, and F. E. Mothersole (2013), The process of serpentinization in dunite from New Caledonia, *Lithos*, *178*, 24-39.

- Gahlan, H. A., M. K. Azer, P. D. Asimow, and K. M. Al-Kahtany (2020), Genesis and geodynamic evolution of serpentinized ultramafics and associated magnesite deposits in the Al-Wask ophiolite, Arabian Shield, Saudi Arabia, *Am. J. Sci.*, **320**, 236-279.
- Garrido, C.-J., P. B. Kelemen, and G. Hirth (2001), Variation of cooling rate with depth in lower crust formed at an oceanic spreading ridge: Plagioclase crystal size distributions in gabbros from the Oman ophiolite, *G-cubed*, **2**, 2000GC000136.
- Giampouras, M., C. J. Garrido, W. Bach, C. Los, D. Fussmann, P. Monien, and J. M. García-Ruiz (2020), On the controls of mineral assemblages and textures in alkaline springs, Samail Ophiolite, Oman, *Chem. Geol.*, **533**, 119435.
- Gillis, K. M., et al. (2014), Primitive layered gabbros from fast-spreading lower oceanic crust, *Nature*, **505**, 204-207.
- Glombitza, C., L. I. Putnam, K. R. Rempfert, M. D. Kubo, M. O. Schrenk, A. S. Templeton, and T. M. Hoehler (2021), Active microbial sulfate reduction in serpentinizing fluids of the continental subsurface, *Communications Earth and Environment*, **2**, 84.
- Godard, M., et al. (2009), Geochemistry of a long in-situ section of intrusive slow-spread oceanic lithosphere: Results from IODP Site U1309 (Atlantis Massif, 30 N Mid-Atlantic-Ridge), *Earth Planet Sci. Lett.*, **279**, 110-122.
- Godard, M., D. Joussetin, and J.-L. Bodinier (2000), Relationships between geochemistry and structure beneath a palaeo-spreading centre: A study of the mantle section in the Oman ophiolite, *Earth Planet. Sci. Lett.*, **180**, 133-148.
- Hacker, B. R., and J. L. Mosenfelder (1996), Metamorphism and deformation along the emplacement thrust of the Samail ophiolite, Oman, *Earth Planet Sci. Lett.*, **144**, 435-451.
- Hanghøj, K., P. Kelemen, D. Hassler, and M. Godard (2010), Composition and genesis of depleted mantle peridotites from the Wadi Tayin massif, Oman ophiolite; Major and trace element geochemistry, and Os isotope and PGE systematics, *Journal of Petrology*, **51**, 201-227.
- Hansman, R. J., U. Ring, S. N. Thomson, B. den Brok, and K. Stübner (2017), Late Eocene uplift of the Al Hajar Mountains, Oman, supported by stratigraphy and low-temperature thermochronology, *Tectonics*, **36**, 3081-3109.
- Hao, J., D. A. Sverjensky, and R. M. Hazen (2017), A model for late Archean chemical weathering and world average river water, *Earth Planet Sci. Lett.*, **476**, 191-203.
- Helgeson, H. C., J. M. Delany, H. W. Nesbitt, and D. K. Bird (1978), Summary and critique of the thermodynamic behavior of aqueous electrolytes at high pressure and temperature, *Am. J. Sci.*, **787**, 1-229.
- Homburg, J., G. Hirth, and P. B. Kelemen (2010), Investigation of the strength contrast at the Moho: A case study from the Oman Ophiolite, *Geology*, **38**, 679-682.
- Hopkinson, L. J., S. Dee, and C. A. Boulter (2000), Moving reactive interfaces and fractal carbonate replacement patterns in serpentinites: evidence from the southern Iberia Abyssal Plain, *Min. Mag.*, **64**, 791-800.
- Horita, J., and M. E. Berndt (1999), Abiogenic methane formation and isotopic fractionation under hydrothermal conditions, *Science*, **285**, 1055-1057.
- Howald, R. A. (2003), The Thermodynamics of Tetrataenite and Awaruite: A Review of the Fe-Ni Phase Diagram, *Metallurgical & Materials Transactions 34A*, 1759-1769.
- Iyer, K., B. Jamtveit, J. Mathiesen, A. Malthe-Sorensen, and J. Feder (2008), Reaction-assisted hierarchical fracturing during serpentinization, *Earth Planet. Sci. Lett.*, **267**, 503-516.
- Jagoutz, E., H. Palme, H. Baddenhausen, K. Blum, M. Cendales, G. Dreibus, and H. Wanke (1979), The abundances of major, minor and trace elements in the earth's mantle as derived from primitive ultramafic nodules, *Proc. Lunar & Planetary Sci. Conf.*, **10**, 2031-2050.
- Jamtveit, B., C. Putnis, and A. Malthe-Sorensen (2009), Reaction induced fracturing during replacement processes, *Contrib. Mineral. Petrol.*, **157**, 127-133.
- Johnson, J. W., E. H. Oelkers, and H. C. Helgeson (1992), SUPCRT92 - A software package for calculating the standard molal thermodynamic properties of minerals, gases, aqueous species, and reactions from 1-bar to 5000-bar and 0C to 1000C, *Computers and Geosciences* **18**, 899-947.
- Katayama, I., et al. (2020), Permeability profiles across the crust-mantle sections in the Oman Drilling Project inferred from dry and wet resistivity data, *J. Geophys. Res.*, **125**, e2019JB018698.
- Katayama, I., N. Abe, K. Okazaki, K. Hatakeyama, Y. Akamatsu, K. Michibayashi, M. Godard, P. Kelemen, and Oman Drilling Project Phase 2 Science Party (2021), Crack geometry of serpentinized peridotites inferred from onboard ultrasonic data from the Oman Drilling Project, *Tectonophysics*, *in press*.
- Kelemen, P. B. (1986), Assimilation of ultramafic rock in subduction-related magmatic arcs, *J. Geol.*, **94**, 829-843.



- Kelemen, P. B. (1990), Reaction between ultramafic wall rock and fractionating basaltic magma: Part I, Phase relations, the origin of calc-alkaline magma series, and the formation of discordant dunite, *Journal of Petrology*, 31, 51-89.
- Kelemen, P. B., and E. Aharonov (1998), Periodic formation of magma fractures and generation of layered gabbros in the lower Crust beneath oceanic spreading ridges, *Geophysical Monograph*, 106, 267-289.
- Kelemen, P. B., M. Braun, and G. Hirth (2000), Spatial distribution of melt conduits in the mantle beneath oceanic spreading ridges: Observations from the Ingalls and Oman ophiolites, *G-cubed*, 1, doi:10.1029/1999GC000012.
- Kelemen, P. B., O. Evans, M. Ghiorso, J. Mustard, B. L. Ehlmann, and M. Spiegelman (2020a), Carbonate in Olivine-Rich Unit (s) on Mars May Have Formed at Low P (H<sub>2</sub>O), *Lunar & Planetary Science Conference Abstracts*, 1213.
- Kelemen, P. B., and G. Hirth (2012), Reaction-driven cracking during retrograde metamorphism: Olivine hydration and carbonation, *Earth Planet. Sci. Lett.*, 345-348, 81-89.
- Kelemen, P. B., G. Hirth, N. Shimizu, M. Spiegelman, and H. J. B. Dick (1997a), A review of melt migration processes in the adiabatically upwelling mantle beneath oceanic spreading ridges, *Phil. Trans. Roy. Soc. London A*, 355, 283-318.
- Kelemen, P. B., E. Kikawa, D. J. Miller, and et al. (2004), Drilling mantle peridotite along the Mid-Atlantic Ridge from 14 to 16 N, *Proc. ODP, Init. Reports*, 209, [http://www-odp.tamu.edu/publications/209\\_IR/209ir.htm](http://www-odp.tamu.edu/publications/209_IR/209ir.htm).
- Kelemen, P. B., E. Kikawa, D. J. Miller, and Shipboard Scientific Party (2007), Leg 209 summary: Processes in a 20-km-thick conductive boundary layer beneath the Mid-Atlantic Ridge, 14°-16°N, *Proc. ODP, Sci. Results 209*, [http://www-odp.tamu.edu/publications/209\\_SR/synth/synth.htm](http://www-odp.tamu.edu/publications/209_SR/synth/synth.htm), 1-33.
- Kelemen, P. B., K. Koga, and N. Shimizu (1997b), Geochemistry of gabbro sills in the crust-mantle transition zone of the Oman ophiolite: Implications for the origin of the oceanic lower crust, *Earth Planet. Sci. Lett.*, 146(3-4), 475-488.
- Kelemen, P. B., and J. Matter (2008), In situ mineral carbonation in peridotite for CO<sub>2</sub> storage, *Proc. National Acad. Sci. (US)*, 105, 17,295-217,300.
- Kelemen, P. B., J. Matter, E. E. Streit, J. F. Rudge, W. B. Curry, and J. Blusztajn (2011), Rates and mechanisms of mineral carbonation in peridotite: Natural processes and recipes for enhanced, in situ CO<sub>2</sub> capture and storage, *Ann. Rev. Earth Planet. Sci.*, 39, 545-576.
- Kelemen, P. B., J. M. Matter, D. A. H. Teagle, J. A. Coggon, and Oman Drilling Project Science Team (2020b), Introduction to Science Theme 1A: Gabbro traverse, in *Proceedings of the Oman Drilling Project*, edited by P. B. Kelemen, J. M. Matter, D. A. H. Teagle, J. A. Coggon and et al., pp. 1-2, International Ocean Discovery Program, College Station, TX.
- Kelemen, P. B., J. M. Matter, D. A. H. Teagle, J. A. Coggon, and Oman Drilling Project Science Team (2020c), Methods and explanatory notes, in *Proceedings of the Oman Drilling Project*, edited by P. B. Kelemen, J. M. Matter, D. A. H. Teagle, J. A. Coggon and et al., International Ocean Discovery Program, College Station, TX.
- Kelemen, P. B., J. M. Matter, D. A. H. Teagle, J. A. Coggon, and Oman Drilling Project Science Team (2020d), Site GT1: Layered cumulate gabbros and deep fault zones, in *Proceedings of the Oman Drilling Project*, edited by P. B. Kelemen, J. M. Matter, D. A. H. Teagle, J. A. Coggon and et al., pp. 1-120, International Ocean Discovery Program, College Station, TX.
- Kelemen, P. B., J. M. Matter, D. A. H. Teagle, J. A. Coggon, and Oman Drilling Project Science Team (2020e), Site GT2: Foliated to layered gabbro transition, in *Proceedings of the Oman Drilling Project*, edited by P. B. Kelemen, J. M. Matter, D. A. H. Teagle, J. A. Coggon and et al., pp. 1-130, International Ocean Discovery Program, College Station, TX.
- Kelemen, P. B., J. M. Matter, D. A. H. Teagle, J. A. Coggon, and Oman Drilling Project Science Team (2020f), Site GT3: Sheeted dike to gabbro transition, in *Proceedings of the Oman Drilling Project*, edited by P. B. Kelemen, J. M. Matter, D. A. H. Teagle, J. A. Coggon and et al., pp. 1-152, International Ocean Discovery Program, College Station, TX.
- Kelemen, P. B., J. M. Matter, D. A. H. Teagle, J. A. Coggon, and Oman Drilling Project Science Team (2021a), Introduction to Science Theme 1B: Crust-mantle traverse, in *Proceedings of the Oman Drilling Project*, edited by P. B. Kelemen, J. M. Matter, D. A. H. Teagle, J. A. Coggon and et al., pp. 1-6, International Ocean Discovery Program, College Station, TX.
- Kelemen, P. B., J. M. Matter, D. A. H. Teagle, J. A. Coggon, and Oman Drilling Project Science Team (2021b), Introduction to Science Theme 3: Multi-borehole observatory, in *Proceedings of the Oman Drilling Project*, edited by P. B. Kelemen, J. M. Matter, D. A. H. Teagle, J. A. Coggon and et al., pp. 1-9, International Ocean Discovery Program, College Station, TX.

- Kelemen, P. B., J. M. Matter, D. A. H. Teagle, J. A. Coggon, and Oman Drilling Project Science Team (2021c), Microbiology, in *Proceedings of the Oman Drilling Project*, edited by P. B. Kelemen, J. M. Matter, D. A. H. Teagle, J. A. Coggon and et al., pp. 1-13, International Ocean Discovery Program, College Station, TX.
- Kelemen, P. B., J. M. Matter, D. A. H. Teagle, J. A. Coggon, and Oman Drilling Project Science Team (2021d), Site BA1, in *Proceedings of the Oman Drilling Project*, edited by P. B. Kelemen, J. M. Matter, D. A. H. Teagle, J. A. Coggon and et al., pp. 1-105, International Ocean Discovery Program, College Station, TX.
- Kelemen, P. B., J. M. Matter, D. A. H. Teagle, J. A. Coggon, and Oman Drilling Project Science Team (2021e), Site BA2, in *Proceedings of the Oman Drilling Project*, edited by P. B. Kelemen, J. M. Matter, D. A. H. Teagle, J. A. Coggon and et al., pp. 1-6, International Ocean Discovery Program, College Station, TX.
- Kelemen, P. B., J. M. Matter, D. A. H. Teagle, J. A. Coggon, and Oman Drilling Project Science Team (2021f), Site BA3, in *Proceedings of the Oman Drilling Project*, edited by P. B. Kelemen, J. M. Matter, D. A. H. Teagle, J. A. Coggon and et al., pp. 1-90, International Ocean Discovery Program, College Station, TX.
- Kelemen, P. B., J. M. Matter, D. A. H. Teagle, J. A. Coggon, and Oman Drilling Project Science Team (2021g), Site BA4, in *Proceedings of the Oman Drilling Project*, edited by P. B. Kelemen, J. M. Matter, D. A. H. Teagle, J. A. Coggon and et al., pp. 1-97, International Ocean Discovery Program, College Station, TX.
- Kelemen, P. B., J. M. Matter, D. A. H. Teagle, J. A. Coggon, and Oman Drilling Project Science Team (2021h), Site CM1: Layered gabbros, crustal ultramafic rocks, and mantle harzburgite, in *Proceedings of the Oman Drilling Project*, edited by P. B. Kelemen, J. M. Matter, D. A. H. Teagle, J. A. Coggon and et al., pp. 1-145, International Ocean Discovery Program, College Station, TX.
- Kelemen, P. B., J. M. Matter, D. A. H. Teagle, J. A. Coggon, and Oman Drilling Project Science Team (2021i), Site CM2: Crust-mantle transition zone and into upper mantle, in *Proceedings of the Oman Drilling Project*, edited by P. B. Kelemen, J. M. Matter, D. A. H. Teagle, J. A. Coggon and et al., pp. 1-146, International Ocean Discovery Program, College Station, TX.
- Kelemen, P. B., J. M. Matter, D. A. H. Teagle, J. A. Coggon, and O. D. P. S. Team (2020g), *Proceedings of the Oman Drilling Project*, doi:10.14379/Oman.ph1-2.proc.2020., International Ocean Discovery Program, College Station, TX.
- Kelemen, P. B., et al. (2021j), Mass transfer into the leading edge of the mantle wedge: Initial results from Oman Drilling Project Hole BT1B, *J. Geophys. Res.*, *minor revision in progress*, preprint at <https://www.essoar.org/doi/10.1002/essoar.10507370.10507371>.
- Kelemen, P. B., N. Shimizu, and V. J. M. Salters (1995a), Extraction of mid-ocean-ridge basalt from the upwelling mantle by focused flow of melt in dunite channels, *Nature*, *375*, 747-753.
- Kelemen, P. B., J. A. Whitehead, E. Aharonov, and K. Jordahl (1995b), Experiments on flow focusing in soluble porous media, with applications to melt extraction from the mantle, *J. Geophys. Res.*, *100*, 475-496.
- Khedr, M. Z., S. Arai, and M. Python (2013), Petrology and chemistry of basal lherzolites above the metamorphic sole from Wadi Sarami central Oman ophiolite, *J. Mineral. Petrol. Sci.*, *108*, 13-24.
- Khedr, M. Z., S. Arai, M. Python, and A. Tamura (2014), Chemical variations of abyssal peridotites in the central Oman ophiolite: Evidence of oceanic mantle heterogeneity, *Gondwana Res.*, *25*, 1242-1262.
- Klein, F., and W. Bach (2009), Fe–Ni–Co–O–S phase relations in peridotite–seawater interactions, *Journal of Petrology*, *50*, 37-59.
- Klein, F., W. Bach, S. E. Humphris, W. A. Kahl, N. Jöns, B. Moskowicz, and T. S. Berquó (2014), Magnetite in seafloor serpentinite—Some like it hot, *Geology*, *42*, 135-138.
- Klein, F., W. Bach, N. Jöns, T. McCollom, B. Moskowicz, and T. Berquó (2009), Iron partitioning and hydrogen generation during serpentinization of abyssal peridotites from 15 degrees N on the Mid-Atlantic Ridge, *Geochimica Et Cosmochimica Acta*, *73*(22), 6868-6893.
- Klein, F., W. Bach, and T. McCollom (2013), Compositional controls on hydrogen generation during serpentinization of ultramafic rocks, *Lithos*, *178*, 55-69.
- Klein, F., and C.-J. Garrido (2011), Thermodynamic constraints on mineral carbonation of serpentinized peridotite, *Lithos*, *126*, 147-160.
- Klein, F., and V. Le Roux (2020), Quantifying the volume increase and chemical exchange during serpentinization, *Geology*, *48*, 552-556.
- Koga, K., P. B. Kelemen, and N. Shimizu (2001), Petrogenesis of the crust-mantle transition zone (MTZ) and the origin of lower crustal wehrlite in the Oman Ophiolite, *G-cubed*, *2*, 2000GC000132.

- Kohut, E. J., and R. L. Nielsen (2003), Low-pressure phase equilibria of anhydrous anorthite-bearing mafic magmas, *G-cubed*, 4.
- Korenaga, J., and P. B. Kelemen (1997), Origin of gabbro sills in the Moho transition zone of the Oman ophiolite: Implications for magma transport in the oceanic lower crust, *J. Geophys. Res.*, 102, 27729-27749.
- Kraus, E., D. Nothaft, B. Stamps, K. Rempfert, E. Ellison, J. Matter, A. Templeton, E. Boyd, and J. Spear (2021), Molecular evidence for an active microbial methane cycle in serpentinite-hosted groundwaters in the Samail Ophiolite, Oman, *Applied & Environmental Microbiology*, 87, 1-18.
- Lacinska, A. M., and M. T. Styles (2013), Silicified serpentinite—a residuum of a Tertiary palaeo-weathering surface in the United Arab Emirates, *Geol. Mag.*, 150, 385-395.
- Lacinska, A. M., M. T. Styles, and A. R. Farrant (2014), Near-surface diagenesis of ophiolite-derived conglomerates of the Barzaman Formation, United Arab Emirates: a natural analogue for permanent CO<sub>2</sub> sequestration via mineral carbonation of ultramafic rocks, *Geol. Soc. London Spec. Pub.*, 392, 343-360.
- Lamadrid, H. M., Z. Zajacz, F. Klein, and R. J. Bodnar (2021), Synthetic fluid inclusions XXIII. Effect of temperature and fluid composition on rates of serpentinization of olivine, *Geochim. Cosmochim. Acta*, 292, 285-308.
- Lazar, C. (2020), Using silica activity to model redox-dependent fluid compositions in serpentinites from 100–700° C and 1–20 kbar, *Journal of Petrology*, 61, ega101.
- Leleu, T., V. Chavagnac, A. Delacour, C. Noiriél, G. Ceuleneer, M. Aretz, C. Rommevaux, and S. Ventalon (2016), Travertines associated with hyperalkaline springs: Evaluation as a proxy for paleoenvironmental conditions, and sequestration of atmospheric CO<sub>2</sub>, *J. Sedimentary Res.*, 86, 1328-1343.
- Leong, J. A., M. Nielson, N. McQueen, W. McGillis, and P. Kelemen (2021a), Serpentinization rates in low-temperature, continental, ultramafic environments: Clues from H<sub>2</sub> and CH<sub>4</sub> outgassing rates in the Samail ophiolite, Oman, *Goldschmidt Conference Abstracts*.
- Leong, J. A. M., A. E. Howells, K. J. Robinson, A. Cox, R. V. Debes II, K. Fecteau, P. Prapaipong, and E. L. Shock (2021b), Theoretical predictions vs environmental observations on serpentinization fluids: Lessons from the Samail ophiolite in Oman, *J. Geophys. Res.*, 126, e2020JB020756.
- Leong, J. A. M., and E. L. Shock (2020), Thermodynamic constraints on the geochemistry of low-temperature, continental, serpentinization-generated fluids, *Am. J. Sci.*, 320, 185-235.
- Lindberg, R. D., and D. D. Runnells (1984), Ground water redox reactions: An analysis of equilibrium state applied to Eh measurements and geochemical modeling, *Science*, 225, 925-927.
- Lippard, S. J., A. W. Shelton, and I. G. Gass (1986), *The Ophiolite of Northern Oman. Geological Society London Memoir 11*, 178 pp.
- Lisabeth, H., W. Zhu, T. Xing, and V. De Andrade (2017a), Dissolution-assisted pattern formation during olivine carbonation, *Geophys. Res. Lett.*, 44, doi:10.1002/2017GL074393.
- Lisabeth, H. P., W. Zhu, P. B. Kelemen, and A. Ilgen (2017b), Experimental evidence for chemo-mechanical coupling during carbon mineralization in ultramafic rocks, *Earth Planet Sci. Lett.*, 474, 355-367.
- Lods, G., D. Roubinet, J. M. Matter, R. Leprovost, P. Gouze, and Oman Drilling Project Science Team (2020), Groundwater flow characterization of an ophiolitic hard-rock aquifer from cross-borehole multi-level hydraulic experiments, *J. Hydrology*, 589, 125152.
- MacDonald, A. H., and W. S. Fyfe (1985), Rate of serpentinization in seafloor environments, *Tectonophysics*, 116(1-2), 123-135.
- MacLeod, C. J., C. J. Lissenberg, and L. E. Bibby (2013), “Moist MORB” axial magmatism in the Oman ophiolite: the evidence against a mid-ocean ridge origin, *Geology*, 41, 459-462.
- Malvoisin, B., N. Brantut, and M.-A. Kaczmarek (2017), Control of serpentinization rate by reaction-induced cracking, *Earth Planet Sci. Lett.*, 476, 143-152.
- Malvoisin, B., C. Zhang, O. Müntener, L. P. Baumgartner, P. B. Kelemen, and Oman Drilling Project Science Team (2020), Measurement of volume change and mass transfer during serpentinisation: Insights from the Oman Drilling Project, *J. Geophys. Res.*, 125, e2019JB018877.
- Manuella, F. C., G. Della Ventura, F. Galdenzi, and S. Carbone (2019), Sr-rich aragonite veins in Hyblean serpentinized peridotite xenoliths (Sicily, Italy): Evidence for abyssal-type carbonate metasomatism, *Lithos*, 326, 200-212.
- Martin, W., J. Baross, D. Kelley, and M. J. Russell (2008), Hydrothermal vents and the origin of life, *Nature Rev. Microbio.*, 6, 805-814.
- Martin, W., and M. J. Russell (2007), On the origin of biochemistry at an alkaline hydrothermal vent, *Phil. Trans. Roy. Soc. London*, B362, 1887-1926.

- Mayhew, L. E., and E. T. Ellison (2020), A synthesis and meta-analysis of the Fe chemistry of serpentinites and serpentine minerals, *Phil. Trans. Roy. Soc. London*, A378, 20180420.
- Mayhew, L. E., E. T. Ellison, H. M. Miller, P. B. Kelemen, and A. S. Templeton (2018), Iron transformations during low temperature alteration of variably serpentinized rocks from the Samail ophiolite, Oman, *Geochim. Cosmochim. Acta*, 222, 704-728.
- McArthur, J. M., R. J. Howarth, G. A. Shields, and Y. Zhou (2020), Strontium isotope stratigraphy, *Geologic Time Scale*, 211-238.
- McCollom, T. M. (1999), Methanogenesis as a potential source of chemical energy for primary biomass production by autotrophic organisms in hydrothermal systems on Europa, *J. Geophys. Res.*, 104, 30729-30742.
- McCollom, T. M. (2007), Geochemical constraints on sources of metabolic energy for chemolithoautotrophy in ultramafic-hosted deep-sea hydrothermal systems, *Astrobio.*, 7, 933-950.
- McCollom, T. M., and W. Bach (2009), Thermodynamic constraints on hydrogen generation during serpentinization of ultramafic rocks, *Geochim. Cosmochim. Acta*, 73, 856-875.
- McCollom, T. M., F. Klein, M. Robbins, B. Moskowitz, T. S. Berquó, N. Jöns, W. Bach, and A. Templeton (2016), Temperature trends for reaction rates, hydrogen generation, and partitioning of iron during experimental serpentinization of olivine, *Geochim. Cosmochim. Acta*, 181, 175-200.
- Mervine, E. M., S. E. Humphris, K. W. W. Sims, P. B. Kelemen, and W. J. Jenkins (2014), Carbonation rates of peridotite in the Samail Ophiolite, Sultanate of Oman constrained through <sup>14</sup>C dating and stable isotopes, *Geochim. Cosmochim. Acta*, 126, 371-397.
- Mervine, E. M., K. W. W. Sims, S. E. Humphris, and P. B. Kelemen (2015), Applications and limitations of U-Th disequilibria systematics for determining rates of peridotite carbonation in the Samail Ophiolite, Sultanate of Oman, *Chem. Geol.*, 412, 151-166.
- Miller, H. M., J. M. Matter, P. Kelemen, E. T. Ellison, M. Conrad, N. Fierer, and A. S. Templeton (2016), Modern water/rock reactions in Oman hyperalkaline peridotite aquifers and implications for microbial habitability, *Geochim. Cosmochim. Acta*, 179, 217-241.
- Mock, D., D. A. Neave, S. Müller, D. Garbe-Schönberg, O. Namur, B. Ildefonse, and J. Koepke (2021), Formation of igneous layering in the lower oceanic crust from the Samail Ophiolite, Sultanate of Oman, *J. Geophys. Res.*, 126, e2020JB019573.
- Monnier, C., J. Girardeau, L. Le Mée, and P. M. (2006), Along-ridge petrological segmentation of the mantle in the Oman ophiolite, *G-cubed*, 7, doi:10.1029/2006GC001320.
- Monnin, C., et al. (2014), Fluid chemistry of the low temperature hyperalkaline hydrothermal system of Prony Bay (New Caledonia), *Biogeosciences*, 11, 5687-5706.
- Morrissey, L. S., and P. L. Morrill (2017), Flux of methane release and carbon dioxide sequestration at Winterhouse Canyon, Gros Morne, Newfoundland, Canada: a site of continental serpentinization, *Can. J. Earth Sci.*, 54, 257-262.
- Müller, T., J. Koepke, C. D. Garbe-Schönberg, M. Dietrich, U. Bauer, and P. E. Wolff (2017), Anatomy of a frozen axial melt lens from a fast-spreading paleo-ridge (Wadi Gideah, Oman ophiolite), *Lithos*, 272, 31-45.
- Navak, B., and F. M. Meyer (2015), Tetrataenite in terrestrial rock, *Am. Min.*, 100, 209-214.
- Neal, C., and G. Stanger (1983), Hydrogen generation from mantle source rocks in Oman, *Earth Planet Sci. Lett.*, 66, 315-320.
- Neal, C., and G. Stanger (1984), Calcium and magnesium hydroxide precipitation from alkaline groundwaters in Oman, and their significance to the process of serpentinization, *Min. Mag.*, 48, 237-241.
- Neal, C., and G. Stanger (1985), Past and present serpentinization of ultramafic rocks: An example from the Semail ophiolite nappe of northern Oman, in *The Chemistry of Weathering*, edited by J. I. Drever, pp. 249-275, D. Reidel Publishing Company, Holland.
- Newman, S. A., S. A. Lincoln, S. O'Reilly, X. Liu, E. L. Shock, P. B. Kelemen, and R. E. Summons (2020), Lipid biomarker record of the serpentinite-hosted ecosystem of the samail ophiolite, Oman and implications for the search for Biosignatures on Mars, *Astrobio.*, 20, 830-845.
- Nicolas, A., and F. Boudier (2008), Large shear zones with no relative displacement, *Terra Nova*, 20, 200-205.
- Nicolas, A., F. Boudier, B. Ildefonse, and E. Ball (2000a), Accretion of Oman and United Arab Emirates ophiolite: Discussion of a new structural map, *Marine Geophys. Res.*, 21(3-4), 147-179.
- Nicolas, A., F. Boudier, B. Ildefonse, and E. Ball (2000b), Accretion of Oman and United Arab Emirates ophiolite: Discussion of a new structural map, *Marine Geophys. Res.*, 21, 147-179.
- Nicolas, A., D. Mainprice, and F. Boudier (2003), High-temperature seawater circulation throughout crust of oceanic ridges: A model derived from the Oman ophiolites, *J. Geophys. Res.*, 108.

- Nicolas, A., I. Reuber, and K. Benn (1988), A new magma chamber model based on structural studies in the Oman ophiolite, *Tectonophysics*, 151, 87-105.
- Niu, Y. L. (2004), Bulk-rock major and trace element compositions of abyssal peridotites: Implications for mantle melting, melt extraction and post-melting processes beneath mid-ocean ridges, *Journal of Petrology*, 45, 2423-2458.
- Noël, J., M. Godard, E. Olliot, I. Martinez, M. Williams, F. Boudier, O. Rodriguez, C. Chaduteaub, S. Escario, and P. Gouze (2018), Evidence of polygenetic carbon trapping in the Oman Ophiolite: Petro-structural, geochemical, and carbon and oxygen isotope study of the Wadi Dima harzburgite-hosted carbonates (Wadi Tayin massif, Sultanate of Oman), *Lithos*, 323, 218-237.
- Nolan, S. C., P. W. Skelton, B. P. Clissold, and J. D. Smewing (1990), Maastrichtian to early Tertiary stratigraphy and palaeogeography of the Central and Northern Oman Mountains *Geol. Soc. Special Pub.*, 49, 495-519.
- Nothaft, D. B., A. S. Templeton, E. S. Boyd, J. M. Matter, M. Stute, A. N. Paukert Vankeuren, and O. D. P. S. Team (2021a), Aqueous geochemical and microbial variation across discrete depth intervals in a peridotite aquifer assessed using a packer system in the Samail Ophiolite, Oman, *J. Geophys. Res.*, 126, e2021JG006319.
- Nothaft, D. B., et al. (2021b), Geochemical, biological and clumped isotopologue evidence for substantial microbial methane production under carbon limitation in serpentinites of the Samail Ophiolite, Oman, *J. Geophys. Res.*, 126, e2020JG006025.
- O'Hanley, D. S. (1992), Solution to the volume problem in serpentinization, *Geology*, 20, 705-708.
- O'Hanley, D. S., and M. D. Dyar (1993), The composition of lizardite 1T and the formation of magnetite in serpentinites. *American Mineralogist*, 78(3-4), 391-404, *Am. Min.*, 78, 391-404.
- O'Neil, J. R., R. N. Clayton, and T. K. Mayeda (1969), Oxygen isotope fractionation in divalent metal carbonates, *J. Chem. Phys.*, 51, 5547-5558.
- Oeser, M., H. Strauss, P. E. Wolff, J. Koepke, M. Peters, D. Garbe-Schönberg, and M. Dietrich (2012), A profile of multiple sulfur isotopes through the Oman ophiolite, *Chem. Geol.*, 312-313, 27-46.
- Oskierski, H. C., J. G. Bailey, E. M. Kennedy, G. Jacobsen, P. M. Ashley, and B. Z. Dlugogorski (2013a), Formation of weathering-derived magnesite deposits in the New England Orogen, New South Wales, Australia: Implications from mineralogy, geochemistry and genesis of the Attunga magnesite deposit, *Mineralium Deposita*, 48, 525-641.
- Oskierski, H. C., B. Z. Dlugogorski, and G. Jacobsen (2013b), Sequestration of atmospheric CO<sub>2</sub> in a weathering-derived, serpentinite-hosted magnesite deposit: <sup>14</sup>C tracing of carbon sources and age constraints for a refined genetic model, *Geochim. Cosmochim. Acta*, 122, 226-246.
- Oskierski, H. C., B. Z. Dlugogorski, and G. Jacobsen (2013c), Sequestration of atmospheric CO<sub>2</sub> in chrysotile mine tailings of the Woodsreef Asbestos Mine, Australia: Quantitative mineralogy, isotopic fingerprinting and carbonation rates, *Chem. Geol.*, 358, 156-169.
- Paukert, A. N., J. M. Matter, P. B. Kelemen, E. L. Shock, and J. R. Havig (2012), Reaction path modeling of enhanced in situ CO<sub>2</sub> mineralization for carbon sequestration in the peridotite of the Samail Ophiolite, Sultanate of Oman, *Chem. Geol.*, 330-331, 86-100.
- Paukert Vankeuren, A. N., J. M. Matter, M. Stute, and P. B. Kelemen (2019), Multitracer determination of apparent groundwater ages in peridotite aquifers within the Samail Ophiolite, Sultanate of Oman, *Earth Planet Sci. Lett.*, 516, 37-48.
- Paulick, H., W. Bach, M. Godard, J. C. M. De Hoog, G. Suhr, and J. Harvey (2006), Geochemistry of abyssal peridotites (Mid-Atlantic Ridge, 15° 20' N, ODP Leg 209): implications for fluid/rock interaction in slow spreading environments, *Chem. Geol.*, 234, 179-210.
- Pearce, J. A., T. Alabaster, A. W. Shelton, and M. P. Searle (1981), The Oman Ophiolite as a Cretaceous Arc-Basin Complex: Evidence and Implications, *Phil. Trans. Roy. Soc. London*, A300, 299-317.
- Pearce, J. A., and D. W. Peate (1995), Tectonic implications of the composition of volcanic arc magmas, *Ann. Rev. Earth Planet. Sci.*, 23, 251-286.
- Pens, M., M. Andreani, I. Daniel, J. P. Perrillat, and H. Cardon (2016), Contrasted effect of aluminum on the serpentinization rate of olivine and orthopyroxene under hydrothermal conditions, *Chem. Geol.*, 441, 256-264.
- Peucker-Ehrenbrink, B., H. K. T. Atwood, and P. B. Kelemen (2012), Rhenium-osmium isotope systematics and platinum group element concentrations in oceanic crust, *Geology*, 40, 199-202.
- Picazo, S., B. Malvoisin, L. Baumgartner, and A. S. Bouvier (2020), Low temperature serpentinite replacement by carbonates during seawater influx in the Newfoundland Margin, *Minerals*, 10, 184.
- Python, M., and G. Ceuleneer (2003), Nature and distribution of dykes and related melt migration structures in the mantle section of the Oman ophiolite, *G-cubed*, 4.



- Quesnel, B., P. Boulvais, P. Gautier, M. Cathelineau, C. M. John, M. Dierick, P. Agrinier, and M. Drouillet (2016), Paired stable isotopes (O, C) and clumped isotope thermometry of magnesite and silica veins in the New Caledonia Peridotite Nappe, *Geochim. Cosmochim. Acta*, *183*, 234-249.
- Quesnel, B., P. Gautier, P. Boulvais, M. Cathelineau, P. Maurizot, D. Cluzel, M. Ulrich, S. Guillot, S. Lesimple, and C. Couteau (2013), Syn-tectonic, meteoric water-derived carbonation of the New Caledonia peridotite nappe, *Geology*, *41*, 1063-1066.
- Quick, J. E. (1982), The origin and significance of large, tabular dunite bodies in the Trinity peridotite, northern California, *Contrib. Mineral. Petrol*, *78*, 413-422.
- Rajendran, S., and S. Nasir (2019), Mapping of hydrothermal alteration in the upper mantle-lower crust transition zone of the Tayin Massif, Sultanate of Oman using remote sensing technique, *J. African Earth Sci.*, *150*, 722-743.
- Rajendran, S., S. Nasir, T. M. Kusky, and S. al-Khribash (2014), Remote sensing based approach for mapping of CO<sub>2</sub> sequestered regions in Samail ophiolite massifs of the Sultanate of Oman. *Earth-Science Reviews*, *135*, pp.122-140, *Earth Sci. Rev.*, *135*, 122-140.
- Rempfert, K. R., H. M. Miller, N. Bompard, D. Nothaft, J. M. Matter, P. Kelemen, N. Fierer, and A. S. Templeton (2017), Geological and geochemical controls on subsurface microbial life in the Samail Ophiolite, Oman, *Frontiers in Microbiology*, Article 56.
- Rioux, M., S. Bowring, P. Kelemen, S. Gordon, F. Dudás, and R. Miller (2012), Rapid crustal accretion and magma assimilation in the Oman-U.A.E. ophiolite: High precision U-Pb zircon geochronology of the gabbroic crust, *J. Geophys. Res.*, *117*, B07201, doi:07210.01029/02012JB009273.
- Rioux, M., S. Bowring, P. Kelemen, S. Gordon, R. Miller, and F. Dudás (2013), Tectonic development of the Samail ophiolite: High precision U-Pb zircon geochronology of crustal growth and ophiolite emplacement, *J. Geophys. Res.*, *118*, 2085-2101.
- Rollinson, H. (2019), Dunites in the mantle section of the Oman ophiolite: The boninite connection, *Lithos*, *334*, 1-7.
- Rospabé, M., G. Ceuleneer, M. Benoit, B. Abily, and P. Pinet (2017), Origin of the dunitic mantle-crust transition zone in the Oman ophiolite: The interplay between percolating magmas and high temperature hydrous fluids, *Geology*, *45*, 471-474.
- Røyne, A., and B. Jamtveit (2015), Pore-scale controls on reaction-driven fracturing, *Rev. Min. & Geochem.*, *80*, 25-44.
- Rudge, J. F., P. B. Kelemen, and M. Spiegelman (2010), A simple model of reaction-induced cracking applied to serpentinization and carbonation of peridotite, *Earth Planet Sci. Lett.*, *291*, 215-227, doi:10.1016/j.epsl.2010.01.016.
- Russell, M. J., A. J. Hall, and W. Martin (2010), Serpentinization as a source of energy at the origin of life, *Geobiology*, *8*, 355-371.
- Salvatore, M. R., T. A. Goudge, M. S. Bramble, C. S. Edwards, J. L. Bandfield, E. S. Amador, J. F. Mustard, and P. R. Christensen (2018), Bulk mineralogy of the NE Syrtis and Jezero crater regions of Mars derived through thermal infrared spectral analyses, *Icarus*, *301*, 76-96.
- Sánchez-Murillo, R., E. Gazel, E. M. Schwarzenbach, M. Crespo-Medina, M. O. Schrenk, J. Boll, and B. C. Gill (2014), Geochemical evidence for active tropical serpentinization in the Santa Elena Ophiolite, Costa Rica: An analog of a humid early Earth?, *G-cubed*, *15*, 1783-1800.
- Sano, Y., A. Urabe, H. Wakita, and H. Wushiki (1993), Origin of hydrogen-nitrogen gas seeps, Oman, *Appl. Geochem.*, *8*, 1-8.
- Schlüter, M., T. Steuber, M. Parente, and J. Mutterlose (2008), Evolution of a Maastrichtian–Paleocene tropical shallow-water carbonate platform (Qalhat, NE Oman), *Facies*, *54*, 513-527.
- Schulte, M., D. Blake, T. Hoehler, and T. McCollom (2006), Serpentinization and its implications for life on the early Earth and Mars, *Astrobio.*, *6*, 364-376.
- Schwarzenbach, E. M., G. L. Früh-Green, S. M. Bernasconi, J. C. Alt, W. C. Shanks III, L. Gaggero, and L. Crispini (2012), Sulfur geochemistry of peridotite-hosted hydrothermal systems: Comparing the Ligurian ophiolites with oceanic serpentinites, *Geochim. Cosmochim. Acta*, *91*, 283-305.
- Schwarzenbach, E. M., B. C. Gill, E. Gazel, and P. Madrigal (2016), Sulfur and carbon geochemistry of the Santa Elena peridotites: Comparing oceanic and continental processes during peridotite alteration, *Lithos*, *252*, 92-106.
- Schwarzenbach, E. M., J.C. Vrijmoed, J. M. Engelmann, M. Liesegang, U. Wiechert, R. Röhne, and O. Plümper (2021), Sulfide dissolution and awaruite formation in continental serpentinization environments and its implications to supporting life, *J. Geophys. Res.*, *126*, e2021JB021758.
- Schwarzenbach, E. M., S. Q. Lang, G. L. Früh-Green, M. D. Lilley, S. M. Bernasconi, and S. Mehay (2013), Sources and cycling of carbon in continental, serpentinite-hosted alkaline springs in the Voltri Massif, Italy, *Lithos*, *177*, 226-244.

- Sciortino, M., J. E. Mungall, and J. Muinonen (2015), Generation of High-Ni sulfide and alloy phases during serpentinization of dunite in the Dumont sill, Quebec. *Economic Geology*, 110(3), pp.733-761, *Econ. Geol.*, 110, 733-761.
- Searle, M., and J. Cox (2002), Subduction zone metamorphism during formation and emplacement of the Semail ophiolite in the Oman Mountains, *Geol. Mag.*, 139, 241-255.
- Searle, M. P., and J. Malpas (1980), The structure and metamorphism of rocks beneath the Semail ophiolite of Oman and their significance in ophiolite obduction, *Trans. Roy. Soc. Edinburgh Earth Sci.*, 71, 247-262.
- Seyler, M., and E. Bonatti (1997), Regional-scale melt-rock interaction in Iherzolitic mantle in the Romanche Fracture Zone (Atlantic Ocean). *Earth and Planetary Science Letters*, 146(1-2), pp.273-287., *Earth Planet Sci. Lett.*, 146, 273-287.
- Seyler, M., J. P. Lorand, H. J. B. Dick, and M. Drouin (2007), Pervasive melt percolation reactions in ultra-depleted refractory harzburgites at the Mid-Atlantic Ridge, 15 20' N: ODP Hole 1274A, *Contrib. Mineral. Petrol.*, 153, 303-319.
- Shock, E. L. (1997), High-temperature life without photosynthesis as a model for Mars, *J. Geophys. Res.*, 102, 23687-23694.
- Shock, E. L., and H. C. Helgeson (1988), Calculation of the thermodynamic and transport properties of aqueous species at high pressures and temperatures: Correlation algorithms for ionic species and equation of state predictions to 5 kb and 1000°C, *Geochim. Cosmochim. Acta*, 52, 2009-2036.
- Shock, E. L., M. Holland, J. P. Amend, G. R. Osburn, and T. P. Fischer (2010), Quantifying inorganic sources of geochemical energy in hydrothermal ecosystems, Yellowstone National Park, USA, *Geochim. Cosmochim. Acta*, 74, 4005-4043.
- Shock, E. L., T. McCollom, and M. D. Schulte (1995), Geochemical constraints on chemolithoautotrophic reactions in hydrothermal systems, *Origins of Life and Evolution of the Biosphere*, 25, 141-159.
- Shock, E. L., D. C. Sassani, M. Willis, and D. A. Sverjensky (1977), Inorganic species in geologic fluids: Correlations among standard molal thermodynamic properties of aqueous ions and hydroxide complexes, *Geochim. Cosmochim. Acta*, 907-950.
- Sleep, N. H., D. K. Bird, and E. C. Pope (2011), Serpentinite and the dawn of life, *Phil. Trans. Roy. Soc. London*, B366, 2857-2869.
- Sleep, N. H., A. Meibom, T. Fridriksson, R. G. Coleman, and D. K. Bird (2004), H<sub>2</sub>-rich fluids from serpentinization: Geochemical and biotic implications, *Proc. Nat. Acad. Sci.*, 101, 12818-12823.
- Smewing, J. D. (1981), Mixing characteristics and compositional differences in mantle-derived melts beneath spreading axes: Evidence from cyclically layered rocks in the ophiolite of North Oman, *J. Geophys. Res.*, 86, 2645-2659.
- Snow, J. E., and H. J. B. Dick (1995), Pervasive magnesium loss by marine weathering of peridotite, *Geochim. Cosmochim. Acta*, 59, 4219-4235.
- Soret, M., P. Agard, B. Dubacq, A. Plunder, and P. Yamato (2017), Petrological evidence for stepwise accretion of metamorphic soles during subduction infancy (Semail ophiolite, Oman and UAE), *J. Metamorphic Geol.*, 35, 1051-1080.
- Stanger, G., J. Laver, and C. Neal (1988), Black carbonaceous calcite associated with serpentinite from Oman, *Min. Mag.*, 52, 403-408.
- Stanger, G., and C. Neal (1994), The occurrence and chemistry of huntite from Oman, *Chem. Geol.*, 112, 247-254.
- Streit, E., P. Kelemen, and J. Eiler (2012), Coexisting serpentine and quartz from carbonate-bearing serpentinized peridotite in the Semail Ophiolite, Oman, *Contrib. Mineral. Petrol.*, 164, 821-837.
- Suhr, G., P. B. Kelemen, and H. Paulick (2008), Microstructures in Hole 1274A peridotites, ODP Leg 209, Mid-Atlantic Ridge: Tracking the fate of melts percolating in peridotite as the lithosphere is intercepted, *G-cubed*, 9.
- Sverjensky, D. A., E. L. Shock, and H. C. Helgeson (1997), Prediction of the thermodynamic properties of aqueous metal complexes to 1000°C and 5 kb, *Geochim. Cosmochim. Acta*, 61, 1359-1412.
- Takazawa, E., N. Abe, M. Seyler, W. P. Meurer, and P. B. Kelemen (2007), Hybridization of dunite and gabbroic materials in Hole 1271B from Mid-Atlantic Ridge 15 N: implications for melt flow and reaction in the upper mantle, *Proc. ODP, Sci. Results*, 209, 1-23.
- Takazawa, E., T. Okayasu, and K. Satoh (2003), Geochemistry and origin of the basal Iherzolites from the northern Oman ophiolite (northern Fizz block), *G-cubed*, 4, 1021.
- Tamura, A., and S. Arai (2006), Harzburgite-dunite-orthopyroxenite suite as a record of supra-subduction zone setting for the Oman ophiolite mantle, *Lithos*, 90, 43-56.

- Tarnas, J., et al. (2021), Characteristics, origins, and biosignature preservation potential of carbonate-bearing rocks within and outside of Jezero Crater, *J. Geophys. Res.*, *126*, e2021JE006898.
- Tartarotti, P., S. Susini, P. Nimis, and L. Ottolini (2002), Melt migration in the upper mantle along the Romanche Fracture Zone (Equatorial Atlantic), *Lithos*, *63*, 125-149.
- Taylor, R. M., H. C. B. Hansen, G. Stanger, and C. B. Koch (1991), On the genesis and composition of natural pyroaurite, *Clay Minerals*, *26*, 297-309.
- Templeton, A., et al. (2021), Accessing the subsurface biosphere within rocks undergoing active low-temperature serpentinization in the Samail ophiolite (Oman Drilling Project), *J. Geophys. Res.*, *126*, e2021JG006315.
- Templeton, A. S., and E. T. Ellison (2020), Formation and loss of metastable brucite: does Fe (II)-bearing brucite support microbial activity in serpentinizing ecosystems?, *Phil. Trans. Roy. Soc. London*, *A378*, 20180423.
- Tilton, G. R., C. A. Hopson, and J. E. Wright (1981), Uranium-lead isotopic ages of the Samail ophiolite, Oman, with applications to Tethyan ocean ridge tectonics, *J. Geophys. Res.*, *86*, 2736-2775.
- Tomkinson, T., M. R. Lee, D. F. Mark, and C. L. Smith (2013), Sequestration of Martian CO<sub>2</sub> by mineral carbonation, *Nature Communications*, *4*, 1-6.
- Tornos, F., et al. (2019), 2019. Do microbes control the formation of giant copper deposits?, *Geology*, *47*, 143-146.
- Tutolo, B. M., B. W. Evans, and S. M. Kuehner (2019), Serpentine–hisingerite solid solution in altered ferroan peridotite and Olivine Gabbro, *Minerals*, *9*, 47.
- Tutolo, B. M., and K. A. Evans (2018), Tochilinite occurrence in serpentinized peridotite from the Samail Ophiolite, *AGU Fall Meeting Abstracts*, *V13E-0160*.
- Tutolo, B. M., A. J. Luhmann, N. J. Tosca, and W. E. Seyfried (2018), Serpentinization as a reactive transport process: the brucite silicification reaction, *Earth Planet Sci. Lett.*, *484*, 385-395.
- Tutolo, B. M., W. E. Seyfried, and N. J. Tosca (2020), A seawater throttle on H<sub>2</sub> production in Precambrian serpentinizing systems, *Proc. Nat. Acad. Sci.*, *117*, 14756-14763.
- Ulrich, M., M. Munoz, S. Guillot, M. Cathelineau, C. Picard, B. Quesnel, P. Boulvais, and C. Couteau (2014), Dissolution–precipitation processes governing the carbonation and silicification of the serpentinite sole of the New Caledonia ophiolite, *Contrib. Mineral. Petrol.*, *167*, 952; doi 910.1007/s00410-00013-00952-00418.
- Ulven, O. I., B. Jamtveit, and A. Malthe-Sorensen (2014a), Reaction driven fracturing of porous rocks, *J. Geophys. Res.*, *119*, doi:10.1002/2014JB011102.
- Ulven, O. I., H. Storheim, H. Austrheim, and A. Malthe-Sorensen (2014b), Fracture initiation during volume increasing reactions in rocks and applications for CO<sub>2</sub> sequestration, *Earth Planet Sci. Lett.*, *389*, 132-142.
- Urann, B. M., H. J. B. Dick, R. Parnell-Turner, and J. F. Casey (2020), Recycled arc mantle recovered from the Mid-Atlantic Ridge, *Nature Communications*, *11*, 1-9.
- Vacquand, C., E. Deville, V. Beaumont, F. Guyot, O. Sissmann, D. Pillot, C. Arcilla, and A. Prinzhofer (2018), Reduced gas seepages in ophiolitic complexes: Evidences for multiple origins of the H<sub>2</sub>-CH<sub>4</sub>-N<sub>2</sub> gas mixtures, *Geochim. Cosmochim. Acta*, *223*, 437-461.
- VanTongeren, J. A., G. Hirth, and P. B. Kelemen (2015), Constraints on the accretion of the gabbroic lower oceanic crust from plagioclase lattice preferred orientations in the Samail ophiolite, *Earth Planet. Sci. Lett.*, *427*, 249-261.
- VanTongeren, J. A., P. B. Kelemen, and K. Hanghoj (2008), Cooling rates in the lower crust of the Oman ophiolite: Ca in olivine, revisited, *Earth Planet. Sci. Lett.*, *267*, 69-82.
- Varnes, E. S., B. M. Jakosky, and T. M. McCollom (2003), Biological potential of Martian hydrothermal systems, *Astrobio.*, *3*, 407-414.
- Vasconcelos, C., J. A. McKenzie, R. Warthmann, and S. M. Bernasconi (2005), Calibration of the  $\delta^{18}\text{O}$  paleothermometer for dolomite precipitated in microbial cultures and natural environments, *Geology*, *33*, 317-320.
- Wang, J., N. Watanabe, A. Okamoto, K. Nakamura, and T. Komai (2020), Characteristics of hydrogen production with carbon storage by CO<sub>2</sub>-rich hydrothermal alteration of olivine in the presence of Mg–Al spinel, *Int. J. Hydrogen Energy*, *45*, 13163-13175.
- Warren, C., R. Parrish, D. Waters, and M. Searle (2005), Dating the geologic history of Oman's Samail ophiolite: Insights from U-Pb geochronology, *Contrib. Mineral. Petrol.*, *150*, 403-422.
- Weis, D., et al. (2006), High-precision isotopic characterization of USGS reference materials by TIMS and MC-ICP-MS, *G-cubed*, *7*.

- Weyhenmeyer, C. E. (2000), Origin and evolution of groundwater in the alluvial aquifer of the Eastern Batinah Coastal Plain, Sultanate of Oman : a hydrogeochemical approach, University of Bern, Bern, CH.
- Wolery, T., and R. Jarek (2003), *EQ3/6, Version 8.0, Software User's Manual (No. 10813-UM-8.0-00)*. US Department of Energy, Office of Civilian Radioactive Waste Management, Office of Repository Development.
- Wolery, T. J. (1992), EQ3/6, a software package for geochemical modeling of aqueous systems: package overview and installation guide (version 7.0) (No. UCRL-MA--110662-PT. 1), *Lawrence Livermore National Lab*.
- Wolery, T. J., and C. F. Jove-Colon (2004), *Qualification of thermodynamic data for geochemical modeling of mineral-water interactions in dilute systems (ANL-WIS-GS-000003)*, 212 pp., US Department of Energy, Office of Civilian Radioactive Waste Management, Office of Repository Development.
- Wyns, R., F. Bechennec, J. Le Meteour, and J. Roger (1992), Geological Map of the Tiwi Quadrangle, Sultanate of Oman. Geoscience Map, Scale 1:100,000, Sheet NF 40-8B, Ministry of Petroleum and Minerals, Directorate General of Minerals, Sultanate of Oman, Muscat, Oman.
- Yoshida, K., A. Okamoto, H. Shimizu, R. Oyanagi, N. Tsuchiya, and Oman Drilling Project Phase 2 Science Party (2020), Fluid Infiltration Through Oceanic Lower Crust in Response to Reaction-Induced Fracturing: Insights From Serpentinized Troctolite and Numerical Models, *J. Geophys. Res.*, *125*, e2020JB020268.
- Yoshikawa, M., M. Python, A. Tamura, S. Arai, E. Takazawa, T. Shibata, A. Ueda, and T. Sato (2015), Melt extraction and metasomatism recorded in basal peridotites above the metamorphic sole of the northern Fizh massif, Oman ophiolite, *Tectonophys.*, *650*, 53-64.
- Zammit, C. M., J. P. Shuster, E. J. Gagen, and G. Southam (2015), The geomicrobiology of supergene metal deposits, *Elements*, *11*, 337-342.
- Zheng, X., B. Cordonnier, J. McBeck, E. Boller, B. Jamtveit, W. Zhu, and F. Renard (2019), Mixed-mode strain localization generated by hydration reaction at crustal conditions, *J. Geophys. Res.*, *124*, 4507-4522.
- Zheng, X., B. Cordonnier, W. Zhu, F. Renard, and B. Jamtveit (2018), Effects of confinement on reaction-induced fracturing during hydration of periclase, *G-cubed*, *19*, 2661-2672.
- Zhu, W., F. Fusses, H. Lisabeth, T. Xing, X. Xiao, V. De Andrade, and S.-I. Karato (2016), Experimental evidence of reaction-induced fracturing during olivine carbonation, *Geophys. Res. Lett.*, *43*, 9535-9543.
- Zihlmann, B., S. Müller, R. M. Coggon, J. Koepke, D. Garbe-Schönberg, and D. A. H. Teagle (2018), Hydrothermal fault zones in the lower oceanic crust: An example from Wadi Gideah, Samail ophiolite, Oman, *Lithos*, *323*, 103-124.
- Zolotov, M. Y. (2014), Formation of brucite and cronstedtite-bearing mineral assemblages on Ceres, *Icarus*, *228*, 13-26.